6-1996

Ionization and Charge Changing in 0.5 - 8 qMeV Li^q+ + He (q=1,2,3) Collisions and Setup of an Electron Spectrometer Control System

Oliver Woitke
Western Michigan University

IONIZATION AND CHARGE CHANGING IN 0.5 - 8 qMeV Li^{q+} + He (q=1,2,3) COLLISIONS AND SETUP OF AN ELECTRON SPECTROMETER CONTROL SYSTEM

by

Oliver Woitke

A Dissertation
Submitted to the
Faculty of The Graduate College
in partial fulfillment of the
requirements for the
Degree of Doctor of Philosophy
Department of Physics

Western Michigan University
Kalamazoo, Michigan
June 1996

IONIZATION AND CHARGE CHANGING IN 0.5 - 8 qMeV Li^{q+} + He (q=1,2,3) COLLISIONS AND SETUP OF AN ELECTRON SPECTROMETER CONTROL SYSTEM

Oliver Woitke, Ph.D.

Western Michigan University, 1996

Projectile charge changing and target ionization cross sections are measured for 0.5 to 8 qMeV Li^{q+} + He (q=1,2,3) collisions. Total cross sections for single-electron capture (for $Li^{1,2,3+}$) and single-electron loss (for $Li^{1,2+}$) are obtained and compared to existing experimental and theoretical data. Also, single and double target ionization of He associated with specific outgoing projectile charge states are identified using coincidence techniques. Cross sections for target ionization associated with no projectile charge change (direct ionization), single-electron capture, and single-electron loss are measured and compared to existing experimental data and to available calculations. Double-to-single target ionization ratios R are obtained and interpreted in terms of theoretical formulations involving electron - nucleus interactions and electron - electron interactions. It is found that R for direct ionization is nearly independent of the incident projectile charge state and can be described by the semi-empirical scaling rule of Knudsen et al. (1984). However, the R values associated with single-electron loss and single-electron capture by the projectile depend strongly on the incident charge state of the projectile. Furthermore, R for a given incoming projectile charge state varies strongly

with the reaction channel. Effective charges for Li^{+} and Li^{2+} associated with single and double target ionization are also calculated.

In the second part of this dissertation the control program and data acquisition software for an electron spectrometer system utilizing two plane-mirror analyzers (PMA) are described. This system will be used to measure the energy and angle of electrons ejected in ion-atom collisions.

ACKNOWLEDGEMENTS

I would like to thank my thesis advisor, Dr. John A. Tanis, for his continuous encouragement and support during my studies, and the members of my committee, Drs. Norah Berrah, Dean W. Halderson, Emanuel Y. Kamber, and Frank L. Severance, for reviewing my dissertation. Thanks are also due to Dr. Péter A. Závodszky and Dr. Stephen M. Ferguson who were always willing to help in the lab.

Further I would like to thank my family for their support, my wife Mary for driving me home from the bars, James Houck for an endless supply of cheap beer, and Beavis and Butt-Head for being role models. :-)

Oliver Woitke

TABLE OF CONTENTS

Table of Contents--Continued

LIST OF TABLES

LIST OF FIGURES

List of Figures--Continued

List of Figures--Continued

INTRODUCTION

In this work, processes involving ionization and electron capture in ion-atom collisions have been studied. In particular, the interaction of a fast (≈ 6 % of the speed of light) beam of $Li^{1,2,3+}$ ions with He and H_2 targets is investigated by measuring cross sections for various reaction channels of interest. These results are important both in fundamental and applied physics.

Such studies can help to test theories of few-body-problems arising in atomic physics, specifically the interactions of nuclei with atomic electrons, and the interactions of electrons with other electrons (electron-electron interaction) (McGuire, 1987). For this purpose, the collision system Li^{q+} + He (q=1,2,3) is well suited because electron-electron effects (i.e., electron correlation) can be observed both for the projectile and the target. Helium is the simplest neutral target that shows electron-electron correlation effects, while lithium can serve (a) as a fully-stripped projectile, (b) as a one-electron projectile, or (c) as a two-electron projectile. In the latter two cases, the Li projectile can exhibit electron-electron effects itself.

In the research of nuclear fusion processes, cross sections for electron capture are used to estimate the energy dissipation in plasmas (Glasstone, 1960). Here, an injected positively charged nuclear fuel beam can capture electrons, thereby becoming neutralized and escaping the magnetic confinement.

The present study has three parts: in the first part, total capture and ionization of the $Li^{1,2,3+}$ projectiles in collisions with a He target is investigated; in the second part, target ionization associated with specific outgoing projectile charge states is investigated; in the third part, a computer program to control an electron spectrometer system, used to measure continuum-electron emission as a function of energy and angle, is described.

Of particular interest in this work is the double ionization of He. For the energy range investigated here, double ionization is examined in terms of mechanisms involving independent-particle interactions and electron correlation effects, namely, two-step (TS) and shake-off (SO) processes, respectively. For this purpose, the measured ratio R of double-to-single ionization is compared with theoretical predictions. The ratio R is used because it tends to cancel out single ionization effects and therefore exhibits the main features of the double ionization mechanisms (McGuire, 1987).

The TS process can be understood in the independent-particle picture as two separate interactions (in the same collision event) of the projectile nucleus with each of the target electrons; this picture is valid for intermediate velocities (in which there is sufficient time for two interactions) such that $q/v > 1$ (in atomic units). Knudsen et al. (1984) have found empirically that $R_{TS} \propto (q/v)^2 \ln(v)^{-1}$.

For energies and charges such that $q/v \lesssim 0.1$, the probability of double ionization by separate projectile nucleus - target electron interactions becomes small, and double ionization is instead described by the "sudden approximation" where, after fast ejection of the first electron by the projectile nucleus, the atomic wavefunction of the target helium changes to the ionic wavefunction leaving the second electron still in its original atomic

eigenenergy state. This electron can then be "shaken off" since the matrix element between the atomic state (containing the electron-electron interaction) and the asymptotic ionic state (without electron-electron interaction) is non-zero. This is the so-called SO process for which the ratio R of double-to-single ionization is constant (McGuire, 1982).

Each of the three main areas of investigation in this work is outlined immediately below.

Projectile Capture and Ionization

In this part, electron capture, and single and double loss cross sections for Li^+ projectiles, electron capture and single loss for Li^{2+} projectiles, and electron capture for Li^{3+} projectiles in collision with He and H_2 targets in the energy range 0.5 - 8 qMeV (charge state q=1,2,3), are determined.

For electron capture from He targets to $Li^{1,2,3+}$, the present results are compared to the empirical scaling rule of Schlachter et al. (1987).

For single-electron loss from $Li^{1,2+}$, cross sections are presented and compared to the classical Bohr model as described by Hvelplund et al. (1980) and Knudsen et al. (1982). These data are also used to estimate the fraction of metastable ions in the incident Li^+ beam.

Target Ionization

Here, single and double ionization of He by Li^{q+} projectiles (q=1,2,3) is investigated in the energy range 0.5 - 8 qMeV. Target ionization associated with specific

outgoing projectile charge states is identified using coinicidence techniques. Results are compared with existing experimental and theoretical results where possible.

For bare Li^{3+}, studies concerning single and double ionization of He associated with no projectile charge change and with single-electron capture have been published by Shah and Gilbody (1985) (350 - 2730 keV) and by Knudsen et al. (1984) (4.5, 10.1, 16.2 MeV). The present work provides new data for the single and double ionization of He associated with no projectile charge change and with single-electron capture for incident Li^{3+} in the energy range 4 - 24 MeV. Our results are compared with the earlier measurements.

For Li^{+} and Li^{2+}, Knudsen et al. (1984) obtained target cross sections for single and double ionization (4.5, 10.1, 16.2 MeV) coincident with the unchanged charge state of the projectile. The present work provides new data for R associated with both the unchanged projectile charge state and with single electron capture in the energy range 1 - 8 MeV and 4 - 15 MeV for Li^{+} and Li^{2+}, respectively. Measured values of R are again compared with those obtained for Li^{3+}.

Data for single loss from Li^{+} and Li^{2+} are also presented; for this channel, however, there is only the currently unpublished set of data by Sanders et al. (1995) available for comparison.

Electron Spectrometer Control Program

A sophisticated electron spectrometer system has recently been put into operation in the WMU accelerator laboratory. This system consists of two separate parallel-plate

electron-energy analyzers. One analyzer is fixed in position to analyze electrons emitted in the beam direction, i.e., at 0°, while the other analyzer can be rotated within a range of about 20° - 160° with respect to the beam direction. With this latter setup continuum-electron emission as a function of ejection angle can be measured. Each of the electron-energy analyzers consists of two sets of parallel-plate analyzers. The analyzers in each set are positioned so that electrons are deflected through a total angle of 180° (-90° to 90°) and serve as electrostatic energy-analyzers which direct continuum electrons of a given kinetic energy into a channel-electron multiplier.

A computer program to control the energy analysis and the angular positioning of the electron analyzers has been written. This program controls the voltages on the parallel plates for each analyzer (for electron-energy analysis) as well as the angular position of the movable analyzer. It is written in object-oriented Borland Turbo Pascal 7.0 and enables the user to monitor and control the different modules (i.e., power supplies, scalers, voltmeters, electrometers, motors, and encoders) manually as well as allowing automatic control of the spectrometer functions. In the automatic mode a specified electron energy range can be scanned and the resulting continuum electron-energy spectrum is displayed in realtime. It is possible to program the spectrometer to run in a high-resolution mode (with corresponding lower count rates) for the observation of narrow (< 0.1 eV), closely spaced peaks, or in a low-resolution mode (with higher count rates) for the observation of broader (> 1 eV), more widely spaced peaks.

With this setup, continuum-electron measurements for Li^{2+} + He have been made to test the control program and to complement the results obtained in the first two parts

of this study. In future work, it is planned to measure continuum electrons in coincidence with electron capture, thus involving the removal of two target electrons. As such, these data can be compared and contrasted with the target ionization measurement mentioned above.

THEORETICAL BACKGROUND

In this chapter, various theories for collision mechanisms are presented. In the first two parts, single ionization and single-electron capture are considered in terms of different models. In the third part, target single and double ionization associated with no charge change of the projectile and with single-electron capture to the projectile are examined.

Single Ionization

Classical Bohr Model

Hvelplund et al. (1980) and Knudsen et al. (1982) present a "free collision" model for electron loss (target or projectile). This model assumes that the ion velocity, v, is much larger than the velocity of the electron to be ionized (so that the electron can be assumed to be at rest) and is valid for values of the Bohr parameter

$$\kappa = \frac{q}{v}\ (a.u.) \gg \frac{1}{2}. \qquad (1)$$

Then the interaction is restricted to one active electron and the nucleus is involved only through the electronic binding energy. The collision must be accompanied by an energy transfer sufficient to release the electron from the nucleus. These collisions are usually associated with small impact parameters. The electron-loss cross section is the incoherent

sum of the cross sections for the scattering of a free electron by the impacting nucleus and by the impacting electrons (attached to the impacting particle). In the case of projectile ionization of one-electron ions (Knudsen et al., 1982), the differential ionization cross section by a target with nuclear charge q, and therefore q electrons, impacting on the projectile is (with $d\sigma \propto q^2$):

$$d\sigma_{total} = d\sigma_{nucleus}(q) + q\, d\sigma_{electrons}(1). \quad (2)$$

Since the projectile electron is ejected for all impact energies above the ionization potential, $d\sigma_{total}$ has to be integrated from the ionization potential, I, to infinity to yield the total single ionization cross section:

$$\sigma_{q,q}^{01} = 4\pi a_0^2 (\frac{v_0}{v})^2 \frac{K_0}{I}(q^2+q), \quad (3)$$

where a_0 is the Bohr radius, v_0 is the Bohr velocity, and $K_e = {}^1/_2 m v_0^2$. If *target* ionization is to be calculated (Hvelplund, 1980), the same method can be used, only the roles of projectile and target have to be interchanged.

Born Approximation

Based on Fermi's Golden Rule (Merzbacher, 1970), as shown by McDowell and Coleman (1970), the single ionization cross section can be written as

$$\sigma_{q,q}^{01} = \frac{\mu^2}{4\pi^2\hbar^4}\frac{k_f}{k_i}\int |T_{fi}|^2 d\Omega. \quad (4)$$

Here k_i and k_f denote the initial and the final momentum, respectively, and μ is the reduced mass. The matrix element T_{fi} in the first Born approximation is

$$T_{fi} = \langle e^{i\vec{k}_f\cdot\vec{\sigma}}\phi_f | V | e^{i\vec{k}_i\cdot\vec{\sigma}}\phi_i \rangle, \tag{5}$$

where $\vec{\sigma}$ is the position vector of the projectile relative to the center of mass of the target, Φ_i and Φ_f are the initial and the final target functions, and V is the Coulomb interaction potential between the projectile and the target. To simplify the calculation, the Bethe approximation (McDowell and Coleman, 1970) is employed which involves retaining only the dipole term in the multipole expansion of $\exp(i(\vec{k}_f-\vec{k}_i)\cdot\vec{r}_j)$. This leads to the relation

$$\sigma^{01}_{q,q} \propto \frac{q^2}{E}\ln(C\,E) \xrightarrow[E\to\infty]{} \frac{q^2}{E}, \tag{6}$$

where C is a constant, E is the energy, and q the charge of the projectile.

Single Capture

Bohr-Lindhard Model

Single electron capture from the target to the projectile can be most easily treated classically with a model known as the Bohr-Lindhard model, which was used by Knudsen et al. (1981) to derive scaling rules for a wide range of impact energies and projectile charges.

In this model, two interaction distances are used: the release distance R_r and the

capture distance R_c. If the distance between the projectile and the target is equal to R_r, then the electric force of the projectile on the electron is equal to the binding force of the target on its electron, i.e.,

$$\frac{qe^2}{R_r^2} = \frac{mv_e^2}{r_e}, \tag{7}$$

where m, v_e, and r_e are the mass, orbital velocity and orbital radius of the electron, respectively, and q is the charge of the projectile. The release distance is then

$$R_r = (qaa_0)^{1/2}(\frac{v_0}{v_e}), \tag{8}$$

with $v_0=e^2/\hbar$ and $a_0 =\hbar^2/(me^2)$ being the first Bohr velocity and radius, respectively. Consequently, release occurs at distances less than R_r.

If the potential energy of the target electron in the field of the projectile is numerically larger than the kinetic energy of the electron in the frame of the projectile, capture to the projectile occurs. The condition for this is

$$\frac{qe^2}{R_c} > \frac{1}{2}mv^2 \tag{9}$$

where v is the projectile velocity. Therefore, the capture distance is

$$R_c = 2qa_0(\frac{v_0}{v})^2. \tag{10}$$

If $R_c > R_r$ and release occurs, capture must necessarily happen too, and the capture cross section is the the cross section for the release process (Knudsen et al., 1981):

$$\sigma^{01}_{q,q\,1} = \pi R_r^2 = \pi a_0^2 q \left(\frac{a}{a_0}\right)\left(\frac{v_0}{v_e}\right)^2 \tag{11}$$

In this case the result is independent of the projectile velocity. If $R_r > R_c$ and release occurs, capture does not necessarily occur. In this case, the scattering cross section is the cross section of the capture process weighted with the probability per unit time of the order of (v_e/a) and the time during which capture can occur (R_c/v) (since capture is a gradual process):

$$\sigma^{01}_{q,q\,1} = \pi R_c^2 \left(\frac{v_e}{a}\frac{R_c}{v}\right) = 8\pi a_0^2 q^3 \left(\frac{a_0}{a}\right)\left(\frac{v_e}{v_0}\right)\left(\frac{v_0}{v}\right)^7 \tag{12}$$

(Knudsen et al., 1981). The release distance scales like $q^{1/2}$ (Eq. 8), while the capture distance scales like q/v^2 (Eq. 10), so that the condition $R_c > R_r$ is likely to prevail in the limit of high projectile charges and low projectile velocities. Therefore, in this limit we expect the cross section to be proportional to q and constant in impact energy (Eq. 10), while at higher energies and lower charges we expect the cross section to scale like q^3/v^7 (Eq. 12). The cross sections in Eqs. 10 and 12 are strictly valid for capture only from a one-electron atom; however, by integrating over the electron density and velocity distribution, cross sections for a many-electron target can be obtained. This, however, does not change the scaling for q and E.

There are two limitations to this classical model; first, the projectile charge after capture has to be high enough to warrant the assumption of quasi-continuum of states, and secondly, the projectile velocity has to be small enough to ensure that quantum effects can be neglected. These requirements lead to the Bohr condition Eq. 1.

Binary Collision Model

Another model for single electron capture is the binary collision model, originally proposed by Thomas (1927). A discussion of this model can be found in McDowell and Coleman (1970) and Briggs and Taulbjerg (1979). In this model $H^+ + H$ collisions are considered and the capture cross section is calculated under the assumption that the electron to be captured undergoes two collisions. First, it is first deflected from the projectile nucleus through an angle of 60° to the beam direction, thereby assuming the projectile velocity, and then it scatters off the target nucleus into the beam direction. Then it has the velocity and the direction of the projectile and can be captured. The cross section obtained by Thomas (1927) for a light projectile and a light target scales as

$$\sigma^{01}_{q,q-1}(Thomas) \propto v^{-11}.$$

McDowell and Coleman (1970), however, discuss a calculation by Bates and Mapleton (1966) for the classical Thomas model that predicts a cross section scaling of

$$\sigma^{01}_{q,q\ 1}(Bates\text{-}Mapleton) \propto v^{\ 9} \qquad (14)$$

but caution that this classical approach might not be suitable for the capture from light

atoms because the charge distribution used in this model may not be correct. A quantum-mechanical evaluation of the cross section (Briggs and Taulbjerg, 1979) yields

$$\sigma^{01}_{q,q\,1}(Briggs\text{-}Taulbjerg) = \frac{2^7\pi^2 Z_1^5 Z_2^5}{Z_1+Z_2} v^{\,11}, \qquad (15)$$

where Z_1 and Z_2 are the charges of the projectile and the target, respectively. This latter scaling in v agrees with the classical calculation by Thomas (1927).

If the target atom contains two electrons, the electron to be captured ("active electron") can undergo collisions not only with the target nucleus but also with the other target electron ("passive electron"). In this model, for which a quantum-mechanical description has been given by Briggs and Taulbjerg (1979), the active electron undergoes two collisions, one with the bare projectile nucleus and the other one with the passive electron. The active electron is first deflected from the projectile nucleus at 45° (as opposed to 60° as in the case discussed in the previous paragraph) to the beam direction, thereby assuming the beam velocity, and is then scattered off the passive electron into the beam direction. It can then be captured by the projectile while the passive target electron recoils perpendicular to the beam direction. Experiments indeed show a peak in the recoil ion spectrum at 90° to the beam direction (Briggs and Taulbjerg, 1979).

These authors also calculate the Thomas capture cross section for H^+ + He collisions, assuming that the nuclear motion can be treated classically and that the helium target ground state can be represented by hydrogenic wavefunctions and electrons without exchange interaction. Using these assumptions, they arrive at

$$\sigma^{01}_{q,q-1}(Briggs\text{-}Taulbjerg) = \frac{2^4\pi^2 Z_1^5 Z_2^3}{Z_1 + \sqrt{2}\, Z_2} v^{-11}\ a.u., \qquad (16)$$

where Z_1 and the Z_2 are the projectile and target nuclear charge, respectively, and v is the projectile velocity. Eq. 16 is valid for the case where the captured electron is scattered off the passive target electron, while Eq. 15 is valid when the captured electron is scattered off the target nucleus.

Born Approximation

The Born approximation for single electron capture is based on the cross section for a rearrangement collision (McDowell and Coleman, 1970)

$$\sigma^{01}_{q,q-1}(Born) = \frac{\mu\mu_f}{4\pi^2\hbar^4}\frac{k_f}{k_i}\int |T_{fi}|^2 d\Omega, \qquad (17)$$

where μ_i, μ_f, k_i, and k_f are the initial and the final reduced projectile mass and the initial and the final relative momenta, respectively. The projectile is assumed to be a bare ion and the wavefunctions of the target electrons are assumed to be hydrogenic to simplify the calculations. The main difference between various Born approximations, as demonstrated by McDowell and Coleman (1970), lies in the choice of the approximation for the matrix element $|T_{fi}|$.

The earliest model describing single capture for a bare projectile impacting on a hydrogenic target was brought forth by Oppenheimer (1928) and by Brinkman and

Kramers (1930) and is called the OBK model. This model is a first Born approximation where the internuclear potential between the projectile and the target nucleus is neglected and only the Coulomb potential of the target (with nuclear charge Z_2)is taken into account:

$$|T_{fi}| = \langle \Psi_f | -\frac{Z_2}{r} | \Psi_i \rangle, \tag{18}$$

with the Ψ's being products of hydrogenic bound state wavefunctions and plane waves. In the high-energy limit (E≳ 0.1 MeV/u) this leads to the following scaling:

$$\sigma^{01}_{q,q\,1}(OBK) \propto (Z_1 Z_2)^5 v^{\,12}, \tag{19}$$

where v and Z_1 are the the projectile velocity and charge, respectively.

Bates and Dalgarno (1952) and Jackson and Schiff (1953) published an extension of the OBK model by introducing the internuclear potential into the matrix element. This model is commonly called the first Born approximation and leads to the same charge and velocity dependence but with the coefficient:

$$\sigma^{01}_{q,q\,1}(1B) = 0.661 \times \sigma^{01}_{q,q\,1}(OBK). \tag{20}$$

This model was extended to helium targets by Mapleton (1961) and it was shown that the velocity scaling remains the same.

The second Born approximation was originally proposed by Drisko (1955), and a summary has been given by McDowell and Coleman (1970). In addition to the internuclear potential introduced in the first Born approximation, the interaction between

the electron and the projectile is also taken into account. Physically, this corresponds to two Thomas scattering processes, namely, the projectile nucleus - target electron and the subsequent target nucleus - target electron collision (Shakeshaft, 1974). At high energies this model yields the same velocity (v^{-11}) and projectile charge (Z_1^5) scaling:

$$\sigma_{q,q\ 1}^{01}(2B) = (0.2946 + \frac{5\pi v}{2^{12}})\sigma_{q,q\ 1}^{01}(OBK), \tag{21}$$

Double Ionization

No Projectile Charge Change

The scattering amplitude for ionization is the matrix element of the interaction energy between the projectile and the target:

$$a = \langle \Phi^f | V | \Phi^i \rangle \tag{22}$$

For single ionization this can be calculated using the Born approximation (McDowell and Coleman, 1970 and McGuire, 1982):

$$a_{q,q}^{01} \propto \frac{Z}{v} \tag{23}$$

leading to a cross section which can be expressed as (see Eq. 6) (McGuire, 1982)

$$\sigma_{q,q}^{01} \propto (\frac{Z}{v})^2 \ln (Cv), \tag{24}$$

where Z and v are the charge and the velocity of the projectile, respectively, and C is a constant. For double ionization the scattering amplitude can therefore be expanded in

terms of Z/v (McGuire, 1982, 1991, and McGuire et al., 1995):

$$a_{q,q}^{02} = c_1\frac{Z}{v} + c_2(\frac{Z}{v})^2, \tag{25}$$

with c_1 and c_2 being complex constants.

Double ionization in helium can be analyzed using many-body perturbation theory (McGuire, 1982, 1987, 1991, & McGuire et al., 1995) to determine the contributions shown in Figure 1. These contributions are not sharply distinguishable physical processes but rather correspond to Feynman diagrams that have to be summed up to compute the constants c_1 and c_2.

Shake-Off (SO): This contribution is due to an electron-hole interaction after the collision. After the first electron is knocked out fast by the projectile, the wavefunction, along with its eigenenergies, changes so that the second electron (which remains in its original energy level) is not in an eigenstate of the ionic wavefunction. It can then be ejected. As Andersen et al. (1987) point out, SO is valid only if there is not more than one interaction of the projectile with the target electrons. If the projectile interacts with both electrons or twice with one electron, TS terms are needed.

Ground-State Correlation (GSC): This refers to the electron-electron interaction in the ground state.

Two-Step-1 (TS1): This contribution is due to an electron-electron interaction after the collision. The electron that is hit by the projectile collides with the second electron and removes it.

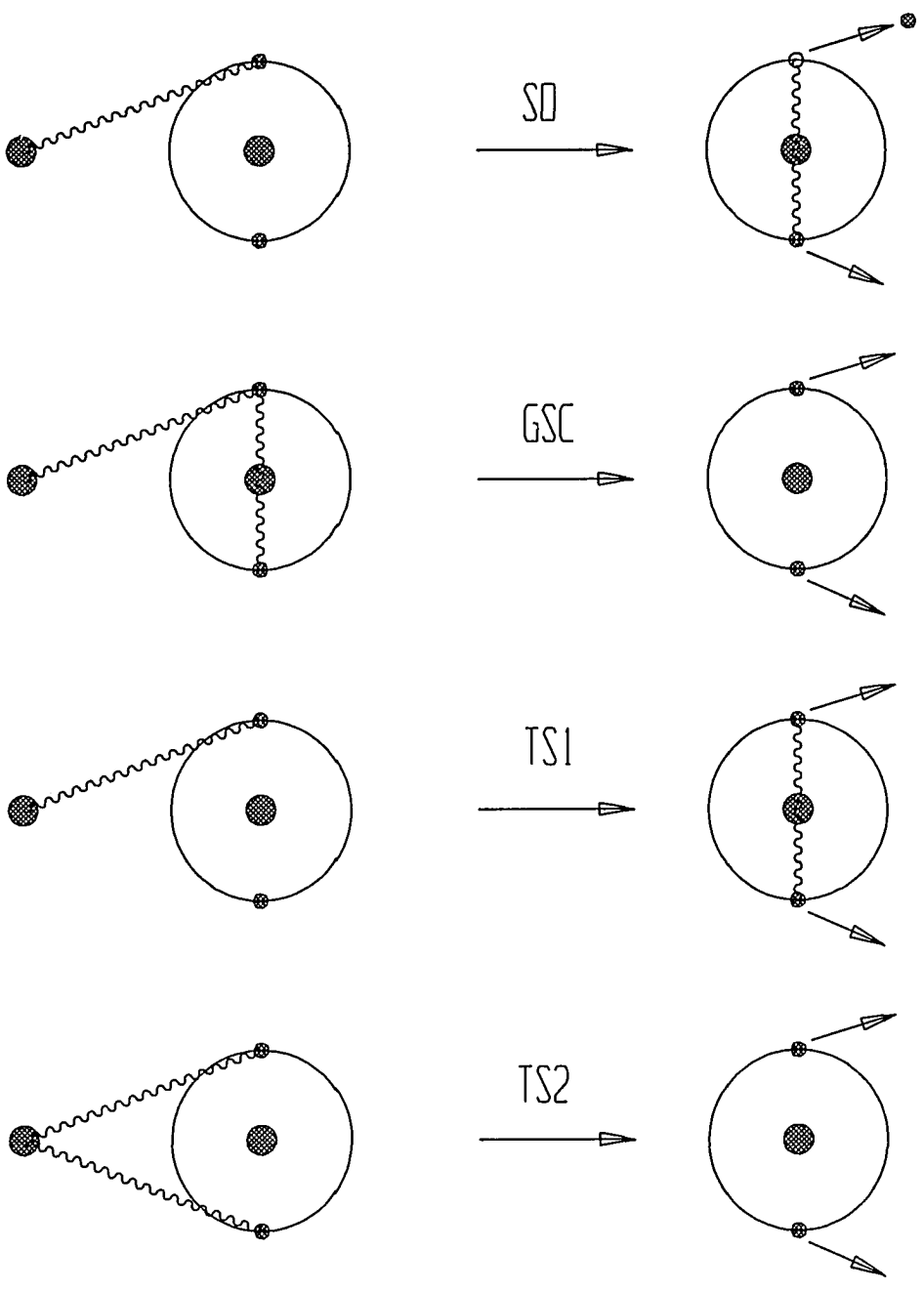

Note: First-order in Z/v: shake-off (SO), ground-state-correlation (GSC), and two-step 1 (TS1); second-order in Z/v: two-step 2 (TS2).

Figure 1. Four Different Double Ionization Mechanisms.

Two-Step-2 (TS2): This is a process in which the projectile interacts with each target electron separately. The electron-electron interaction does not take place here.

The first three processes, which involve a single projectile nucleus - target electron interaction, are first order in Z/v and allow the calculation of the constant c_1, while TS2, which involves two projectile nucleus - target electron interactions, is second order in Z/v and allows the calculation of c_2. McGuire (1987 and 1991) differentiates further between static correlation (SO) and scattering interaction (GSC, TS1) for the above processes that include electron-electron interactions. Static correlation is expressed in the asymptotic initial and final wavefunctions and is independent of the collision velocity, while scattering correlation is included in the scattering operator and depends on the collision dynamics. It is speculated that, experimentally the first-order correlation processes cannot be distinguished and they are therefore collectively referred to as SO (Végh and Burgdörfer, 1990, and Andersen et al., 1987).

The cross section for the SO process is the product of the single ionization cross section (McDowell and Coleman, 1970) and a constant depending on the overlap of the initial and the final target wavefunctions (which is independent of the collision dynamics):

$$\sigma_{q,q}^{02}(SO) = c_1(\frac{Z}{v})^2 \ln (c_2 v) \times |\langle \Phi_f | \Phi_i \rangle|^2 \qquad (26)$$

(with c_1 and c_2 being constants), while the cross section for the TS2 process is the product of two independent projectile-electron collisions:

$$\sigma_{q,q}^{02}(TS2) \propto (\frac{Z}{v})^4 , \qquad (27)$$

Ignoring interference between SO and TS2, the ratio of the total double-to-single ionization cross sections can be written from Eqs. 24, 26, and 27 as

$$R_{q,q} = A + B\left(\frac{Z}{v}\right)^2 \frac{1}{\ln(Cv)}, \tag{28}$$

where the first term is the high-energy SO limit and the second term expresses the independent electron TS2 process (Knudsen et al., 1984). Knudsen et al. (1984) compiled data for a wide range of fully-stripped projectiles colliding with helium and determined the fitting parameters A, B, and C:

$$R_{q,q} = 2.2\times10^{-3} + 4.55\times10^{-3} \times \frac{q^2}{E \ln(13.12\sqrt{E})}, \tag{29}$$

with q being the charge of the projectile and E the energy in MeV/u.

Single Electron Capture to the Projectile

Double ionization in coincidence with single electron capture to the projectile is called transfer ionization (TI). For $q/v \lesssim 1$, TI can be calculated using perturbation theory; much like the case of direct double ionization, it can be distinguished between two direct encounters between the projectile and the target electrons (independent electron approximation) and processes in which the ionization and capture are correlated.

The former process is called a first Born ("1B", Knudsen et al., 1987) or "direct" (McGuire et al., 1987) process in which both electrons interact independently with the projectile. It is analogous to TS2 in the case of direct double ionization. The cross

section can then be expressed as a product of the capture and the ionization cross sections:

$$\sigma^{02}_{q,q\,1}(1B) \propto \sigma^{01}_{q,q\,1} \times \frac{q^2}{v^2}. \qquad (30)$$

The latter process is called a second Born process ("2B", Knudsen et al., 1987) which includes electron correlation and can be subdivided into a "2B1" and a "2B2" process.

In the 2B1 process the projectile hits one of the target electrons which scatters off the target nucleus and is ejected into the direction of the projectile, resulting in single capture. This can be followed by ionization through rearrangement. Therefore, this mechanism is analogous to SO in the case of direct double ionization; McGuire et al. (1987) call this a "static interaction" because the correlation is contained in the asymptotic wave functions of the final and the initial states. The cross section is proportional to the single capture cross section and the ionization (through the overlap between the initial and the final wave function) (McGuire et al., 1987):

$$\sigma^{02}_{q,q\,1}(2B1) \propto \sigma^{01}_{q,q\,1} \; |\langle \Phi_{final} | \Phi_{initial} \rangle|^2. \qquad (31)$$

In the 2B2 process the projectile hits the first target electron which is then scattered off the second one, resulting in single capture. Subsequently, the second electron is ejected from the target with the same speed as the projectile. This has its direct double ionization analog in the TS1 process where the second electron is ejected after interacting with the first one. The electron-electron interaction in this case occurs

during the collision, which is why Knudsen et al. (1987) and McGuire et al. (1987) term this "scattering correlation". The cross section can be expressed as (McGuire et al., 1987):

$$\sigma^{02}_{q,q\ 1}(2B2) \propto \sigma^{01}_{q,q\ 1}\ \frac{1}{v^4}. \tag{32}$$

Thus, 2B2 is expected to be most important only at lower velocities where the electrons have sufficient time to interact.

In the low energy region where the first Born (1B) process is dominant, the TI fraction of helium is expected to scale as in the case of direct double ionization (e.g., Tanis, 1989). This can be seen from Eq. 30 where $\sigma^{01}_{q,q-1}$ cancels out:

$$R_{q,q\ 1} \propto (\frac{q}{v})^2. \tag{33}$$

For the high energy regime where the 2B1 processes is dominant, Knudsen et al. (1987) give this relation for the TI fraction of helium:

$$R_{q,q\ 1} = R_{\gamma} + \frac{q + Z_2}{8Z_2^2\ (q + \sqrt{2}\ Z_2)}, \tag{34}$$

where R_{γ} = 3.4% (double-to-single photo ionization ratio), Z_2 is the target nuclear charge and q is the projectile charge.

EXPERIMENTAL PROCEDURE

This work was done using the tandem Van de Graaff accelerator at Western Michigan University (Figure 2) (Forest, 1991). A cathode of LiF in a SNICS (Source of Negative Ions by Caesium Sputtering) was used to produce a beam of Li^- ions which were directed towards the high-voltage terminal of the accelerator. Here the negative lithium ions were stripped of some of their electrons to Li^+, Li^{2+}, or Li^{3+} and then accelerated a second time. The 90° analyzing magnet selected the beam of the desired charge state and energy which was then directed into the atomic physics beam line (the rightmost beam line in Figure 2) towards the collision chamber.

Two types of measurements have been made with this setup: "singles" measurements where the total yields for single loss, double loss, and single capture by the $Li^{1,2,3+}$ projectiles have been determined without knowledge of the final charge state of the He target atoms, and "coincidence" measurements where single and double ionization of the He target was associated with single or double loss, single capture, or no charge change by the incident $Li^{1,2,3+}$ projectiles.

Singles Measurements

In the singles experiment, the number of reaction products has been measured for each projectile charge state and impact energy at different gas pressures under single-collision conditions. A schematic of this setup is shown in Figure 3; in this part of the

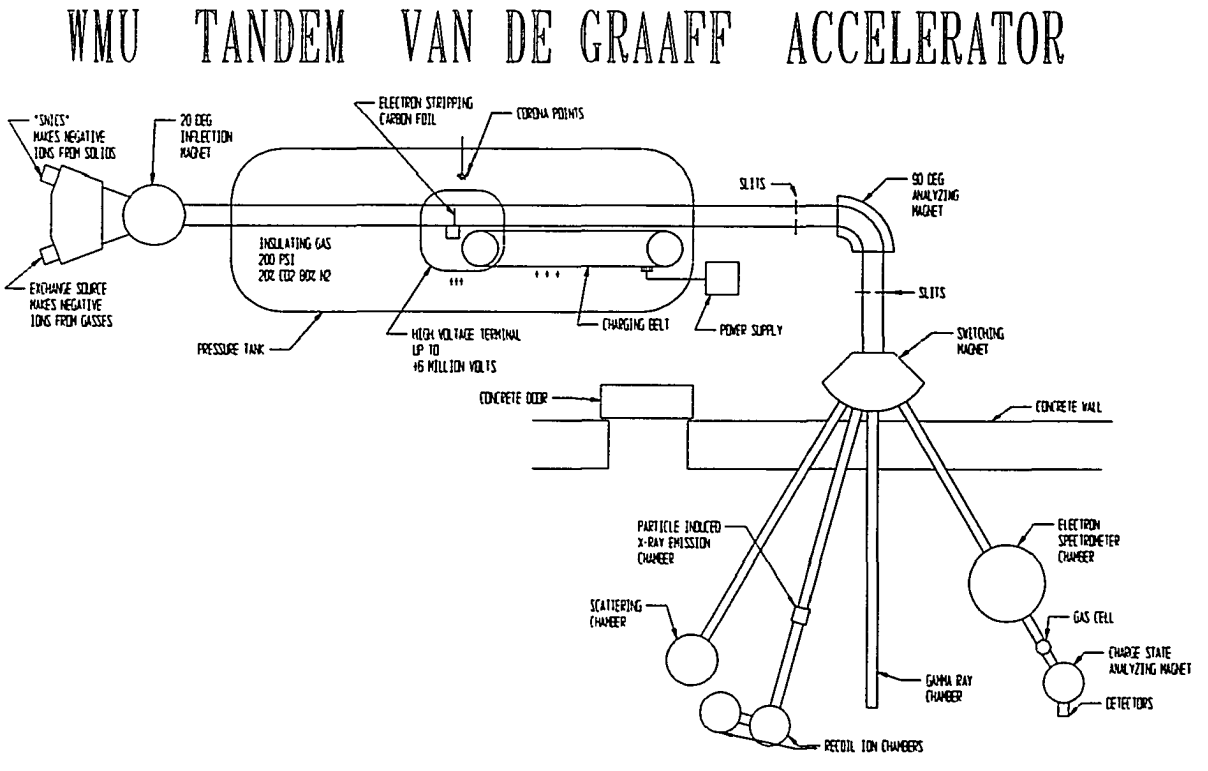

Figure 2. Schematic of the Western Michigan University Tandem Van De Graaff Accelerator Laboratory (Ferguson, 1995).

experiment, however, the recoil-ion detector, and, consequently, the coincidence setup shown in the figure was not used.

The Li^{q+} (q=1,2,3) projectiles are directed into the collision chamber where they collide with the helium target gas. Outgoing $Li^{0,1,2,3+}$ reaction products first travel through a magnet that separates the charge states and then are counted. All charge states except the main beam are directed into solid-state surface barrier detectors which count each incident particle. They were operated with a maximum of about 50,000 impacting

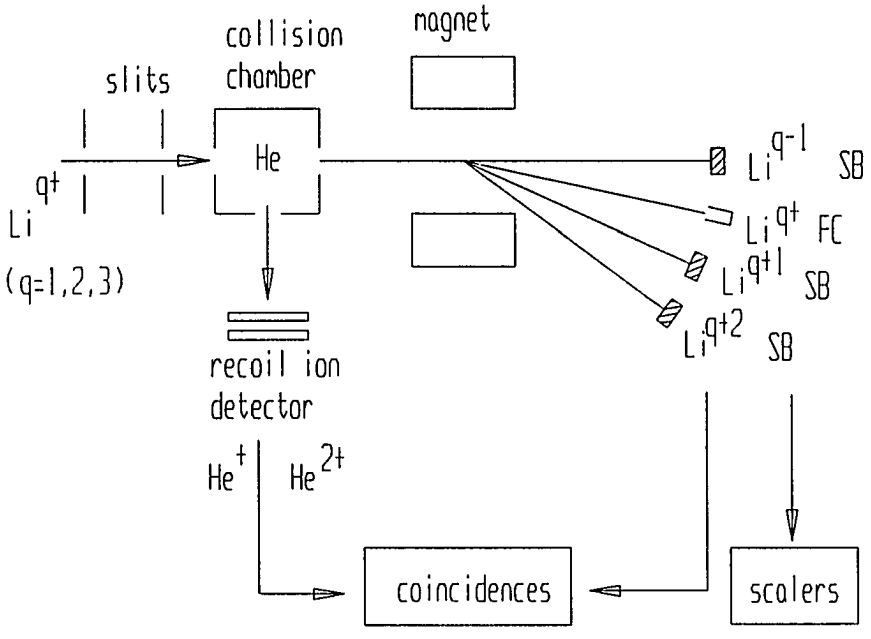

Note: SB denotes a surface barrier detector and FC denotes a Faraday cup. For the singles measurements the recoil ion detector and the coincidence setup was not used.

Figure 3. Schematic of the Experimental Arrangement.

particles per second (≈ 0.01 pA for a singly charged particle beam) to avoid pileup. The main beam, due to its higher intensity, was collected by a Faraday cup that does not have a restriction on the incoming current. The electronics setup that counts the incoming particles is shown in Figure 4. In the branch for the main beam (unchanged projectile charge state), a Keithley electrometer measures the charge in the Faraday cup (FC). A full scale current gives a 2 V dc output which is dropped across a 1 MΩ resistor, thereby converting the voltage output to a current output. A digital current integrator (DCI) then converts this current to digital logic pulses which are counted with a scaler. In the charge-changed particle branch, the surface barrier detector (SB) puts out one pulse for each impacting particle. This pulse is sent through a preamplifier, an amplifier, a constant-fraction discriminator (CFD) and is registered by a scaler.

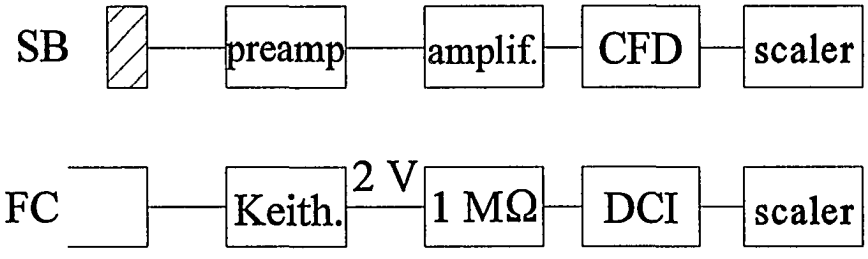

Note: Separate channels were used for the surface barrier dectectors (SB) for q-1, q+1, q+2, and q. The main beam was measured in the Faraday cup (FC).

Figure 4. Schematics of the Electronics for Particle Counting and Beam Integration.

Coincidence Measurements

In the coincidence experiment, data for $Li^{1,2,3+}$ have been taken for the same energy ranges as in the singles measurements. A schematic of the setup is also shown in Figure 3 where now the recoil-ion detector is used. In order to detect coincidences between the target reaction products (He^{+} or He^{2+}) and the different outgoing charge states of the beam (q-1, q, q+1, and q+2), the recoil ion detector was used. The collision chamber and the recoil ion detector are shown in detail in Figure 5. Recoil ions produced in the collision region are accelerated between a +900 V grid and a 0.8 cm diameter, negatively biased (-900 V) cylindrical aperture and then travel through the field-free region and through another aperture (biased to -100 V) towards the negatively biased (-1900 V) microchannel plate (MCP). The second aperture serves to shape the electric field in order to produce a cleaner time-of-flight spectrum. The detector is designed so that all ions of the same mass-to-charge ratio produced in the collision region have approximately the same time of flight to the MCP, so that ions of different mass-to-charge ratios can be easily distinguished.

The electronics for processing the signals from the recoil-ion detector and the surface barrier detectors are shown in Figure 6. This diagram has three branches: q±n (n=1,2), q, and recoil. The recoil branch processes signals from the recoil-ion detector, the q branch processes the main beam signal coming from the Faraday cup, and the q±n branch processes beam particles detected in the surface barrier detectors.

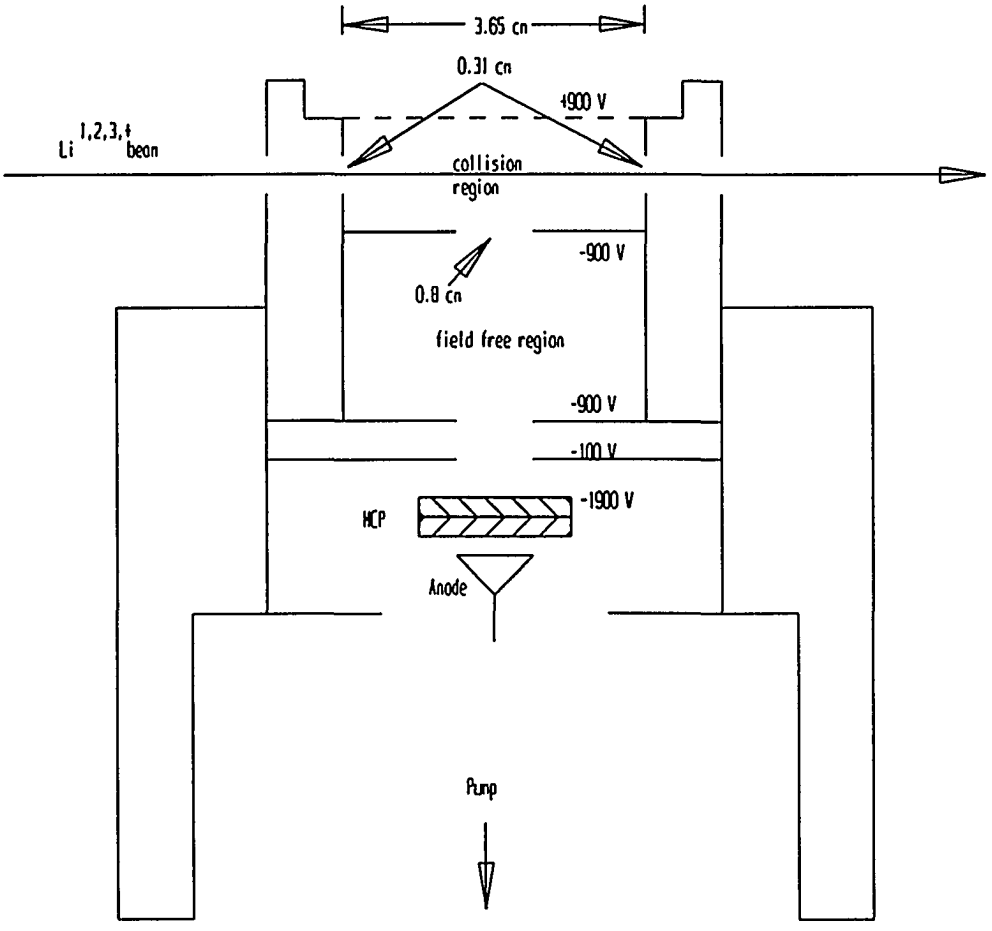

Figure 5. Schematic of the Collision Chamber and the Recoil-Ion Detector Detector.

After a collision takes place, the resulting He^{+} or He^{2+} ion is extracted and accelerated into the recoil-ion detector where a signal from the microchannel plate (recoil) is sent through a fast timing amplifier (FTA), a timing filter amplifier (TFA), and a constant-fraction discriminator (CFD) to the time-to-amplitude converter (TAC). The corresponding beam particle, which strikes one of the solid-state detectors (q±n) at the end of the beamline (see Figure 3), is also sent to the TAC through an amplifier (TFA), a delay (in this case, 300 nsec), and a CFD. The delay was adjusted so that both signals

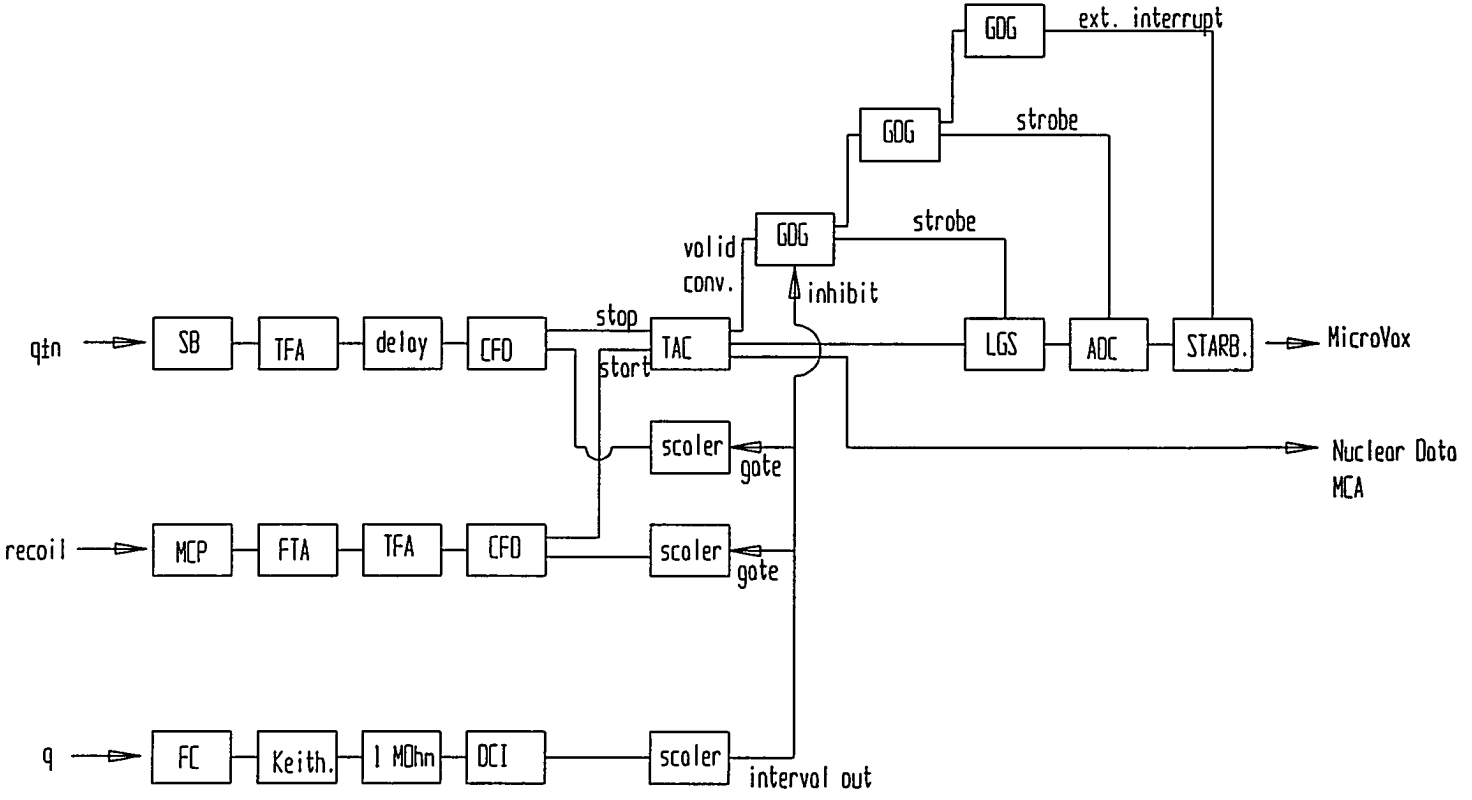

Figure 6. Electronics Setup for the Coincidence Measurements.

arrive at the TAC within the full-scale range selected (in this case, 2 μsec).

Every time a He ion is detected, there should be a corresponding Li particle, so the TAC is started by a He ion signal and stopped by a Li signal that arrives within 2 μsec. (Li particles that stop the TAC without having undergone a collision with the He ion that started the TAC appear as background in the TAC spectrum). The TAC then converts the time difference between the START and the STOP signals to a voltage between 0 V and 10 V. This timing information was sent to a PC-based multi-channel analyzer (MCA) where a counts vs. time spectrum could be displayed.

The TAC spectrum was also displayed using the CHAOS data acqusition software running on a MicroVAX computer using a STARBURST interface. In this case, the electronics was more complicated because CHAOS uses a CAMAC analog-to-digital converter (ADC), which takes its input from a linear-gate-stretcher (LGS) to shape the incoming pulse. Both of these modules, as well as STARBURST itself, have to be strobed; this strobing is done with the gate delay generators (GDG). If the TAC detects a valid conversion (start and stop arrive within 2 μsec), a strobe is sent to the first GDG which strobes the LGS. The second GDG strobes the ADC. The third GDG gives the ADC the time it needs to complete the conversion (≈80 μsec) and provides an external interrupt for STARBURST to signal that an event has taken place.

The main beam scaler (q branch) was used as the "master counter" which starts and stops the data acquistion. The INTERVAL OUT from this scaler was connected to the GATE inputs of the recoil scaler (recoil branch), the charge-changed particle scalers (q±n branches), and to the INHIBIT input of the first GDG. Thus, it starts and stops all

other ("slave") scalers and inhibits the strobing of the LGS, the ADC, and STARBURST which, in turn, stops the data acquisition.

The particle detectors were operated with less than 50,000 counts per second corresponding to about 0.01 pA for a singly charged particle beam. This low beam current required that the experiment be run in two steps for each incident projectile energy and charge state. In the first step, coincidences between the recoiling helium target ions and the charge-*changed* projectiles q+1, q+2, and q-1 were measured for a beam current of about 1 pA. For this current, the particle rate in the SB detectors was about 50 kHz and the 1 pA main beam was collected in the Faraday cup. (For the conversion from the collected Faraday cup charge to the number of incoming beam particles, refer to the discussion of the singles measurements). In the second step, coincidences between the helium target ions and the *unchanged* charge state main beam projectiles of charge q were measured. In this case the beam current had to be reduced to about 0.01 pA because the main beam was directed into one of the SB particle detectors in order to observe the coincidences.

DATA ANALYSIS

Determination of the Cross Sections

The number I_{react} of particles undergoing a collision reaction is given by

$$I_{react} = I_0 \sigma T \epsilon, \tag{36}$$

where I_0 is the total number of incoming particles, σ is the cross section for the reaction in cm^2, ϵ is the detection efficiency, and T is the target thickness in atoms/cm^2. T can be expressed in terms of the pressure p (in mTorr) and the target cell length l (in cm):

$$T = N_0 p l, \tag{37}$$

with N_0=3.3*10^{13} atoms/cm^2 (at room temperature). Therefore, the cross section can be expressed as

$$\sigma = \frac{1}{\epsilon} \frac{1}{N_0 l} \frac{\Delta F}{\Delta p}, \tag{38}$$

where $F=I_{react}/I_0$ is the fractional yield, i.e., the ratio of reaction products to the total number of incoming particles. In order to obtain the cross section, the fractional yield F is plotted versus the pressure p. Under single-collision conditions, i.e., when the probability for more than one interaction during passage through the collision region is negligibly small, the fractional yield is proportional to the pressure which leads to a

straight line in the fractional yield-pressure diagram. Then the slope $\Delta F/\Delta p$ can be used to determine the cross section from Eq. 37.

Singles Measurements

Total charge-changing cross sections were obtained for 0.5 - 8 MeV Li^{+}, 3 - 16 MeV Li^{2+}, and 3 - 20 MeV Li^{3+} + He collisions. For each projectile charge state and energy, data were taken for target gas pressures in the range 0 - 100 mTorr; for single capture to Li^{3+} at energies above 10 MeV, target gas pressures up to 200 mTorr were also used. For each reaction channel investigated (single loss, double loss, and single capture), the total number of projectile-charge-changing events I_{react} was counted with a scaler (Figure 3) while the number of projectiles in the incident charge state (no charge change) was determined from the total charge collected in the Faraday cup in the manner described in the previous chapter. The recoil-ion detector was not used in this part of the experiment. The reaction counts I_{react} and the total number of impacting particles I_0 were used to determine the fractional yield for each target gas pressure. This fractional yield was then plotted versus the target gas pressure to determine the slope $\Delta F/\Delta p$. A typical example is shown in Figure 7.

The efficiency ϵ of the surface-barrier detectors is 100%. However, the pressure in the gas cell is not constant over the entire reaction length due to the entrance and the exit slit apertures. The effect of these apertures on the target length can be taken into account as follows (Ramsey, 1956):

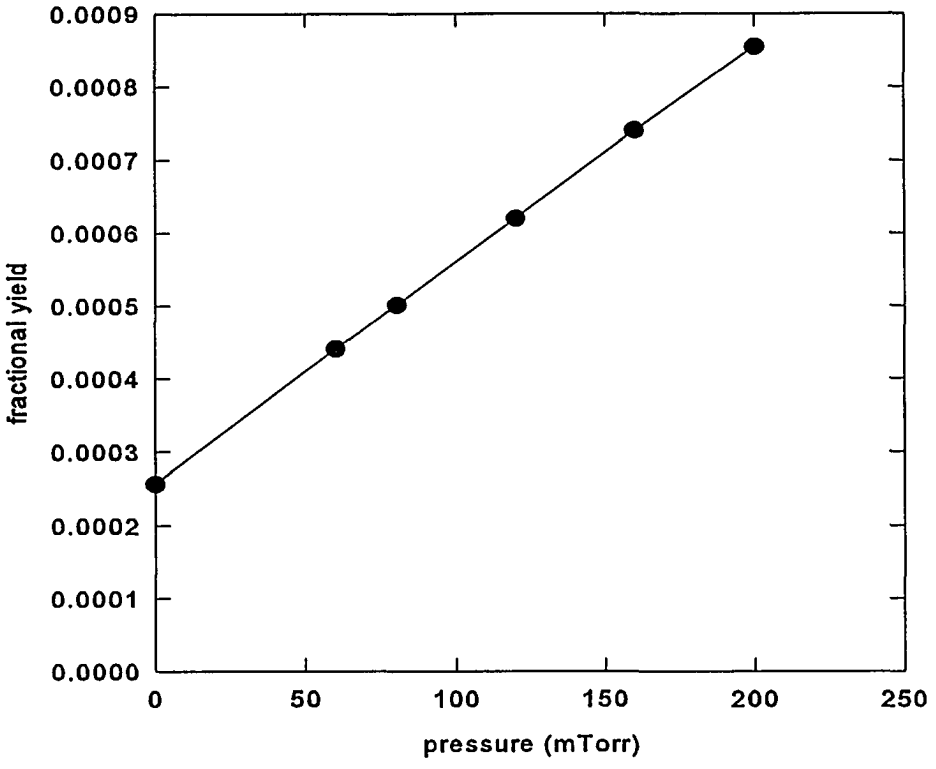

Note: The linearity of the plot indicates that the data have been taken under single-collision conditions.

Figure 7. Fractional Yield vs. Pressure for Single Electron Capture to Li^{3+} at 12 MeV.

$$l = l_{geom} + \frac{(C_1 + C_2)}{\sqrt{2}}, \tag{39}$$

where C_1=0.31 cm and C_2=0.31 cm are the entrance and the exit slit diameters (Figure 5) and l_{geom}=3.65 cm is the geometrical length of the gas cell. Therefore, l=4.08 cm. The efficiency ϵ, the effective target cell length l, and the slope were then used in Eq. 37 to calculate the cross section for each reaction channel at each energy.

Coincidence Measurements

Cross Sections

Measurements of the coincidence cross sections were carried out for each projectile charge state ($Li^{1,2,3,+}$) and reaction channel (single and double loss, single capture, and direct ionization) at impact energies in the range 2 - 8 MeV for Li^{+}, 3 - 16 MeV for Li^{2+}, and 3 - 20 MeV for Li^{3+}. Each of these measurements was done for target gas pressures in the range 0 - 1 mTorr. As in the case of the singles experiment, the total number of projectile-charge-changing events at each energy and pressure were recorded by scalers (Figure 3) and the main beam intensity was determined from the charge collected in the Faraday cup.

For the measurements of the coincident events, i.e., for counting the number of projectiles with a given post-collision charge state in coincidence with a given He target charge state, the recoil-ion detector (Figure 5) described in the previous chapter was used. This detector uses the time-of-flight technique to distinguish between particles with different charge-to-mass ratios. A typical time-of-flight spectrum is shown in Figure 8. This spectrum shows the number of He^{+} and He^{2+} ions associated with projectile single capture for 6 MeV Li^{2+} at 1 mTorr versus the time difference between the START and the STOP pulses received by the TAC, i.e., between the arrival of the signal from the target He ion in the recoil-ion detector and the signal from the corresponding Li particle in the solid state detector. The time-of-flight for a projectile ion from the collision region to the solid state detectors is constant (because it depends only on the beam energy), so

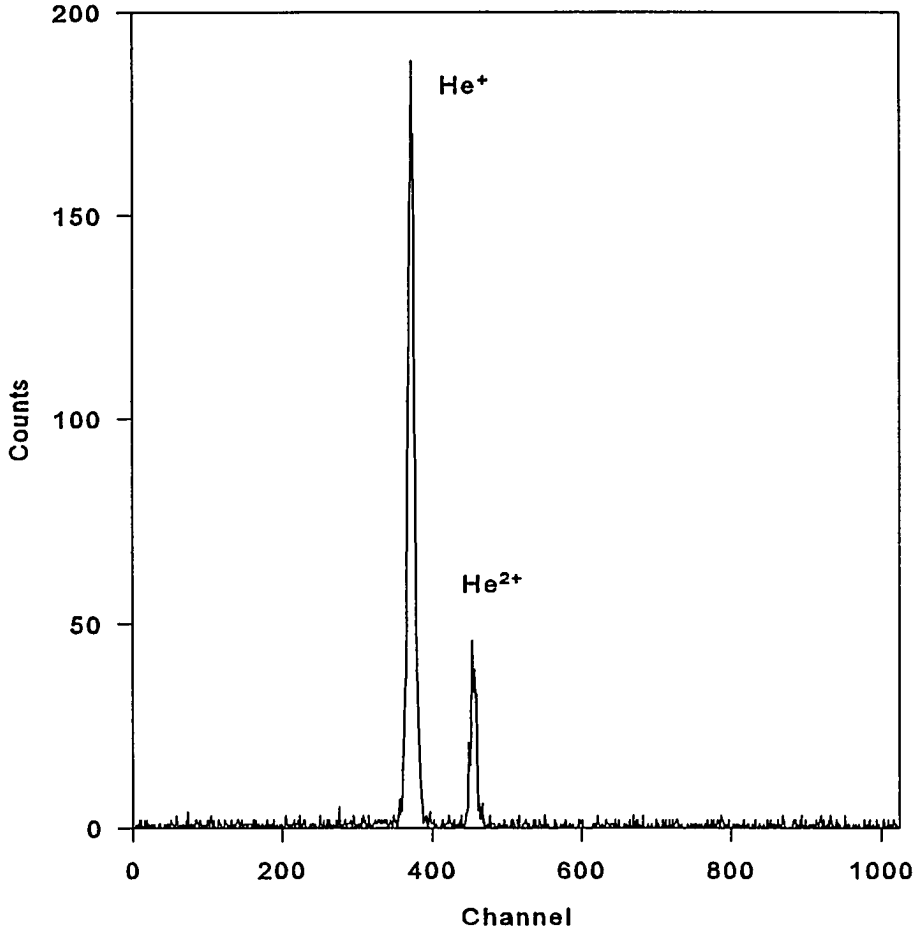

Figure 8. Coincidence Time-Of-Flight Spectrum for He Target Ionization Associated With Single Electron Capture From He to Li^{2+} at 6 MeV and 1 mTorr.

that the arrival of the STOP signal is constant for a given energy, while the time-of-flight for a recoiling target ion to the MCP depends on the charge-to-mass ratio of the extracted ion. The faster the ion travels, the earlier the START signal arrives, and the greater the time difference becomes. Thus, the peak representing the fastest ions (He^{2+}) are on the right side of the spectrum.

Such a spectrum was obtained for each reaction channel and for each incident projectile charge state, energy, and pressure. The number of counts in the single and the double He ionization peaks were determined by integrating the peaks and subtracting the background. From the number of "real" counts in each peak and the total number of incident particles, the fractional yield could be determined for the double and the single ionization of the He target, and this fraction was plotted versus the target gas pressure in order to calculate the cross sections for a given projectile energy, charge state, reaction channel, and target ionization state.

The effective target gas cell length in the case of the coincidence measurements differed from that in the case of the singles measurements. The recoil-ion detector restricts the length of the "active" region in which collisions can be detected by the size of the aperture through which the helium ions are extracted into the detector (Figure 5). This active area is 0.8 cm long compared to 4.08 cm in the singles experiment. Therefore, in Eq. 37 l=0.8 cm is used.

Furthermore, while the detection efficiency of the surface barrier detectors is 100%, the intrinsic efficiency of the recoil ion detector is only about 50 % and this value must be determined experimentally. This will be discussed below.

Recoil-Ion Detector Efficiency

The determination of the recoil-ion detector efficiency was based on the fact that, for single electron capture in a helium target, the only two processes that can occur are single and double ionization of the target, i.e.,

$$\sigma_{q-1} = \sigma_{q-1}^{01} + \sigma_{q-1}^{02}, \tag{40}$$

with σ_{q-1}, σ_{q-1}^{01}, and σ_{q-1}^{02} being the cross sections for the total single capture, and single capture associated with single and double ionization of the target, respectively. (Particles measured in the other projectile reaction channels are not necessarily connected with any target ionization, and therefore the above equation does not apply to the direct ionization and the loss channels.) The total single capture cross sections have been determined from the singles measurements described above. Thus, the efficiency ϵ of the recoil-ion detector can be determined from the following relation:

$$\epsilon \times S_{q-1} = S_{q-1}^{01} + S_{q-1}^{02}, \tag{41}$$

where S_{q-1}, S_{q-1}^{01}, and S_{q-1}^{02} are the slopes in the fractional yield vs. pressure diagram for the total single capture and for single capture coincident with target single and double ionization, respectively. The efficiency calculated from Eq. 40 for all incident lithium charge states and all energies is shown in Figure 9. Although there is a slight indication of an increase in the efficiency with increasing projectile energy, the data of Figure 9 were averaged to give an overall efficiency of

$$\epsilon = 50\ (\pm 10)\ \%. \tag{42}$$

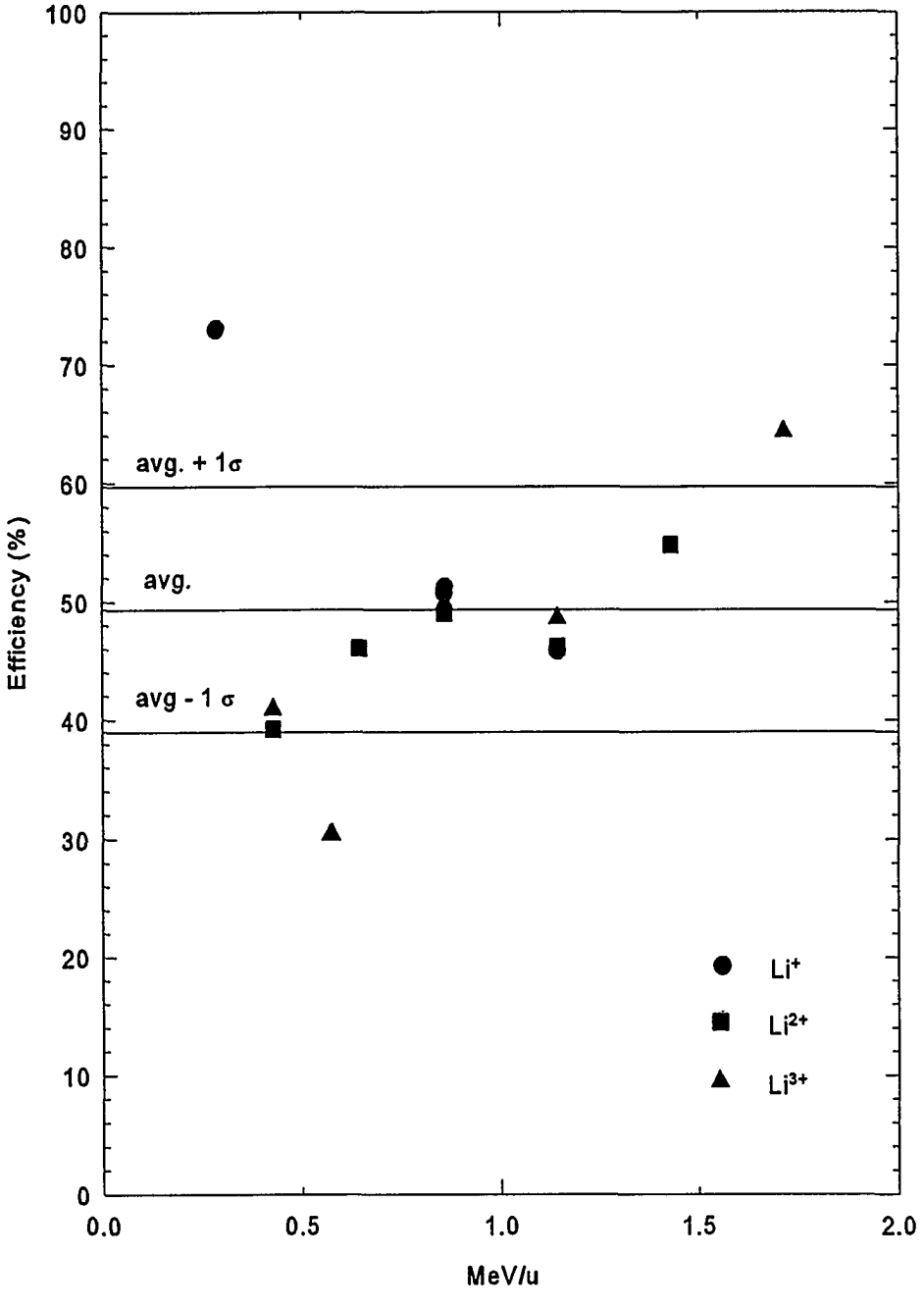

Note: Also shown are the average and the standard deviation values.

Figure 9. Efficiency of the Recoil-Ion Detector.

Double-to-Single Ionization Ratios

A quantity that is useful in the interpretation of this experiment is the ratio of double-to-single ionization:

$$R = \frac{\sigma^{02}}{\sigma^{01}}. \tag{43}$$

As explained in the theory chapter, this ratio exhibits the main features of the double ionization mechansims, since the single ionization effects tend to "cancel out". This quantity can be determined more accurately than the absolute coincidence cross sections since the detector efficiency cancels out in this ratio.

R has been calculated using two different methods. In the first method, R was determined directly from the number of counts for single and double ionization taken from the coincidence spectra. The counts in the single and the double ionization peaks for all measured pressures for a given energy and ionization channel were summed to determine the ratio. The error in this case is given approximately by the statistical uncertainty which is the square root of the total number of counts. In addition, the ratios were calculated for each individual pressure measurement and these values were than averaged. This method gives information about the reproducibility of the measurements since the ratios should be independent of the pressure if the experiment is carried out under single-collision conditions. In the second method, the coincidence cross sections were used to determine the ratios. Both of these methods yield results that are the same to within the experimental uncertainty.

Errors

Singles Cross Sections

As explained above, the cross sections are proportional to the slope of the fractional yield vs. pressure curve. In addition to statistical uncertainties, changes in experimental conditions such as fluctuations in the beam current or the target gas pressure can introduce random uncertainties. In general, the errors in fitting the fractional yield vs. pressure curves were about ±5%.

Systematic error is introduced from the uncertainty in the effective length of the gas cell. The geometrical length is 3.65 cm, while the correction for the non-uniform pressure distribution made by Eq. 38 is about 10% of the physical length. An error of about 20% for this correction is estimated, leading to a systematic error in the length of about 2%. Another systematic error is introduced from the inaccuracy of the pressure reading in the collision region. This error is assumed to be about 5%. A third systematic error is due to uncertainties in the reading of the charge of the main beam in the Faraday cup. Calibration of the Keithley electrometer with a constant current source showed that the current has a systematic error of about 4%. Systematic errors are uniformly positive or negative for all of the measured data.

In order to assign an error due to the reproducibility of the experimental results, the present results for the single capture and the single and double loss channels for Li^+ on He were compared to the corresponding results from measurements made in 1994 (Woitke et al.). The average deviation of the present results from the earlier ones at

energies 2, 4, and 6 MeV is approximately ±15%.

Coincidence Cross Sections

Before using the integrated double and single ionization peaks to calculate coincidence cross sections and ratios, the nature of the peaks in the time-of-flight spectrum has to be considered. The time scaling in the spectrum is proportional to $(m/q)^{1/2}$ so that all charged particles with the same mass-to-charge ratio appear at the same position in the spectrum and, hence, cannot be distinguished. This poses a problem for the He^{2+} peak, which has a mass-to-charge ratio of 2. If there is a non-negligible amount of H_2 in the collision region, the He^{2+} peak will appear larger because H_2^+ also has a mass-to-charge ratio of 2.

The most common background contaminations from which H_2^+ could originate are air, water vapor, H_2, and carbon compounds. Coincidence spectra of collisions of Li^+ with air (a), water vapor (b), and H_2 (c) have been taken at 0.36 MeV/u in the double loss channel and are shown in Figure 10 and are compared with the He target spectrum (d). Water vapor shows only an H^+ peak but no H_2^+ contribution which is expected considering the low dissociation energy of H_2 of 4.75 eV (Haken and Wolf, 1987) compared with the impact energy of 0.36 MeV/u. Air does not show an H_2^+ contribution either, because most of the hydrogen in air is expected to originate from water vapor. Carbon compounds have not been investigated but they seem an unlikely source of H_2^+.

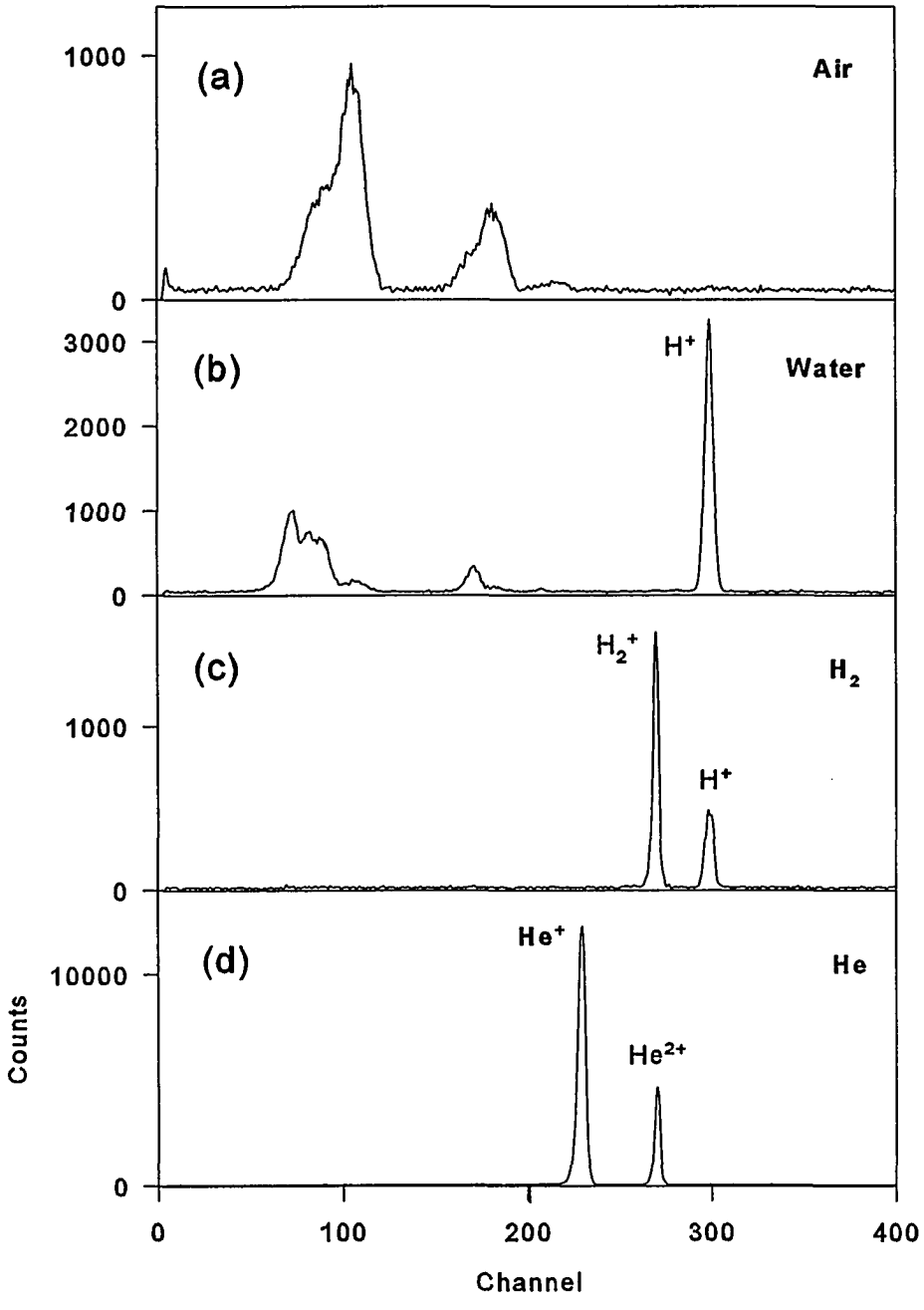

Figure 10. Coincidence Spectrum for the Double Loss Channel for Collisions Between Li^+ and He, H_2, Water, and Air at 0.36 MeV/u.

Since the H^+ in carbon compounds are usually bound to C or O ions, they are similar to the case of water molecules, hence are unlikely to recombine to H_2^+ or H_2 (with a dissociation energy of 4.75 eV) in collisions with MeV Li ions. Therefore, they would only appear as an H^+ peak and not contribute to the He^{2+} peak.

It was found, however, that after running the experiment for a few hours, an H^+ peak appeared in the He spectrum which grew in time. Cleaning the helium supply line by successively pumping it out and flushing it with helium about five times removed this peak. Therefore it seems likely that a contamination was caused by residual gas, possibly moisture, in the helium line. Moisture, however, distorts neither the He^+ nor the He^{2+} peak as can be seen in Figure 10 (compare (b) and (d)). Since no permanent H^+ peak was observed, it is unlikely that the He bottle contained any of the above contaminants.

The statistical and systematic errors listed for the singles measurements also apply to the the coincidence measurements. The statistical errors are the error in fitting the fractional yield vs. pressure diagram (±5%) and the reproducibility error (±15%). The systematic errors, each of which is uniformly positive or negative for all of the measured data points, are the error due to the correction for the gas cell length (±2%), the erorr due to the uncertainty in the pressure measurement in the collision region (±5%), and the inaccuracy of the measurement in the main beam charge (±4%).

A significant source of error unique to the coincidence measurements is the uncertainty of the recoil-ion detector efficiency. This error is approximately 20% and applies only to the cross sections and not the ratios where this error cancels out.

In addition to the above uncertainties in the cross sections, corrections due to double collisions had to be made. In this experiment, the *final* target and projectile charge states were measured for each *initial* projectile charge states. There is, however, a possibility that the projectile does not change from its initial to its final charge state in a single step but that it undergoes an extra collision in the beamline or in the gas cell. In order to correct for these double collisions, the possible intermediate steps for the different reaction channels have to be considered. In the following paragraph, $\sigma_{i,f}$ and $\sigma_{i,f}^{*}$ denote the actual (true) and the measured cross sections, respectively, for a given initial (i) and final (f) charge state, and F_n is the zero pressure fractional yield for a given outgoing projectile charge state for a given beam energy. Hence, F_n depends on the residual gas background.

Incident Li^+ projectiles which emerge in the single capture channel can undergo capture in the beamline before the target region so that neutral Li^0 collides with the target, i.e.,

$$\sigma_{1,0}^{i\,*} = \sigma_{1,0}^{i} + F_0\sigma_{0,0}^{i}, \tag{44}$$

where i=01, 02 for single and double ionization of the target, respectively. Therefore, the measured coincidence cross section $\sigma_{1,0}^{i\,*}$ is the sum of the "true" coincidence cross section $\sigma_{0,1}^{i}$ and the product of the direct ionization cross section and the fraction of the ions which underwent premature capture. These correction terms were calculated for each energy and then averaged over the measured energy range. The corrections that have to be made for target single ionization, i.e, the difference between $\sigma_{1,0}^{i\,*}$ and $\sigma_{0,1}^{i}$ for

i=01, are found to be less than 1% for each energy investigated; for double ionization, i.e., i=02, the correction is even smaller.

In the single loss channel for Li^+, there are two reactions that can distort the results:

$$\sigma^{i}_{1,2}{}^{*} = \sigma^{i}_{1,2} + F_2\sigma^{i}_{2,2} + F_3\sigma^{i}_{3,2}, \tag{45}$$

with i=01,02. The second term on the right describes the single ionization of Li^+ before it strikes the helium target atom that is detected (Li^+ turns into Li^{2+} and then remains unchanged during a subsequent collision) and the third term is a sequence of a double loss and a subsequent single capture process (Li^+ turns into Li^{3+} and subsequently into Li^{2+}). The latter process is two to three orders of magnitude smaller than the second term and can therefore be neglected. Corrections corresponding to single and double target ionization based on Eq. 44 were found to be less than 5% and 3%, respectively, averaged over the measured energy range.

Li^{2+} capture corrections are described by

$$\sigma^{i}_{2,1}{}^{*} = \sigma^{i}_{2,1} + F_1\sigma^{i}_{1,1}, \tag{46}$$

with i=01, 02. Corrections for single and double ionization were found to be less than 1% for each energy. The single loss cross sections for Li^{2+}, described by

$$\sigma^{i}_{2,3}{}^{*} = \sigma^{i}_{2,3} + F_3\sigma^{i}_{3,3}, \tag{47}$$

with i=01, 02, have much bigger average corrections, namely, 25% for single and 7% for

double target ionization.

Li^{3+} capture corrections are described by

$$\sigma^{i}_{3,2}{}^{*} = \sigma^{i}_{3,2} + F_2\sigma^{i}_{2,2}, \tag{48}$$

with i=01,02. The corrections averaged over all energies were 5% for single ionization and 1% for double ionization.

There is an uncertainty associated with all of the above corrections because they vary with energy. For each projectile charge state and reaction channel, the standard deviation of the variations of the corrections over the measured energy range was assumed to be the uncertainty in making the corrections. For most cases, this uncertainty was negligible (<1%). However, the standard deviation, and therefore the uncertainty for the correction, for the single loss channel of Li^{2+} was 15% for single ionization and 4% for double ionization.

Double-To-Single Ionization Ratios

The statistical uncertainty for the ratios can be determined from the reproducibility of the results. When the ratios were calculated, they were determined for a given energy, charge state, and ionization channel from (a) the total number of counts for all pressures and from (b) the number of counts at each pressure. The latter method gives an estimate of the reproducibility of the ratio which was around 5%. In some cases, however, the error was larger (up to about 15%), especially when the total counts were low (around 100).

A systematic error in the measurement of these ratios can also result from the discriminator setting in the electronics setup. The constant-fraction discriminator (CFD) that selects the true recoil-ion signals from the noise required very careful setting in order not to cut out valid signals while still rejecting the noise (Figure 6). Figure 11 shows a plot of the measured double-to-single ionization ratios for 8 MeV Li^{3+} vs. the discriminator setting associated with no projectile charge change. The ratio that is expected from the scaling rule of Knudsen et al. (1984) is ≈1.6%. In the region around the discriminator setting of 0.18, which was used in the measurements the ratio varies due to inaccuracies in the setting of the discriminator or instabilities in the discriminator level or the input voltage. In fact, it was observed that the ratios obtained for bare Li^{3+} projectiles were as much as 10% higher than predicted by the scaling rule of Knudsen et al. (1984); this is a result which is consistent with data for bare He^{2+} taken by Forest et al. (1995). Therefore, an overall systematic error of +10% was assigned to the ratios measured here.

Like the coincidence cross sections, the ratios also have to be corrected for double collisions in the gas cell. This was done by recalculating all the ratios from the corrected cross sections obtained for each projectile energy, charge state, and reaction channel. In addition to the other errors that the ratios retain, this method introduces a new error due to the uncertainties in the corrections. The corrections that have to be made for each incident projectile and reaction channel vary with energy. As an estimate, the standard deviation of the corrections for the ratios for each projectile charge state and reaction channel over the entire energy range was taken to be the average error for that projectile

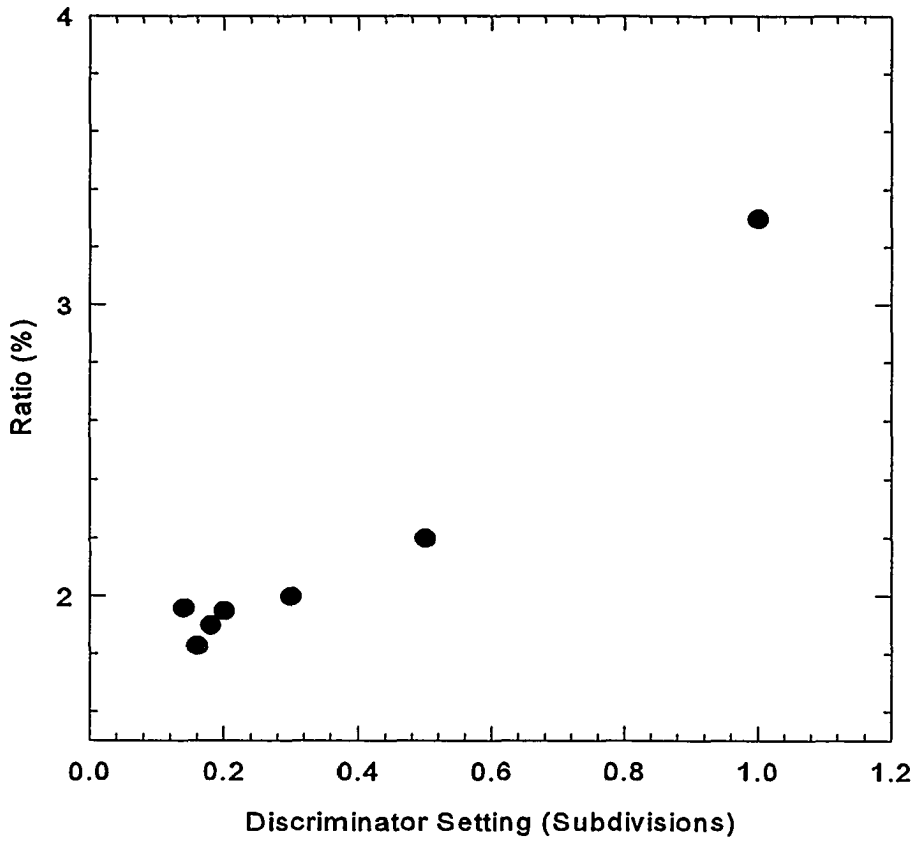

Figure 11. Double-to-Single Ionization Ratios vs. Discriminator Setting for No Charge Change for Incident 8 MeV Li^{3+} on He.

charge and reaction channel, in addition to the error that existed before the correction. For incident Li^{+}, the capture channel did not need to be corrected, while the single loss channel required an average correction of 5% over the investigated energy range with an uncertainty of 2%. For Li^{2+}, the capture channel again did not need correction, while the average single loss corrections were 23% with an uncertainty of 15%. The corrections for the single capture channel for Li^{3+} were about 5% with an uncertainty of about 2%.

RESULTS AND DISCUSSION

Singles Cross Sections

The cross sections for total single-electron loss from the projectile (projectile ionization) are listed in Table 1 and shown in Figure 12. For a discussion of the cross section values and their uncertainties refer to the previous chapter. The present data for Li^{2+} agree well with previous measurements by Hülskötter et al. (1991).

For Li^+ projectiles it is important to note that there can be metastable ions, i.e., Li^+ (1s2s), in the beam. These metastable ions can be created in the gas stripper at the high voltage terminal of the Van de Graaff which strips the Li^- extracted from the SNICS of two of its electrons. The flight path from the gas stripper (in the terminal) to the collision chamber is approximately 20 m so the Li^+, travelling with at most 8 MeV ($\approx 15*10^6$ m/s), spends about 1.3 μs in flight before a collision takes place. As Hvelplund (1976) notes, there are two possible metastable states in the beam, 1s2s $^1S_0$ and 1s2s $^3S_1$. The lifetimes of these states have been calculated by Drake et al. (1969, 1971) to be 0.5 ms and 49 s for the singlet and the triplet states, respectively. Therefore, the Li^+ beam reacting in the collision region is likely to be a mixture of the two metastable states 1s2s $^1S_0$ and 1s2s $^3S_1$, as well as the ground state $1s^2\ ^1S_0$.

Hvelplund (1976) measured capture and loss cross sections for ground state and metastable Li^+ produced with an atmospheric air stripper incident on He and Ar targets

Table 1

Cross Sections for Total Single Electron Loss From $Li^{1,2+}$ Projectiles in Collisions With Helium

E(MeV/u)	$\sigma_{q,q+1}$ (cm^2)	E(MeV/u)	$\sigma_{q,q+1}$ (cm^2)
Li^+ Projectile		Li^{2+} Projectile	
0.0714	(1.6 ± 0.3) [-17]	0.4286	(6.2 ± 1.2) [-18]
0.1071	(2.4 ± 0.5) [-17]	0.6429	(5.1 ± 1.0) [-18]
0.1429	(2.4 ± 0.5) [-17]	0.8571	(4.2 ± 0.8) [-18]
0.2143	(2.6 ± 0.5) [-17]	1.1429	(3.5 ± 0.7) [-18]
0.2857	(2.3 ± 0.5) [-17]	2.0000	(2.9 ± 0.6) [-18]
0.5714	(1.8 ± 0.4) [-17]	2.2857	(1.8 ± 0.4) [-18]
0.8571	(1.2 ± 0.3) [-17]		
1.0000	(1.2 ± 0.2) [-17]		
1.1429	(1.0 ± 0.2) [-17]		

and found that the metastable fraction was about 50% and that the cross sections resulting from collisions with metastable states are about 50 times higher than for collisions with ground state lithium. Although the impact energy was 40 - 90 keV (in the present experiment it is between 2 - 8 MeV), this shows that the existence of metastables can pose a serious problem.

In order to obtain an estimate of the metastable fraction in the present experiment, the Bohr formula for electron loss from the projectile (Eq. 3), can be used. Figure 12

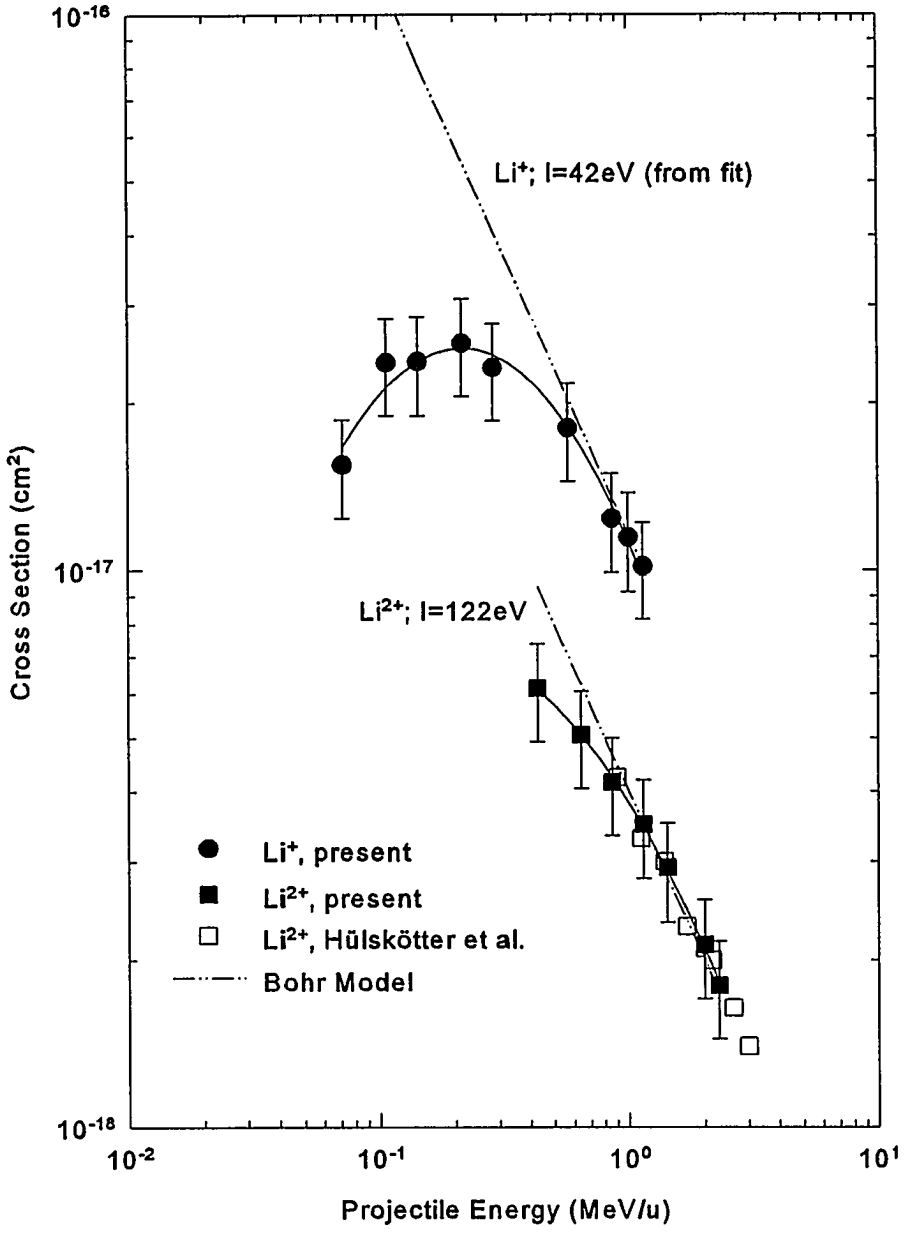

Note: Also shown are data from Hülskötter et al. (1991), and the theoretical Bohr model (Hvelplund et al., 1980 and Knudsen et al., 1982). In this model the ionization potential I for Li^{2+} is 122 eV, while for Li^{+} the theory fits the experiment for I=42 eV, which is between the value for ground state Li^{+} ($1s^2$) (76 eV) and the value for metastable Li^{+} (1s2s) (16 eV).

Figure 12. Cross Sections for Total Single-Electron Loss From the Projectile in $Li^{1,2+}$ + He Collisions.

shows the present experimental results in comparison with Bohr's prediction for electron loss for Li^{2+} and Li^{+} projectiles. The ionization energy, which is needed in the Bohr formula, for ground state Li^{+} is 76 eV, while for the metastable singlet and triplet states it is approximately 16 eV (Hvelplund, 1976). Experimentally, the Bohr model can be fit to the data for an ionization potential of 42 eV. Assuming a mixture of metastable and ground state in the beam, this leads to the following relation:

$$\sigma_{exp} = x\,\sigma_{meta} + (1-x)\,\sigma_{g.s.}, \tag{48}$$

where σ_{exp}, σ_{meta}, and $\sigma_{g.s.}$ are the measured cross section and the cross sections for the metastable and the ground states of Li^{+}, respectively, while x is the fraction of metastables. The electron loss cross sections are inversely proportional to the ionization potential (see Eq. 3). Thus, from the derived ionization potential I_{exp} (from the fit to the experimental data), and from the known ionization potentials for the metastable and the ground states I_{meta} and $I_{g.s.}$, respectively, the metastable fraction can be calculated to be:

$$x \approx 22\% \tag{49}$$

for the percentage of all metastable states in the beam.

Cross sections for total single electron capture are listed in Table 2 and shown in Figure 13. Comparison is made with the classical-trajectory Monte Carlo calculation of Olson (1978) for Li^{3+} and with the empirical scaling of Schlachter et al. (1987). Measurements by Wirkner-Bott et al. (1981) for Li^{2+} and Li^{3+} are also shown. These

Table 2

Cross Sections for Total Single Electron Capture to $Li^{1,2,3+}$ Projectiles in Collisions With Helium

E(MeV/u)	$\sigma_{q,q-1}$ (cm^2)	E(MeV/u)	$\sigma_{q,q-1}$ (cm^2)
Li^+ Projectile		Li^{2+} Projectile	
0.0714	(2.0 ± 0.4) [-17]	0.4286	(2.3 ± 0.5) [-18]
0.1071	(1.0 ± 0.2) [-17]	0.6429	(5.3 ± 1.1) [-19]
0.1429	(5.6 ± 1.1) [-18]	0.8571	(1.7 ± 0.3) [-19]
0.2143	(2.2 ± 0.4) [-18]	1.1429	(5.2 ± 1.0) [-20]
0.2857	(1.0 ± 0.2) [18]	1.4286	(1.9 ± 0.4) [-20]
0.5714	(1.2 ± 0.2) [-19]	2.0000	(3.5 ± 0.7) [-21]
0.8571	(2.4 ± 0.5) [-20]	2.2857	(3.0 ± 0.6) [-21]
1.0000	(1.5 ± 0.3) [-20]		
1.1429	(8.0 ± 1.6) [-21]		
Li^{3+} Projectile			
0.4286	(6.7 ± 1.3) [-18]		
0.5714	(2.4 ± 0.5) [-18]		
0.8571	(4.9 ± 1.0) [-19]		
1.1429	(1.5 ± 0.3) [-19]		
1.4429	(5.2 ± 1.0) [-20]		
1.7143	(2.2 ± 0.4) [-20]		
2.2857	(5.5 ± 1.1) [-21]		
2.8571	(2.4 ± 0.5) [-21]		

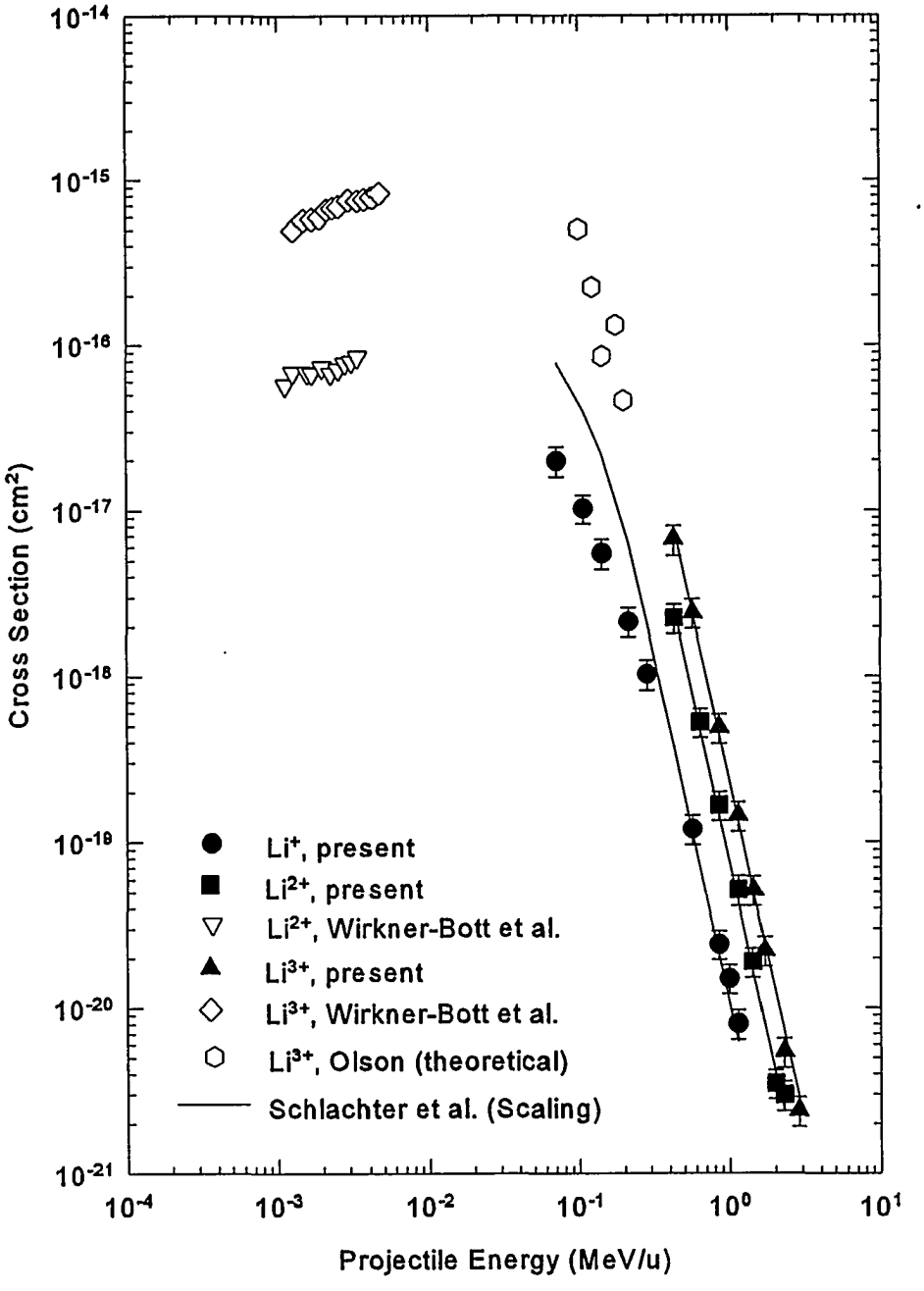

Note: Also shown are experimental data by Wirkner-Bott et al. (1981), the empirical scaling rule of Schlachter et al. (1987), and the classical trajectory Monte Carlo calculation by Olson (1978).

Figure 13. Cross Sections for Total Single-Electron Capture for Li^{q+} + He Collisions (q=1,2,3).

latter data, however, were taken in the keV energy range (compared to the MeV range in the present experiment) so that a direct comparison cannot be made.

Although the scaling rule of Schlachter et al. (1987) was derived mainly for single electron capture by fast highly-charged ions, Figure 13 shows that this scaling rule works well for Li^{+}, Li^{2+}, and Li^{3+} in the high-energy regime above about 0.5 MeV/u. In this regime, the scaling rule is given approximately by:

$$\sigma_{q-1} \propto q^{2.8} E^{-4.18}, \tag{50}$$

where E is in units of keV/u. It is noted that all of the single capture theories discussed in the chapter "Theoretical Background" have the same general form, i.e.,

$$\sigma_{q-1} = A q^{m} E^{n}. \tag{51}$$

Thus, this general form can be fit to the present data to determine more precisely the energy and charge scaling for Li^{q+} (q=1,2,3) projectiles.

Eq. 51 can be rewritten as:

$$\log \sigma_{q-1} = \log A + m \log q + n \log E. \tag{52}$$

Then n can be determined from the slope of a fit to the high-energy $Li^{1,2,3+}$ data in Figure 13, while log A + m log q is the intercept of the fit to the data. The intercept can then be plotted versus the charge state in order to determine the slope m and the intercept log A. The results of this fitting give m=2.74 (±0.06) and n=-4.2 (±0.3). The high-energy approximation for the present data is then:

$$\sigma_{q-1} \propto q^{2.74 \pm 0.06} E^{-4.2 \pm 0.3} \quad (53)$$

which is consistent with the result of Schlachter et al. (1987) within the experimental uncertainty.

Coincidence Measurements

Cross sections for the single and double ionization of He by $Li^{1,2,3+}$ projectiles undergoing no charge change, single electron capture, or single electron loss are listed in Tables 3 - 5 and shown in Figures 14 - 16, respectively. These coincidence cross sections were determined as discussed in the previous chapter.

For the direct ionization channel (Figure 14), the present results are consistent with earlier results of other investigators (Knudsen et al., 1984, Shah and Gilbody, 1985, and Sanders, 1995) except those for Li^+ associated with single target ionization measured by Knudsen et al. (1984). It is not clear why this is so but it could be due to a different fraction of metastable ions in the beam.

For the single capture channel (Figure 15), the present experiment provides new data in the energy regime above 700 keV/u for all three Li charge states. In the region of overlap with other measurements at lower energies, there is good agreement between the present experiment and the measurements by Shah and Gilbody (1985) and Sanders et al. (1995).

For the single loss channel (Figure 16), a comparison is made with the data of Sanders et al. (1995). In the region of overlap, the data for double target ionization agree

Table 3

Cross Sections for Single and Double Ionization of He by $Li^{1,2,3+}$ Projectiles Undergoing no Projectile Charge Change

E(MeV/u)	$\sigma^{01}_{q,q}$ (cm^2)	$\sigma^{02}_{q,q}$ (cm^2)	$R_{q,q}$ (%)
	Li^+ Projectile		
0.2857	(9.8 ± 2.7) -[17]	(4.8 ± 1.4) [-18]	4.9 ± 0.1
0.3571	(8.4 ± 2.3) -[17]	(3.6 ± 1.0) [-18]	4.3 ± 0.1
0.4286	(7.1 ± 2.0) -[17]	(2.7 ± 0.8) [-18]	3.8 ± 0.1
0.6429	(5.2 ± 1.5) -[17]	(1.4 ± 0.4) [-18]	2.7 ± 0.1
0.8571	(4.0 ± 1.1) -[17]	(8.8 ± 2.5) [-19]	2.2 ± 0.3
1.1429	(3.7 ± 1.0) -[17]	(6.0 ± 1.7) [-19]	1.6 ± 0.1
	Li^{2+} Projectile		
0.4286	(1.9 ± 0.5) [-16]	(6.7 ± 1.9) [-18]	3.5 ± 0.3
0.6429	(1.2 ± 0.3) [-16]	(3.0 ± 0.8) [-18]	2.4 ± 0.1
0.8571	(9.1 ± 2.6) [-17]	(1.8 ± 0.5) [-18]	1.9 ± 0.1
1.1429	(8.2 ± 2.3) [-17]	(1.3 ± 0.4) [-18]	1.5 ± 0.1
1.4286	(5.8 ± 1.6) [-17]	(6.8 ± 1.9) [-19]	1.2 ± 0.1
1.7143	(5.9 ± 1.7) [-17]	(5.2 ± 1.5) [-19]	0.9 ± 0.1
2.2857	(4.5 ± 1.3) [-17]	(3.8 ± 1.1) [-19]	0.8 ± 0.2

Table 3--Continued

E(MeV/u)	$\sigma^{01}_{q,q}$ (cm^2)	$\sigma^{02}_{q,q}$ (cm^2)	$R_{q,q}$ (%)
	Li^{3+} Projectile		
0.4286	(3.3 ± 0.1) [-16]	(1.5 ± 0.4) [-17]	4.5 ± 0.1
0.5714	(2.4 ± 0.7) [-16]	(8.4 ± 2.4) [-18]	3.5 ± 0.2
0.8571	(1.7 ± 0.5) [-16]	(3.9 ± 1.1) [-18]	2.4 ± 0.0
1.7143	(1.2 ± 0.3) [-16]	(1.4 ± 0.4) [-18]	1.2 ± 0.0
2.2857	(8.4 ± 2.3) [-17]	(8.4 ± 2.3) [-19]	1.0 ± 0.1
2.8571	(7.5 ± 2.1) [-17]	(5.8 ± 1.6) [-19]	0.8 ± 0.1
3.4286	(6.4 ± 1.8) [-17]	(4.8 ± 1.3) [-19]	0.7 ± 0.0

Note: The ratios $R_{q,q}$ of double-to-single ionization are also shown. Only the random uncertainties are given here.

very well, while the present results for single target ionization appear to be lower than those of Sanders et al. (1995).

From Figures 14 - 16 it is seen that for all incident projectile charges and outgoing projectiles charge states, the cross sections for double target ionization are seen to be smaller than the cross sections for single target ionization. This result is consistent with the expectation that double target ionization requires a "harder" collision, i.e., the average impact parameter for the collision is smaller.

In this work, the main interest is the ratio of double-to-single ionization of the He

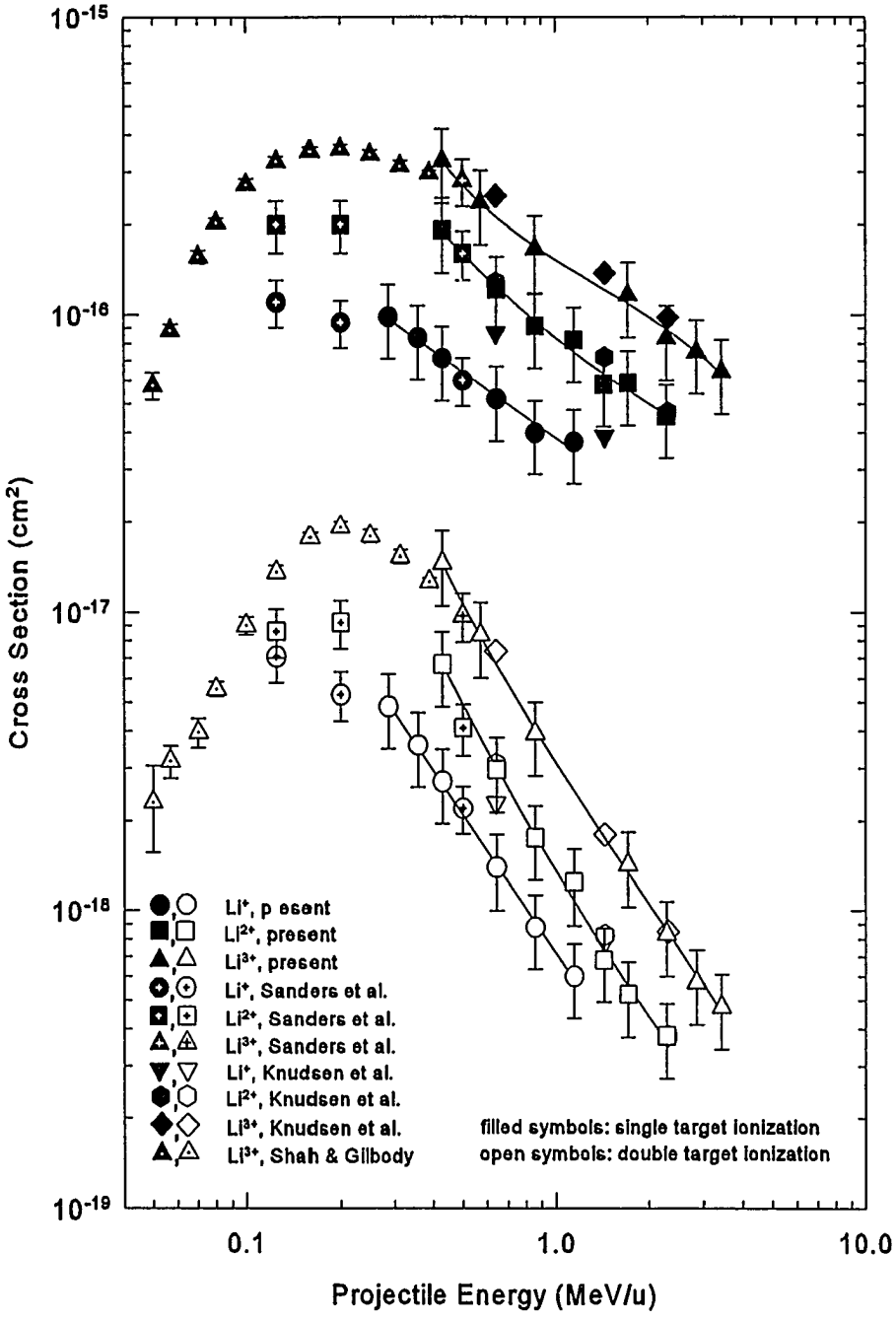

Note: Results of Sanders et al. (1995), Knudsen el al. (1984), and Shah and Gilbody (1985) are also shown. The lines are drawn to guide the eye.

Figure 14. Cross Sections for the Single and Double Ionization of He by $Li^{1,2,3+}$ Projectiles Undergoing No Charge Change.

Table 4

Cross Sections for the Single and Double Ionization of He by $Li^{1,2,3+}$ Projectiles Undergoing Single Electron Capture

E(MeV/u)	$\sigma^{01}_{q,q-1}$ (cm^2)	$\sigma^{02}_{q,q-1}$ (cm^2)	$R_{q,q-1}$ (%)
	Li^+ Projectile		
0.2857	(6.9 ± 1.9) [-19]	(2.1 ± 0.6) [-19]	29.5 ± 0.3
0.3571	(4.1 ± 1.2) [-19]	(1.2 ± 0.3) [-19]	27.9 ± 0.5
0.4286	(2.1 ± 0.6) [-19]	(5.4 ± 1.5) [-20]	25.1 ± 0.9
0.6429	(5.6 ± 1.6) [-20]	(1.1 ± 0.3) [-20]	18.9 ± 1.5
0.8571	(1.9 ± 0.5) [-20]	(3.2 ± 0.9) [-21]	16.9 ± 0.8
1.1429	(6.9 ± 1.9) [-21]	(1.1 ± 0.3) [-21]	16.6 ± 2.8
	Li^{2+} Projectile		
0.4286	(1.8 ± 0.5) [-18]	(4.8 ± 1.3) [-19]	26.9 ± 1.0
0.6429	(4.3 ± 1.2) [-19]	(9.4 ± 2.6) [-20]	21.5 ± 0.5
0.8571	(1.4 ± 0.4) [-19]	(2.7 ± 0.7) [-20]	18.8 ± 1.6
1.1429	(4.5 ± 1.3) [-20]	(6.8 ± 1.9) [-21]	15.1 ± 0.6
1.4286	(1.5 ± 0.4) [-20]	(2.3 ± 0.6) [-21]	14.9 ± 1.5
1.7143	(7.1 ± 2.0) [-21]	(1.1 ± 0.3) [-21]	14.9± 0.1
	Li^{3+} Projectile		
0.4286	(5.8 ± 1.6) [-18]	(2.2 ± 0.6) [-18]	37.8 ± 1.7
0.5714	(1.8 ± 0.5) [-18]	(5.9 ± 1.7) [-19]	32.0 ± 1.9
0.8571	(3.9 ± 1.1) [-19]	(9.9 ± 2.8) [-20]	25.5 ± 0.9
1.1429	(1.2 ± 0.3) [-19]	(2.2 ± 0.6) [-20]	17.7 ± 0.1

Table 4--Continued

E(MeV/u)	$\sigma^{01}_{q,q-1}$ (cm^2)	$\sigma^{02}_{q,q-1}$ (cm^2)	$R_{q,q-1}$ (%)
1.7143	(2.0 ± 0.6) [-20]	(2.3 ± 0.7) [-21]	11.8 ± 1.2
2.0000	(2.0 ± 0.6) [-20]	(1.6 ± 0.5) [-21]	8.1 ± 0.7

Note: The ratios $R_{q,q-1}$ of double-to-single ionization are also shown. Only the random uncertainties are given here.

target which gives insight into the nature of the double ionization process. As discussed in the chapter "Theoretical Background", by considering this ratio single ionization effects tend to cancel out. The double-to-single target ionization ratios associated with projectiles undergoing no charge change (direct ionization), single-electron capture, and single-electron loss are listed in Tables 3 - 5.

The double-to-single ionization ratios R can be examined (a) as a function of the incoming projectile charge state, or (b) as a function of the outgoing projectile charge state, i.e., reaction channel. In Figures 17 - 19 the double-to-single ionization ratios are shown for all outgoing projectile charge states associated with a given incoming projectile (no charge change, capture, or loss) associated with each incoming charge state.

A benchmark for the validity of the present results is the double-to-single ionization ratio associated with no projectile charge change for Li^{3+} projectiles. For bare charge state, while Figures 20 - 22 show the ratios for a given outgoing reaction channel

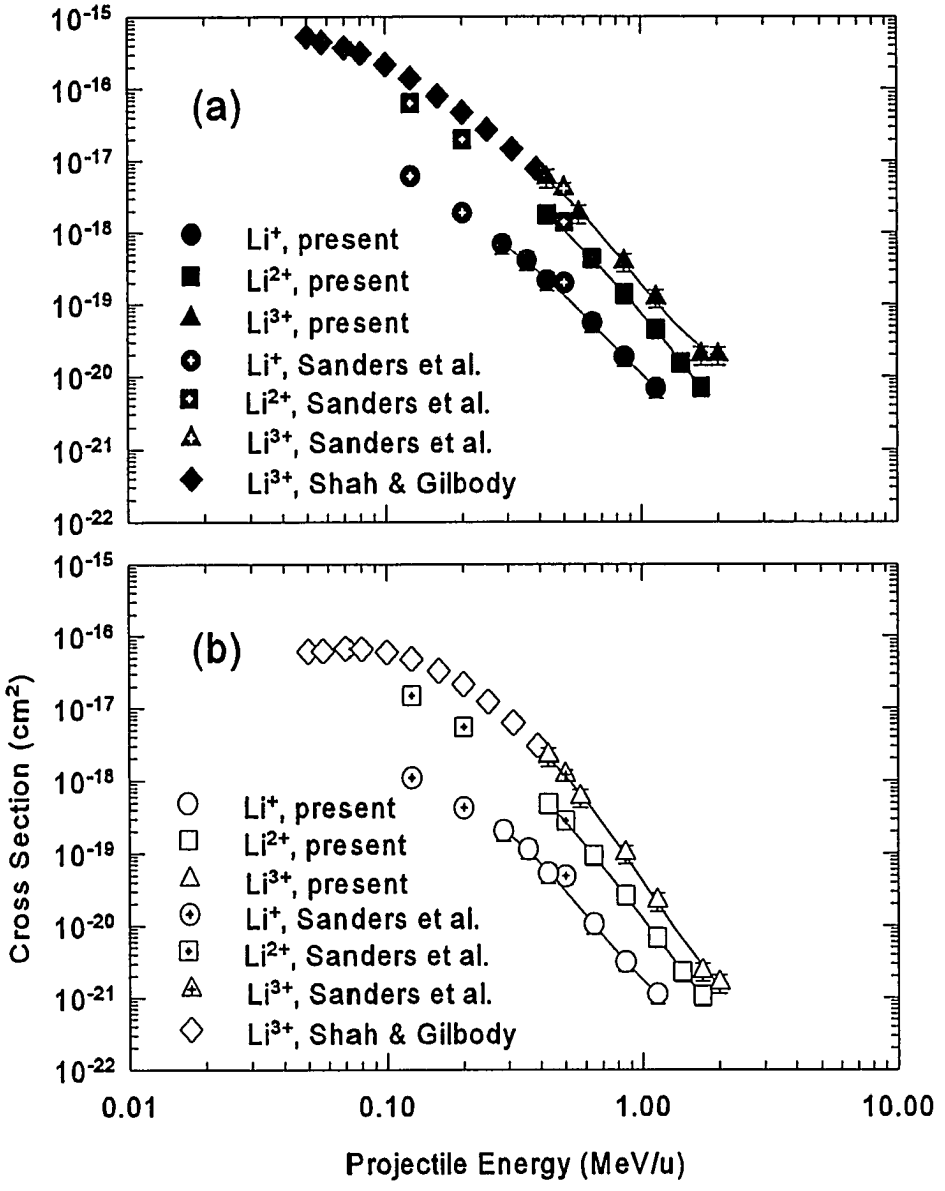

Note: Results of Sanders et al. (1995) and Shah and Gilbody (1985) are also shown. The lines are drawn to guide the eye.

Figure 15. Cross Sections for (a) Single and (b) Double Ionization of He by $Li^{1,2,3+}$ Projectiles Undergoing Single Electron Capture.

Table 5

Cross Sections for the Single and Double Ionization of He by $Li^{1,2+}$ Projectiles Undergoing Single Electron Loss

E (MeV/u)	$\sigma^{01}_{q,q+1}$ (cm^2)	$\sigma^{02}_{q,q+1}$ (cm^2)	$R_{q,q+1}$ (%)
	Li^+ Projectiles		
0.2857	(1.1 ± 0.3) [-17]	(1.3 ± 0.4) [-18]	11.2 ± 0.3
0.3571	(9.1 ± 2.6) [-18]	(9.2 ± 2.6) [-19]	10.1 ± 0.3
0.4286	(6.6 ± 1.9) [-18]	(6.1 ± 1.7) [-19]	9.3 ± 0.6
0.6429	(6.3 ± 1.8) [-18]	(4.0 ± 1.1) [-19]	6.5 ± 0.3
0.8571	(4.7 ± 1.3) [-18]	(2.5 ± 0.7) [-19]	5.3 ± 0.2
1.1429	(3.9 ± 1.1) [-18]	(1.6 ± 0.5) [-19]	4.1 ± 0.2
	Li^{2+} Projectiles		
0.4286	(2.4 ± 0.7) [-18]	(3.5 ± 1.0) [-19]	14.8 ± 2.4
0.6429	(2.1 ± 0.7) [-18]	(2.3 ± 0.7) [-19]	10.8 ± 1.8
0.8571	(1.9 ± 0.6) [-18]	(1.7 ± 0.5) [-19]	8.7 ± 1.5
1.1429	(1.4 ± 0.4) [-18]	(9.8 ± 2.8) [-20]	7.2 ± 1.2
1.4286	(1.0 ± 0.3) [-18]	(6.9 ± 1.9) [-20]	6.8 ± 1.3
1.7143	(9.6 ± 3.1) [-19]	(5.7 ± 1.6) [-20]	6.0 ± 1.3
2.2857	(8.7 ± 2.8) [-19]	(3.6 ± 1.0) [-20]	4.1 ± 0.8

Note: The ratios $R_{q,q+1}$ of double-to-single ionization are also shown. Only the random uncertainties are given here.

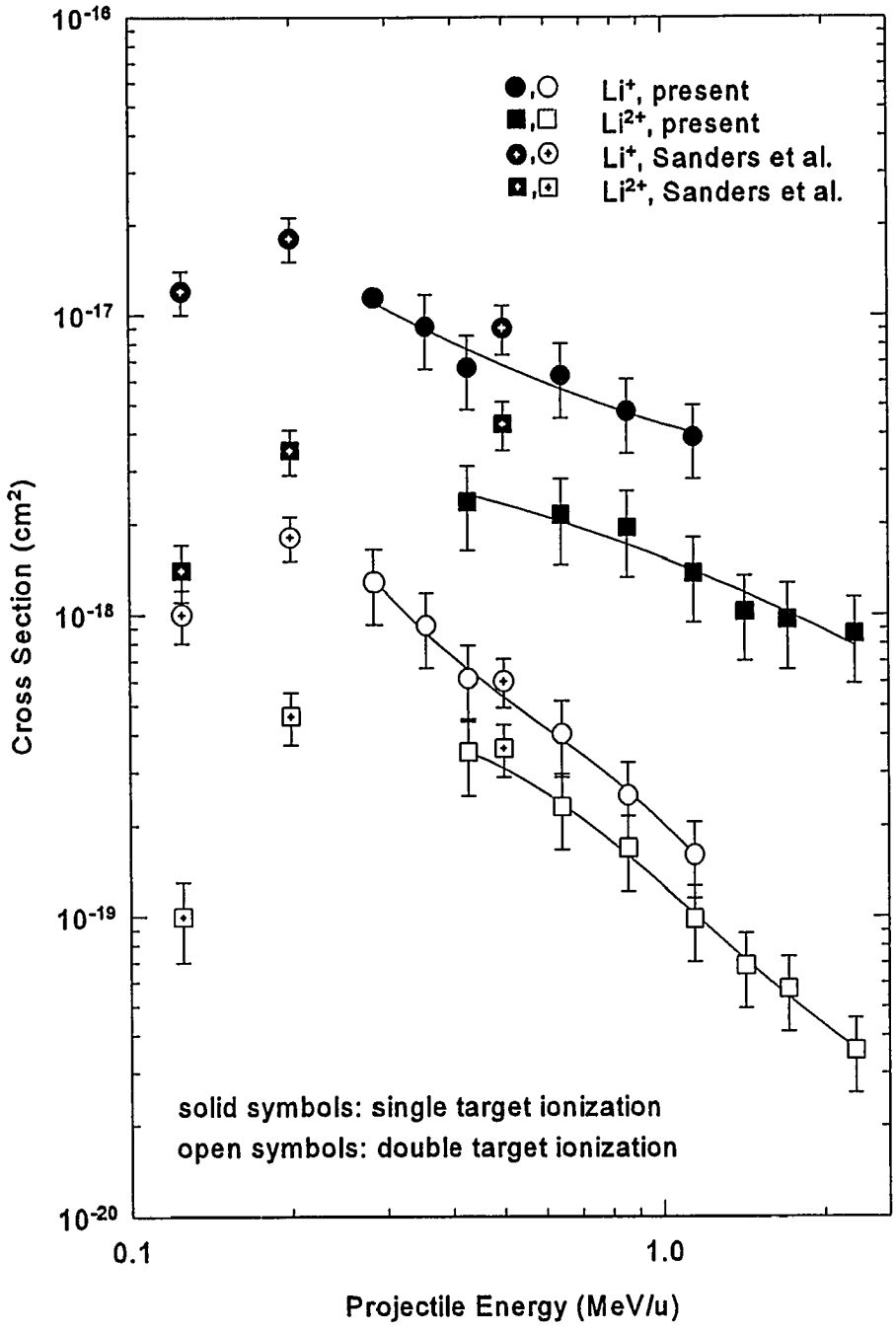

Note: Results of Sanders et al. (1995) are also shown. The lines are drawn to guide the eye.

Figure 16. Cross Sections for the Single and Double Ionization of He by $Li^{1,2+}$ Projectiles Undergoing Single Electron Loss.

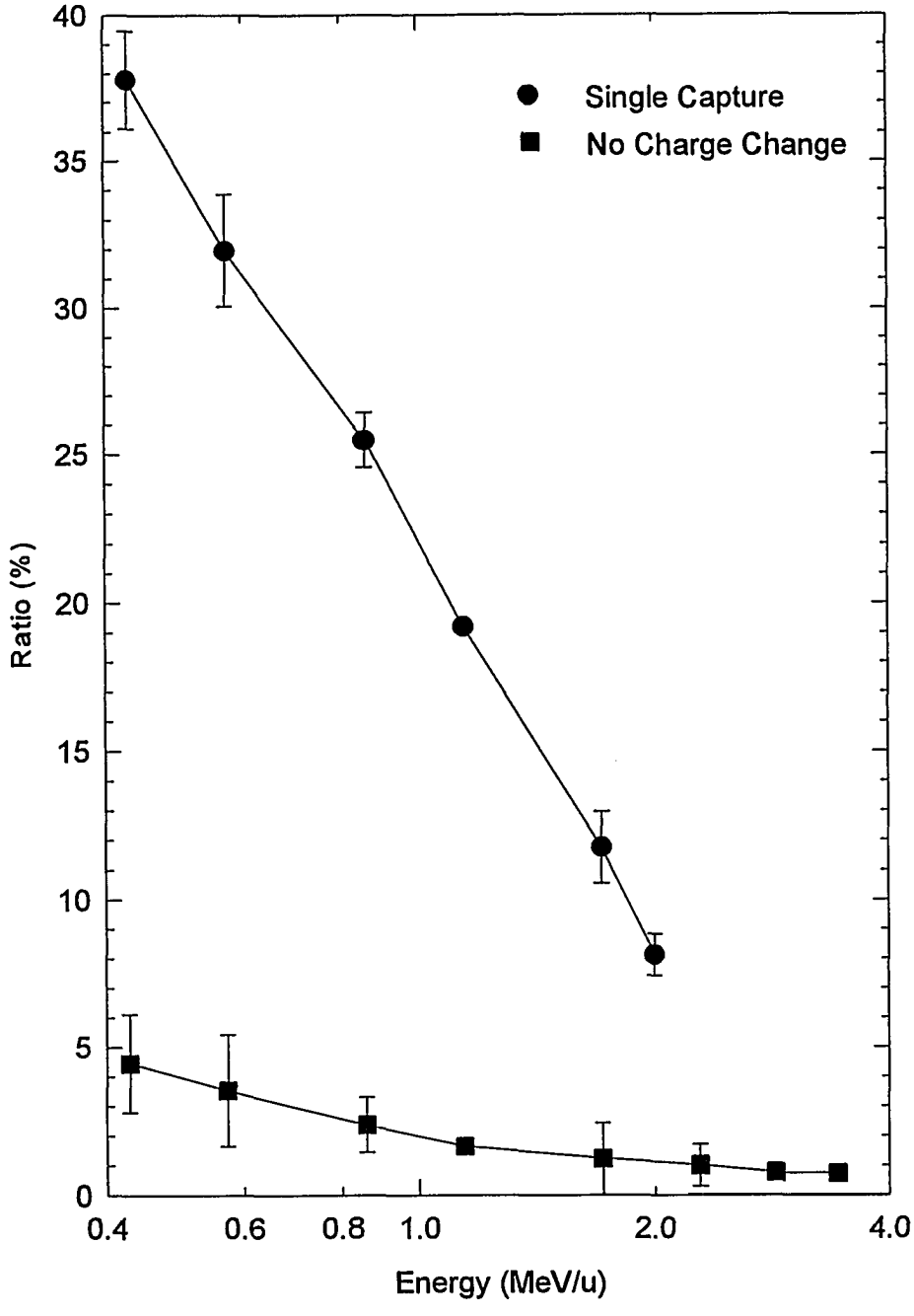

Note: The lines are drawn to guide the eye.

Figure 17. He Target Double-to-Single Ionization Ratios Associated With Direct Ionization (No Charge Change) and Single-Electron Capture for Li^{3+} Projectiles.

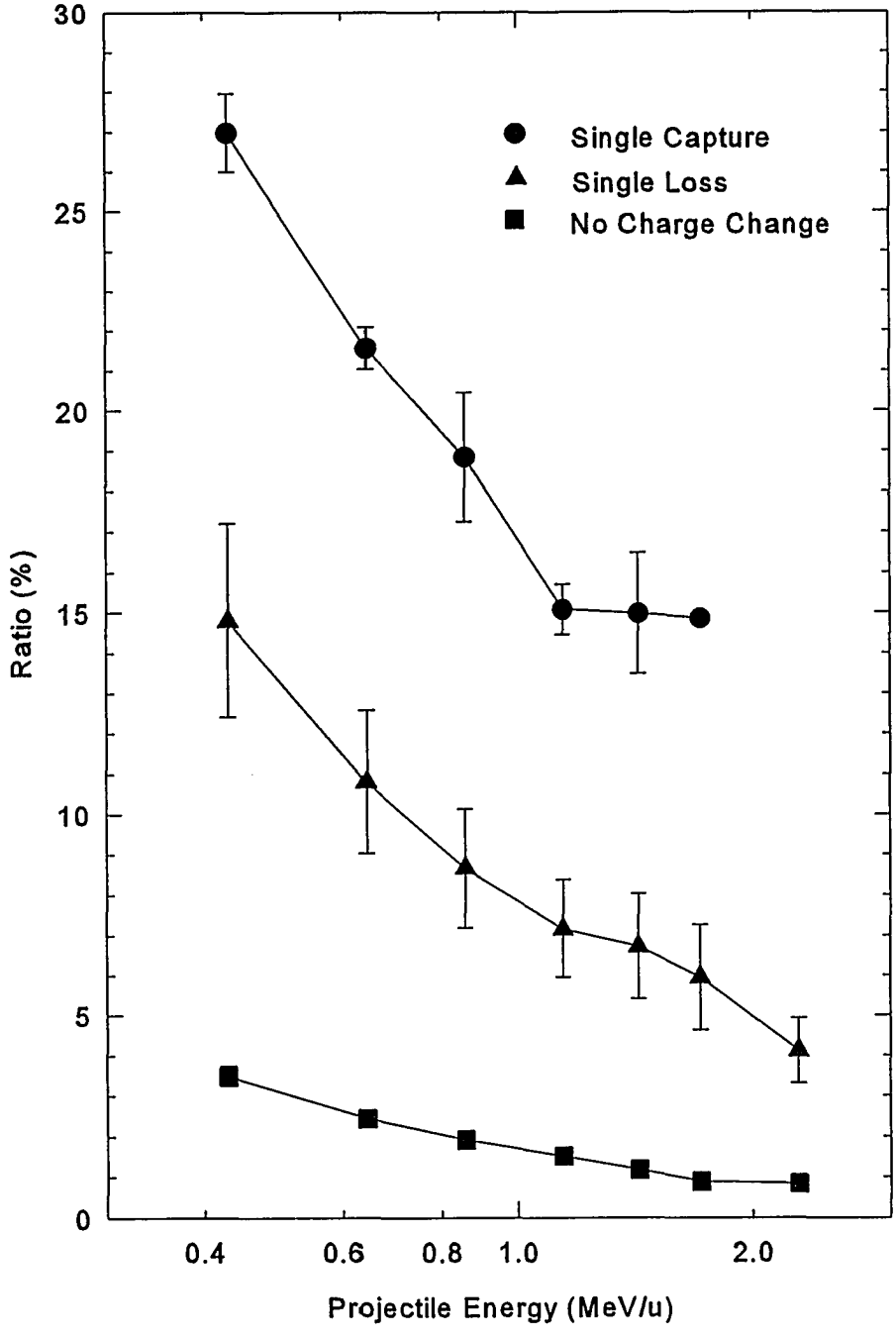

Note: The lines are drawn to guide the eye.

Figure 18. He Target Double-to-Single Ionization Ratios Associated With Direct Ionization (No Charge Change), Single-Electron Capture, and Single-Electron Loss for Li^{2+} Projectiles.

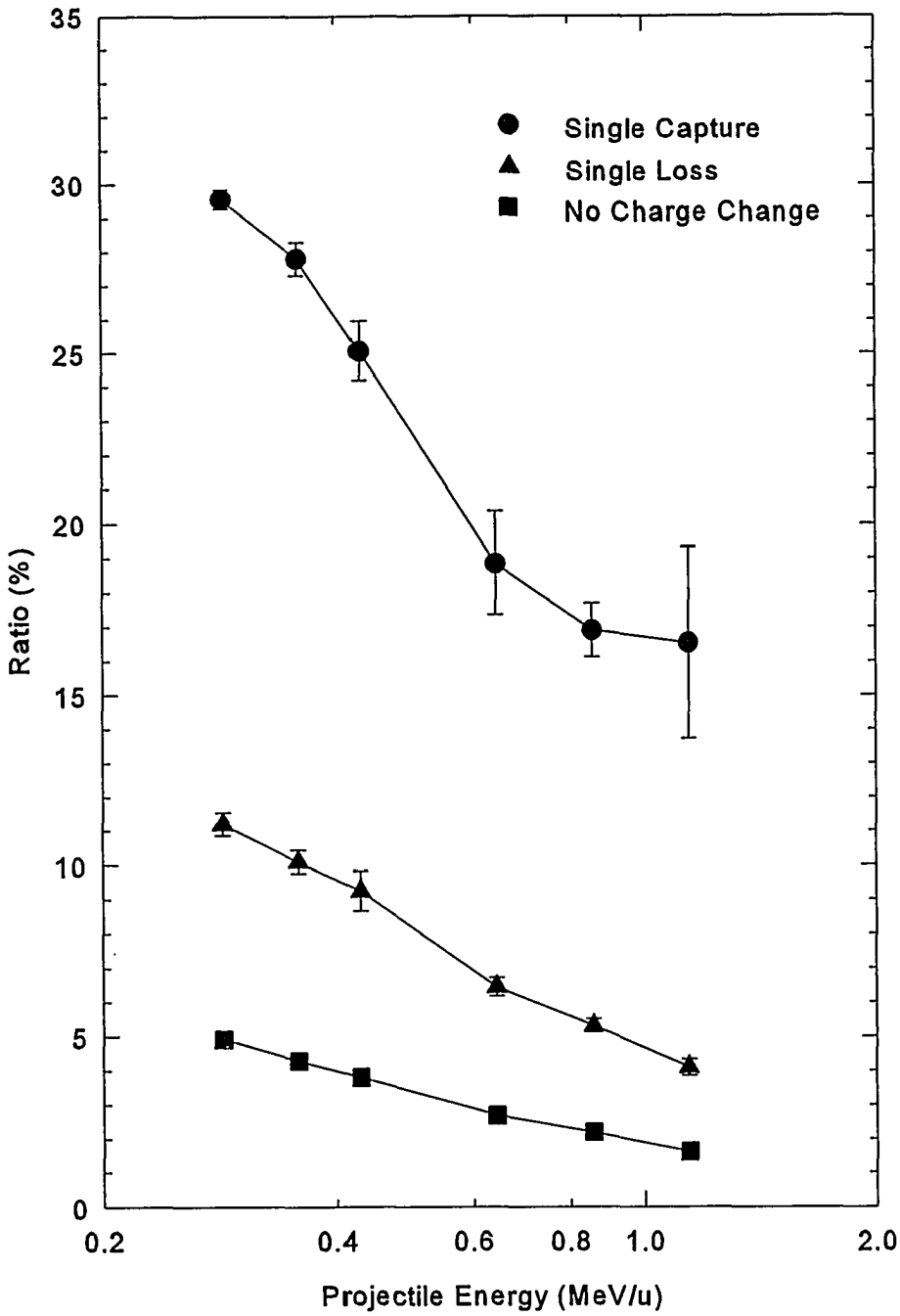

Note: The lines are drawn to guide the eye.

Figure 19. He Target Double-to-Single Ionization Ratios Associated With Direct Ionization (No Charge Change), Single-Electron Capture, and Single Electron Loss for Li^+ Projectiles.

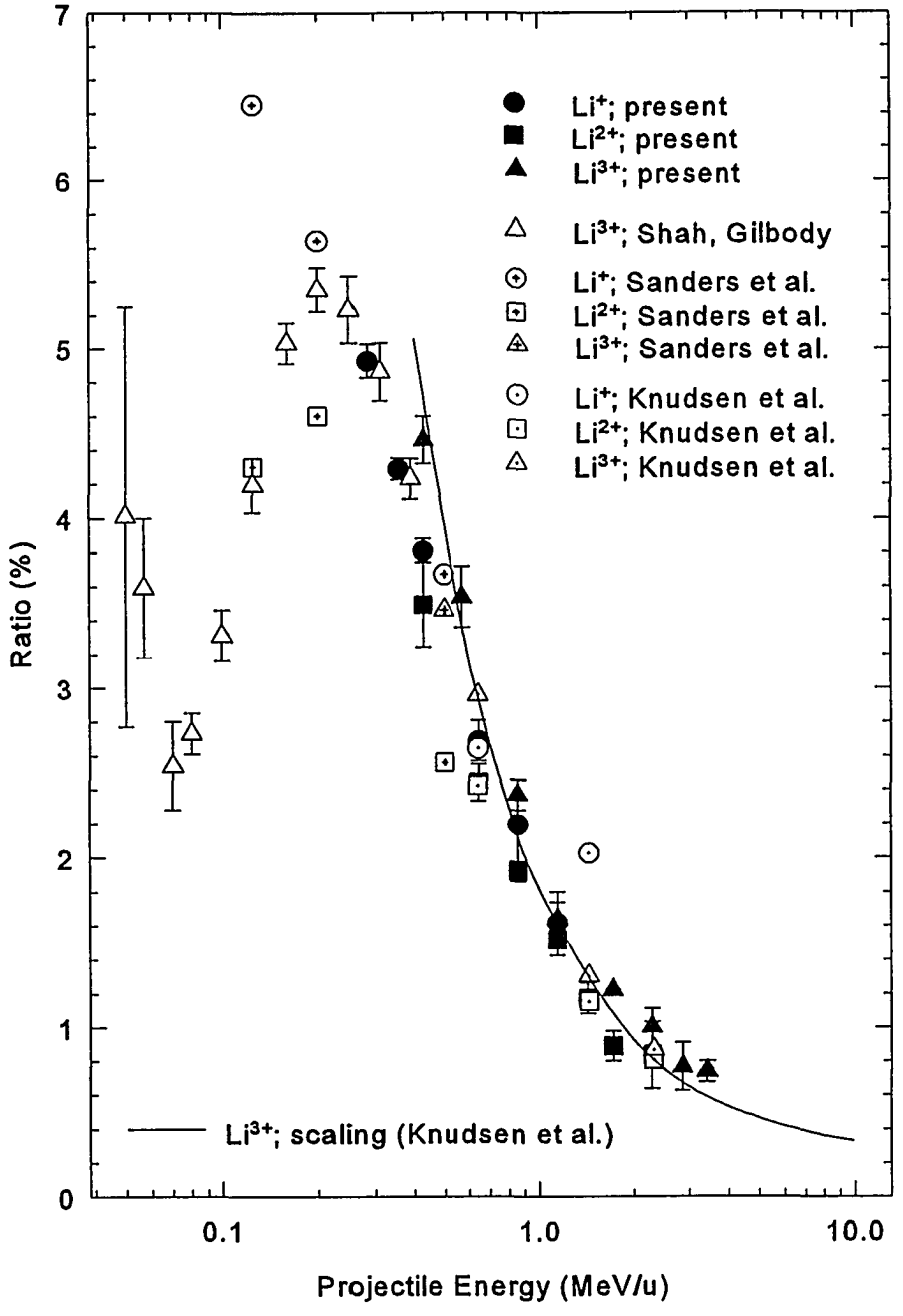

Note: Also shown are data from Knudsen et al. (1984), Shah and Gilbody (1985), and Sanders et al. (1995). The smooth curve is the scaling rule of Knudsen et al. (1984) for Li^{3+} + He.

Figure 20. He Target Double-to-Single Ionization Ratios Associated With No Charge Change for Li^{+}, Li^{2+}, and Li^{3+} Projectiles.

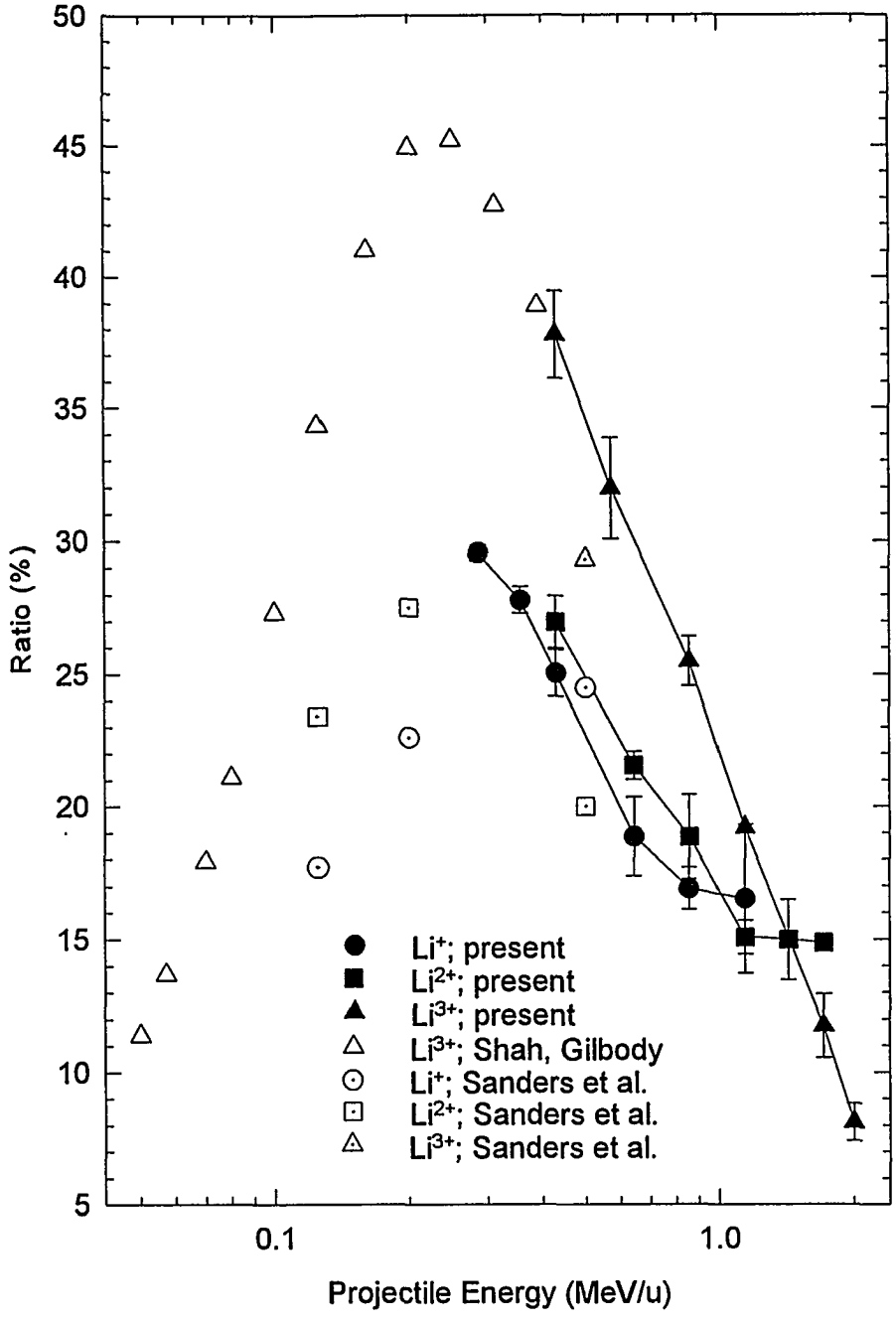

Note: Also shown are data from Shah and Gilbody (1985) and Sanders et al. (1995). The lines are drawn to guide the eye.

Figure 21. He Target Double-to-Single Ionization Ratios Associated With Single-Electron Capture for Li^{+}, Li^{2+}, Li^{3+} Projectiles.

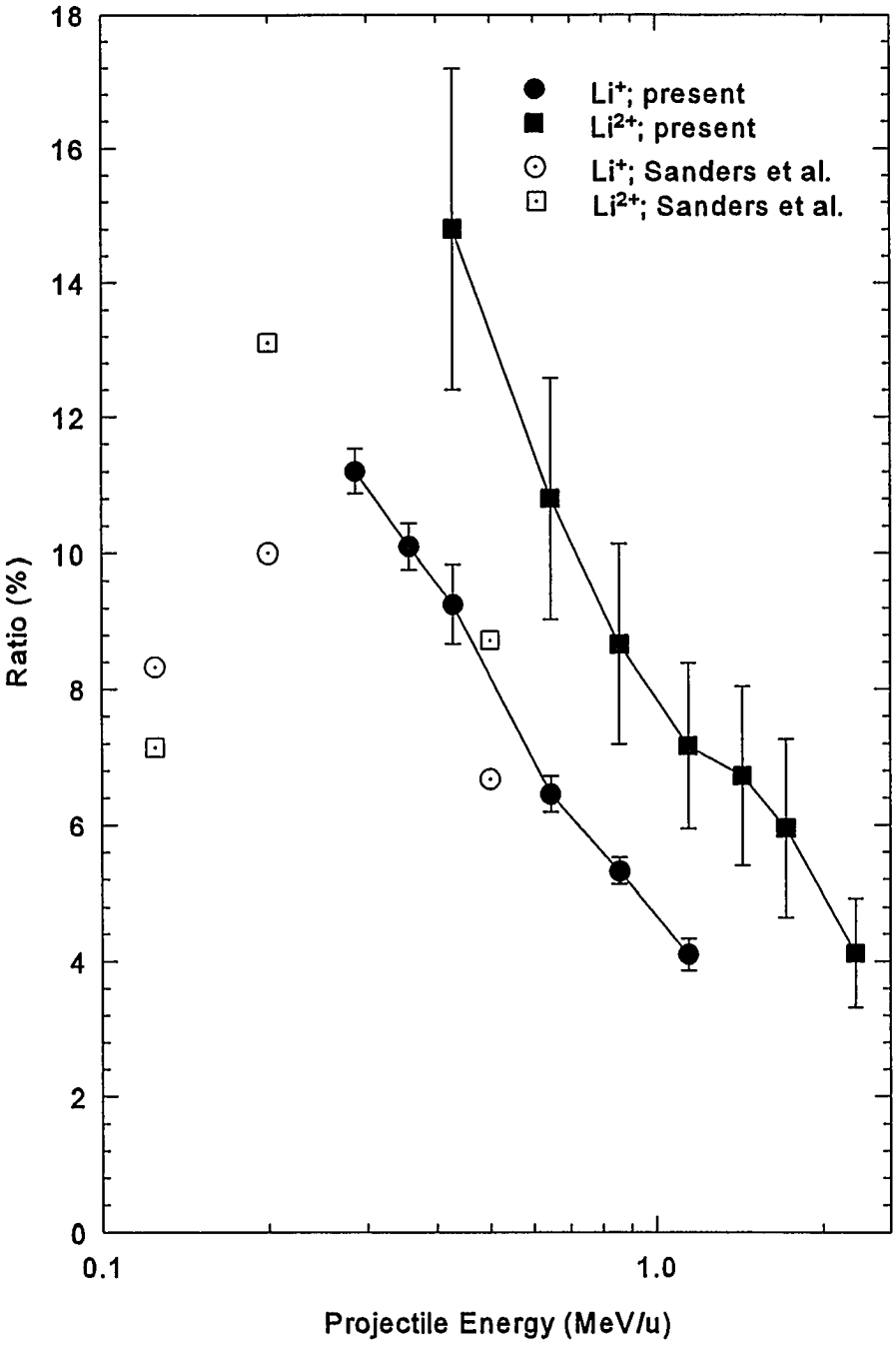

Note: Also shown are data from Sanders et al. (1995). The lines are drawn to guide the eye.

Figure 22. He Target Double-to-Single Ionization Ratios Associated With Single-Electron Loss for Li^{+} and Li^{2+} Projectiles.

projectiles with charge Z and energy E Knudsen et al. (1984) found a semi-empirical scaling rule,

$$R_{Z,Z} = 2.2\times10^{-3} + 4.55\times10^{-3}\frac{Z^2}{E\ \ln(13.12\sqrt{E})}, \qquad (54)$$

where E is in units of MeV/u. This scaling rule predicts that in the TS (two-step, see chapter "Theoretical Background") regime $R_{Z,Z}$ is mainly a function of Z/v, while in the SO (shake-off) limit $R_{Z,Z}$ is constant. The approximate regions of validity for the TS and SO mechanisms are shown in Figure 23 (Tanis, 1992) as a function of Z and v. Indeed the present results for the bare Li^{3+} projectiles obey this scaling rule as seen in Figure 24.

Figures 17 - 22 which show the double-to-single ionization ratios allow three important observations:

1. For a given incident projectile charge state, the ratios depend strongly on the reaction channel (Figures 17 - 19).

2. For direct ionization (no charge change), the ratios are largely independent of the incoming projectile charge state (Figure 20), and apparently depend only on the nuclear charge.

3. For single-electron capture and single-electron loss, the ratios depend quite strongly on the incoming projectile charge state (Figures 21 and 22).

Observation (1) can be specified as:

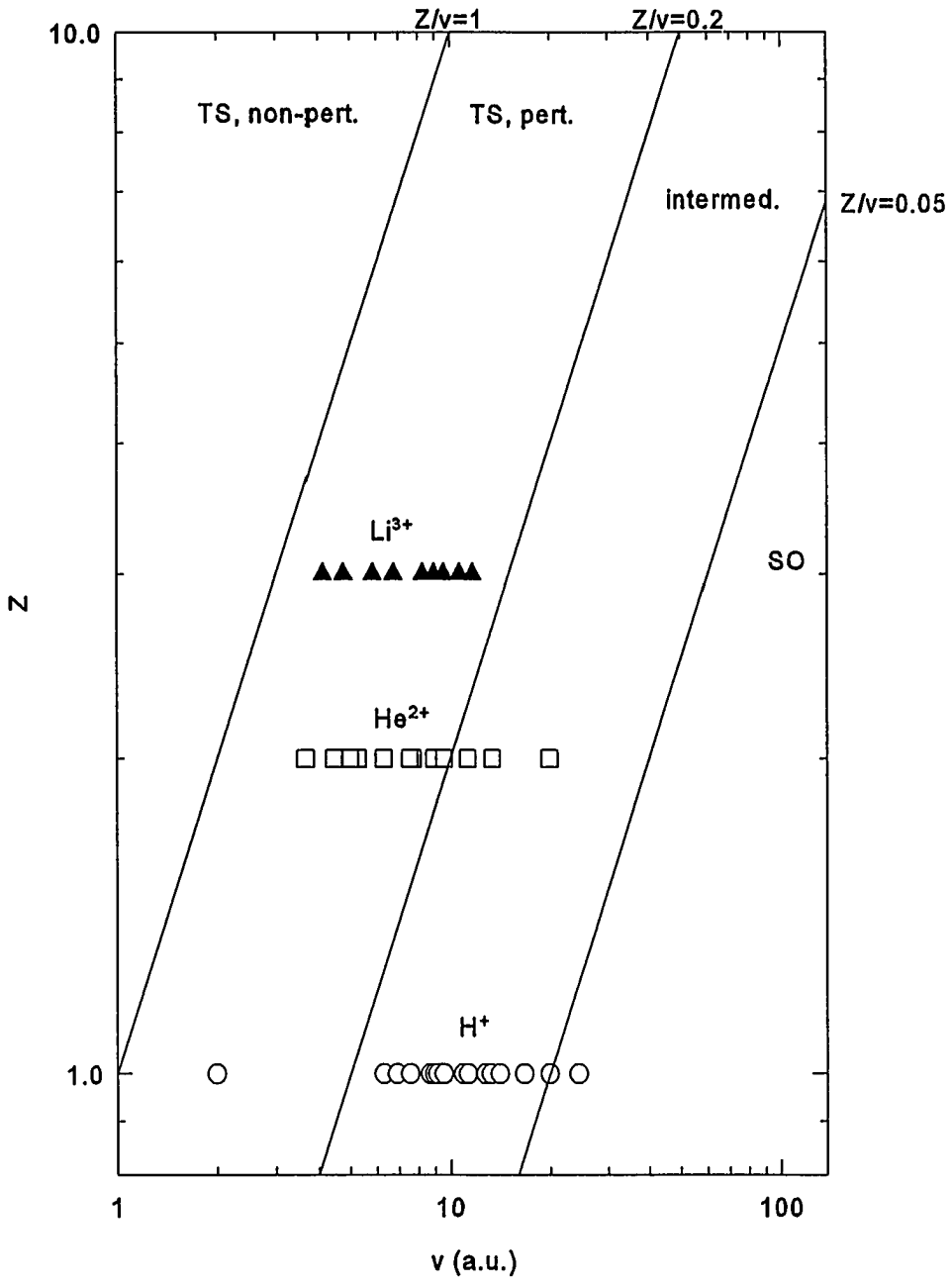

Note: The Li^{3+} points show where the data from the present experiment lie and the H^{+} and He^{2+} points show where the data of Knudsen et al. (1984) and Andersen et al. (1987) lie.

Figure 23. Plot of Z vs. v Showing the Regions Where the Non-Perturbative Two-Step (TS, non-pert.), the Perturbative Two-Step (TS, pert.), and the Shake-Off (SO) Mechanisms Are Important as Well as the Intermediate Region Where Both TS and SO May Be Important.

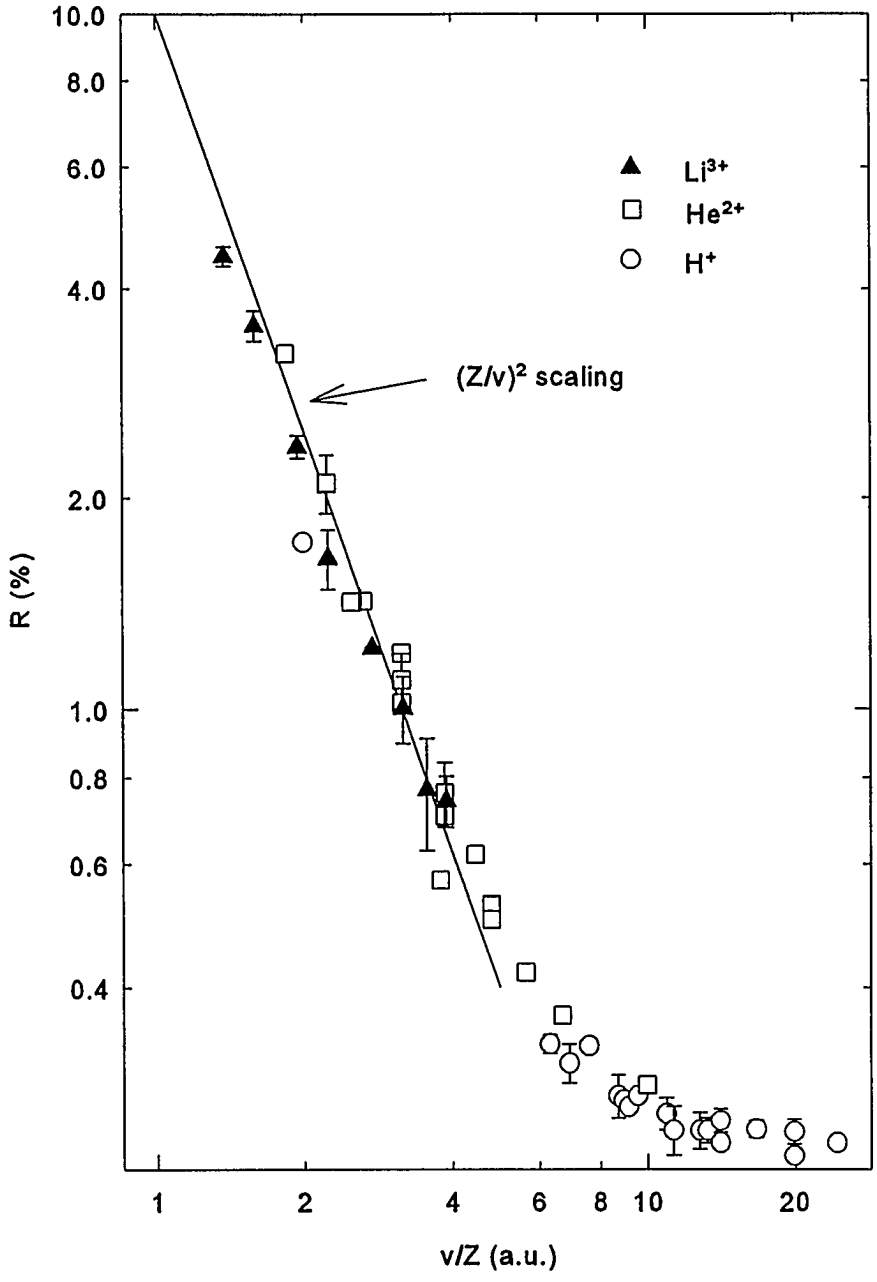

Note: The linear slope up to about v/Z=5 marks the TS regime, while the horizontal tail above about v/Z=20 marks the SO limit. The results for Li^{3+} are from the present experiment, while the data for H^+ and He^{2+} are from Knudsen et al. (1984) and from Andersen et al. (1987).

Figure 24. He Target Double-to-Single Ionization Ratios for No Projectile Charge Change vs. v/Z for Collisions of H^+, He^{2+}, and Li^{3+} With He.

$$R_{q,q} \leq R_{q,q+1} \leq R_{q,q-1}, \quad (55)$$

where the subscripts denote the reaction process (for Li^{3+} there is of course no single loss). This dependence of R on the outgoing charge state can be understood qualitatively in terms of the average impact parameters for the three types of collision reactions. The larger the ratio, the more double ionization which takes place and this is generally expected to require smaller impact parameter collisions than for single ionization. Therefore, the average impact parameter for the single capture reaction channel is expected to be smaller than that for the single loss channel, which, in turn, is smaller than the average impact parameter for direct ionization. The fact that the average impact parameters depend strongly on the ionization reaction channel indicates that the projectile electrons react with the target electrons in different ways. This is consistent with observation (3) and will be discussed below in the context of projectile electron - target electron interactions.

Scattering Without Projectile Electron - Target Electron Interaction (Direct Ionization)

According to observation (2), the ratio $R_{q,q}$ for direct ionization is nearly independent of the number of electrons on the impacting projectile. Figure 20 shows that for energies $\gtrsim$ 0.3 MeV/u the ratios for incident $Li^{1,2,3+}$ are all nearly the same, and fall along the predicted scaling rule of Knudsen et al. (1984) for Li^{3+}. This phenomenon was previously observed by Forest et al. (1995) who report that the double-to-single ionization ratios of He^{+} + He and of He^{2+} + He are nearly the same in this intermediate-

velocity regime. Since the scaling rule of Knudsen et al. (1984) was derived only for *bare* projectiles impacting on He, it is not clear a priori that it should work for partially-stripped projectiles. From Figure 20, however, it can be seen that for energies $\gtrsim$ 0.3 MeV/u the incident projectile charge state does not appear to play an important role in the double-to-single ionization ratio. These results suggest that the electrons on the projectile have almost no influence on the double-to-single ionization ratio, and therefore, the projectile *electron* - target electron interaction appears to be negligible compared to the projectile *nucleus* - target electron interaction for the direct ionization channel. Thus, for the direct ionization channel it is concluded that the ratio of double-to-single ionization of the He target is governed almost exclusively by the nuclear charge.

Scattering With Projectile Electron - Target Electron Interaction
(Single Electron Capture and Single Electron Loss)

In the single loss channel (Figure 22), the ratios for Li^+ and Li^{2+} exhibit a similar behavior, with the Li^{2+} ratios being approximately 80% larger than the Li^+ results. Thus, Li^{2+} causes more target double ionization for a given amount of target single ionization than Li^+. This is evidence that the electronic structure in this reaction channel plays an important role. The results can be interpreted in the free-collision model (Hvelplund et al., 1980 and Knudsen et al., 1982). In this model,collision processes such as Li^{2+} + He and He^+ + He reduce to collisions of He targets with bare projectiles, namely, Li^{3+} + He and He^{2+} + He, respectively, where the projectiles do not change their charge state, plus the scattering of a free electron accompanying these processes, i.e., e^- + He. Electrons

in the collision reaction have a dual role: they can (a) shield the nucleus (screening), or (b) ionize the electron(s) of the collision partner (antiscreening). In the screening process, the electrons remain in their original state, while in the antiscreening process they actively participate in the collision and can be ionized or excited (McGuire et al., 1981, Montenegro and Meyerhof, 1991, Montenegro et al., 1992, and Montenegro et al., 1994). Screening is characterized by an electron - nucleus interaction, while antiscreening involves the electron - electron interaction. Screening and the excitation part of antiscreening both leave the projectile in the same charge state (Montenegro and Meyerhof, 1992, and Montenegro et al., 1994) so that they cannot be distinguished in this experiment. However, it can be concluded that double ionization of the helium target is larger for the ionization part of antiscreening (single loss reaction channel) than it is for the excitation part of antiscreening and for screening combined (direct ionization). This is seen for Li^{2+} and Li^{+} in Figures 18 and 19 where the ratios for single loss are larger than the ratios for direct ionization at all energies investigated. These results are consistent with the screening-antiscreening theory by Montenegro et al. (1994). These authors investigated the target single ionization process in the projectile-electron loss channel for $He^{+} + H_2$ collisions and found that the projectile nucleus - target electron interaction and the projectile electron - target nucleus interaction are small compared to the projectile electron - target electron interaction above 2 MeV. Therefore, above this energy, for a given projectile species, the antiscreening interaction is stronger than the screening interaction in the single loss channel.

In the single capture channel, the projectile electrons may also play an important role. This can be seen in Figure 21 where the He target double-to-single ionization ratios for the three different incident projectile charge states are compared for this reaction channel. The ratios for both Li^+ and Li^{2+} exhibit approximately the same behavior, have nearly the same magnitude and appear to level off at the highest energies investigated. The ratios for Li^{3+}, however, are still decreasing for the highest energies investigated. At the lower energies investigated (0.3 - 1.0 MeV/u),

$$R_{q,q-1}(Li^{3+}) > R_{q,q-1}(Li^{+}) \, , \, R_{q,q-1}(Li^{2+}), \tag{56}$$

while at higher energies ($\gtrsim$ 1.0 MeV/u) the situation is reversed:

$$R_{q,q-1}(Li^{+}) \, , \, R_{q,q-1}(Li^{2+}) > R_{q,q-1}(Li^{3+}). \tag{57}$$

Therefore, at the lowest velocities the bare projectile produces a larger transfer ionization (TI) fraction (due to electron - nucleus interactions) than the non-bare projectiles (due to a mixture of electron - nucleus and electron - electron interactions), while at the highest velocities the situation is reversed. Thus, the strength of the electron - electron interaction apparently increases compared to the electron - nucleus interaction as the collision velocity increases.

Results for the hydrogenic projectile Li^{2+} can also be compared with He^+ (which has the same electronic structure) and with He^{2+} (which has the same charge). Figure 25 shows that $R_{q,q-1}$ for bare He^{2+} is larger than $R_{q,q-1}$ for one-electron He^+ over nearly the entire energy range investigated. The ratios for Li^{2+}, however, are about twice as large

as those for He^{2+} and for He^{+} in the region of overlap. The fact that $R_{q,q-1}$ for Li^{3+} is higher than $R_{q,q-1}$ for He^{2+} suggests that it is not the ionic charge that is important for the TI fraction, but rather the nuclear charge. Furthermore, the fact that $R_{q,q-1}$ for Li^{2+} is also higher than $R_{q,q-1}$ for He^{+} must be due to the higher nuclear charge of Li^{2+} since both Li^{2+} and He^{+} have the same electronic structure. These results suggest that, for the capture channel in the investigated energy range, Li^{2+} behaves like neither He^{2+} nor He^{+}. Instead, the different nuclear charges of Li and He play a role in this channel.

Therefore, transfer ionization seems to be governed by both the projectile nuclear charge and by the electrons of the projectile. Furthermore, for the present $Li^{1,2,3+}$ data, the relative contribution of the electrons increases strongly compared to the contribution of the nucleus as indicated by Figure 21.

Effective Charge

A good measure of the collective influence of the projectile electrons on the collision process is the effective charge. In this case, the projectile electrons are considered as an electron cloud that can interact with the target via screening or antiscreening (e.g., McGuire et al., 1981, Montenegro et al., 1992, and Montenegro et al., 1994), as mentioned above. As can be seen in Figure 23, the present data for the bare projectile Li^{3+} are in the perturbative two-step regime (see e.g., Andersen et al., 1987,Knudsen et al., 1984, and Tanis, 1992) where double ionization is expected to take place through two separate encounters of the projectile with each of the target electrons. In this velocity regime, single (i=01) and double (i=02) ionization are expected to scale

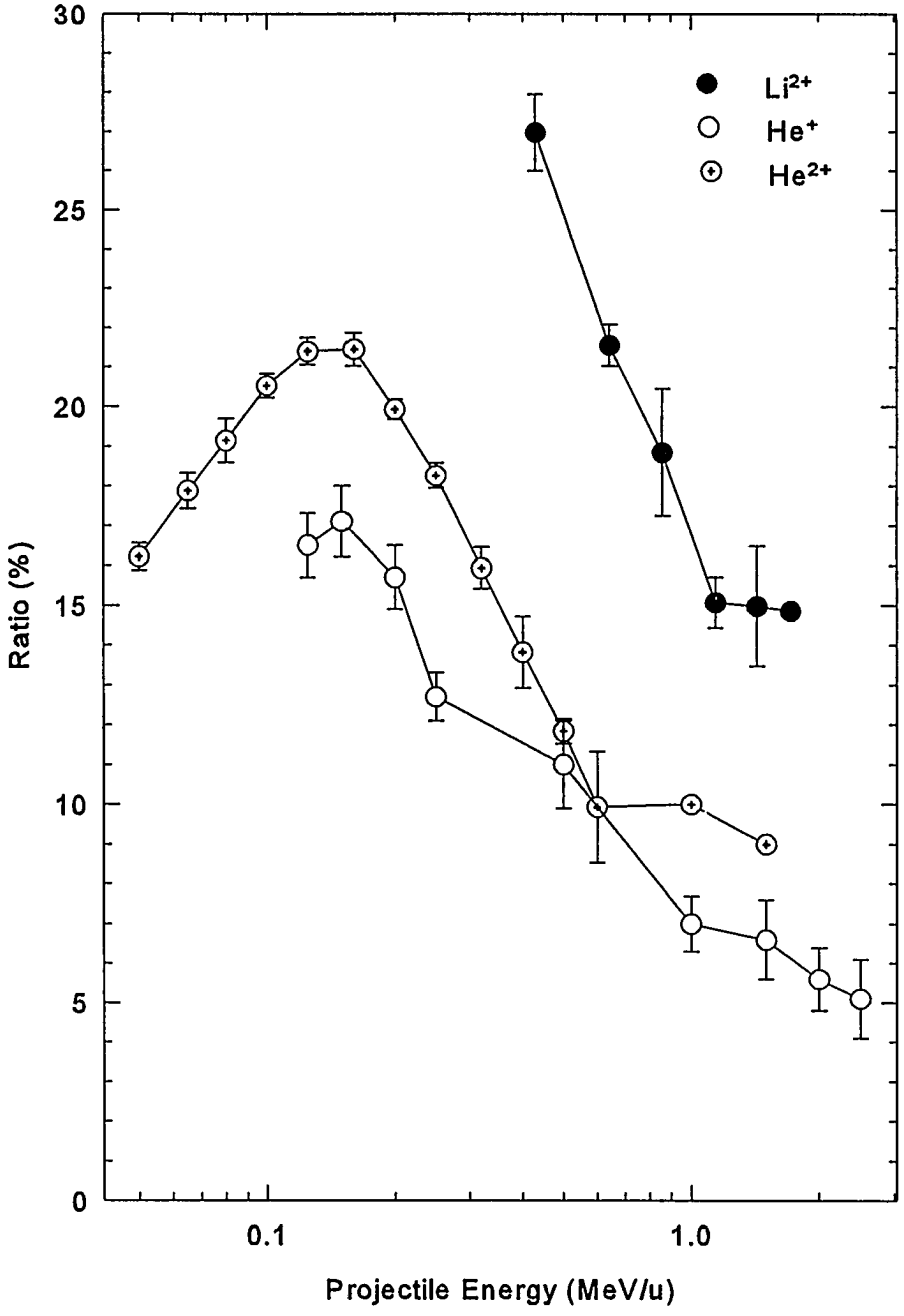

Note: The Li^{2+} data are from the present experiment, while the He^{+} and He^{2+} data are from Forest et al. (1995), Andersen et al. (1987), and Knudsen et al. (1987). The lines are drawn to guide the eye.

Figure 25. He Target Double-to-Single Ionization Ratios Associated With Single-Electron Capture for Li^{2+}, He^{2+}, and He^{+} Projectiles.

like $(q^i_{eff}/v)^2$ and $(q_{eff}/v)^4$, respectively, where q_{eff} is the effective charge of the projectile as seen by the target. (For a discussion of the scaling, refer to the chapter "Theoretical Background".) These relations can be used to calculate the effective charges of Li^+ and Li^{2+} for target ionization by normalizing the direct ionization cross sections for these projectiles to those of the bare projectile Li^{3+}. The results are shown in Figure 26. For Li^+ the average effective charges for single and double ionization are 1.4 and 2.0, respectively, while the average effective charges for single and double ionization by Li^{2+} are 2.1 and 2.4, respectively. For Li^{3+} it is assumed that the effective charge is equal to the nuclear charge, so that the charge is 3 for both single and double ionization.

McGuire et al. (1981) proposed a theory for the effective charge of a hydrogenic projectile based on the screening and antiscreening mechanisms. At distant collisions such a projectile with nuclear charge Z is fully screened so that

$$|q_{eff}^{distant}|^2 = |Z-1|^2, \tag{58}$$

while at close collisions the projectile nucleus and the projectile electrons collide independently with the target so that the effective charge is larger than the nuclear charge:

$$|q_{eff}^{close}|^2 = Z^2+1. \tag{59}$$

For the hydrogenic projectile Li^{2+}, these equations predict an effective charge of 2 for distant collisions and an effective charge of 3.2 for close encounters. The experimentally determined effective charge for single ionization (q_{eff}=2.1) is close to the distant-collision limit, while the effective charge for double ionization (q_{eff}=2.4) is somewhere between the

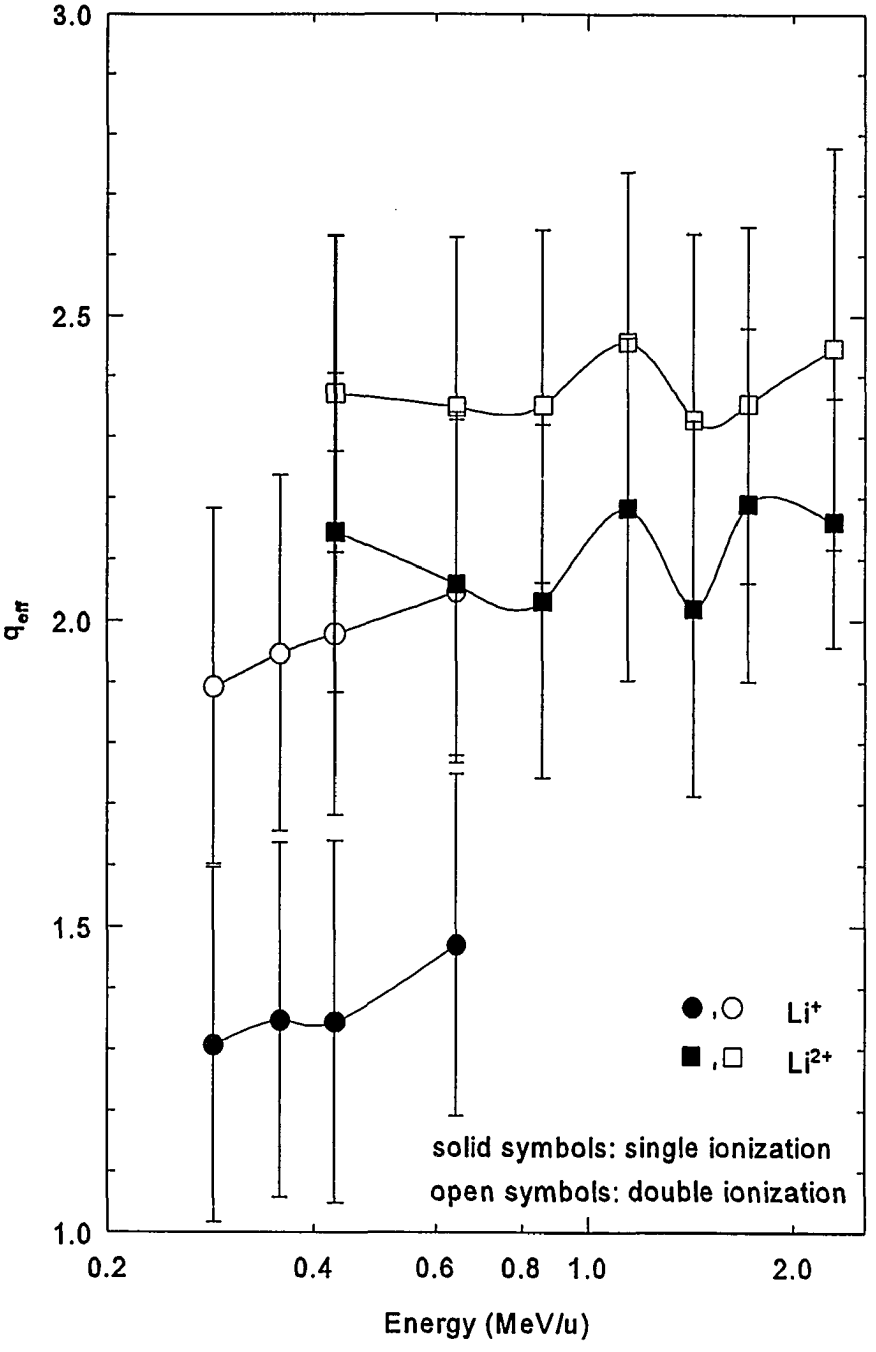

Note: These data have been obtained by normalizing the single and double ionization cross sections in the direct ionization channel to the corresponding cross sections for Li^{3+}. The cross section data used were the values obtained in the present work.

Figure 26. Effective Charges of Li^{+} and Li^{2+} Colliding With He.

close-encounter and the distant-encounter limits. Similar results can be obtained for Li^+. Thus, these results for the effective charge indicate that collisions associated with double ionization require a smaller impact parameter than collisions associated with single ionization as expected, and are consistent with what has been reported by Forest et al. (1995) for $He^+ + He$ collisions.

ELECTRON SPECTROMETER

Overview

An electron spectrometer system has been constructed at WMU and installed on one of the atomic physics beamlines in the Van de Graaff laboratory (see Figure 2). This system allows the detection and energy analysis of continuum-electrons ejected at 0° as well as within a range of about 20° - 160°. A schematic is shown in Figure 27. The spectrometer (Figure 28) consists of two plane-mirror analyzers (PMA) that act as capacitor plates and deflect electrons with a given energy into the channeltron. This energy is proportional to the voltage across the lower pair of PMA's and can be selected by a control computer. An electron energy spectrum is then obtained by scanning a given energy range (using the control computer) and counting the number of pulses originating from the electrons striking the channeltron at each energy. At the same time, outgoing ions in a given charge state can be counted with solid state detectors so that a coincidence setup (as described in an earlier chapter) can detect electron emission in coincidence with a certain charge exchange reaction, e.g., loss or capture processes.

A 486 PC acts as the control for the electron spectrometer system, while a MicroVAX acts as the main data acquisition computer. This scheme was chosen because the data acquisition software, namely, CHAOS, running on the MicroVAX, has proven to be a reliable and versatile data acquisition program which can be used to record

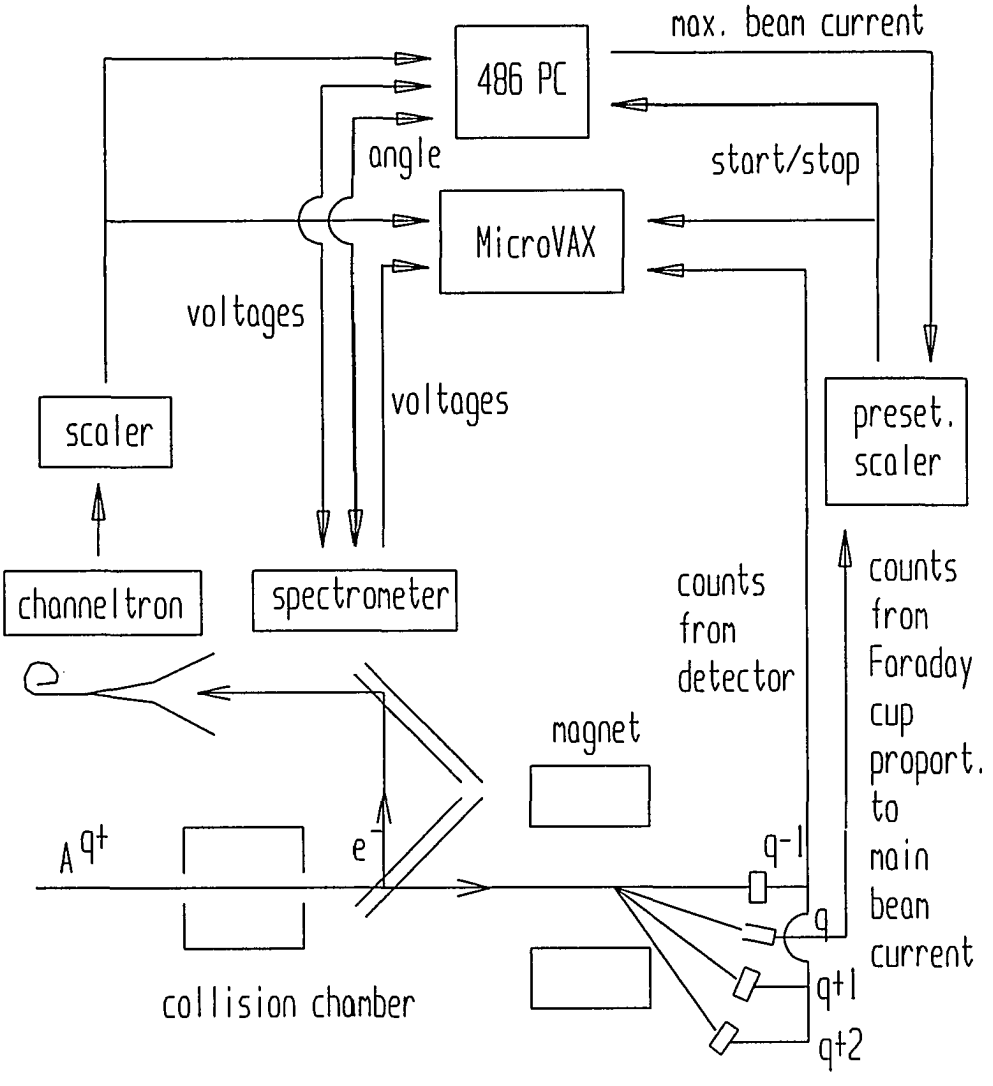

Note: The direction of the flow of information is shown by arrows. The main beam of charge q is collected in a Faraday cup, while the charge-changed projectiles are counted with surface-barrier detectors.

Figure 27. Experimental Setup for Continuum-Electron Measurements.

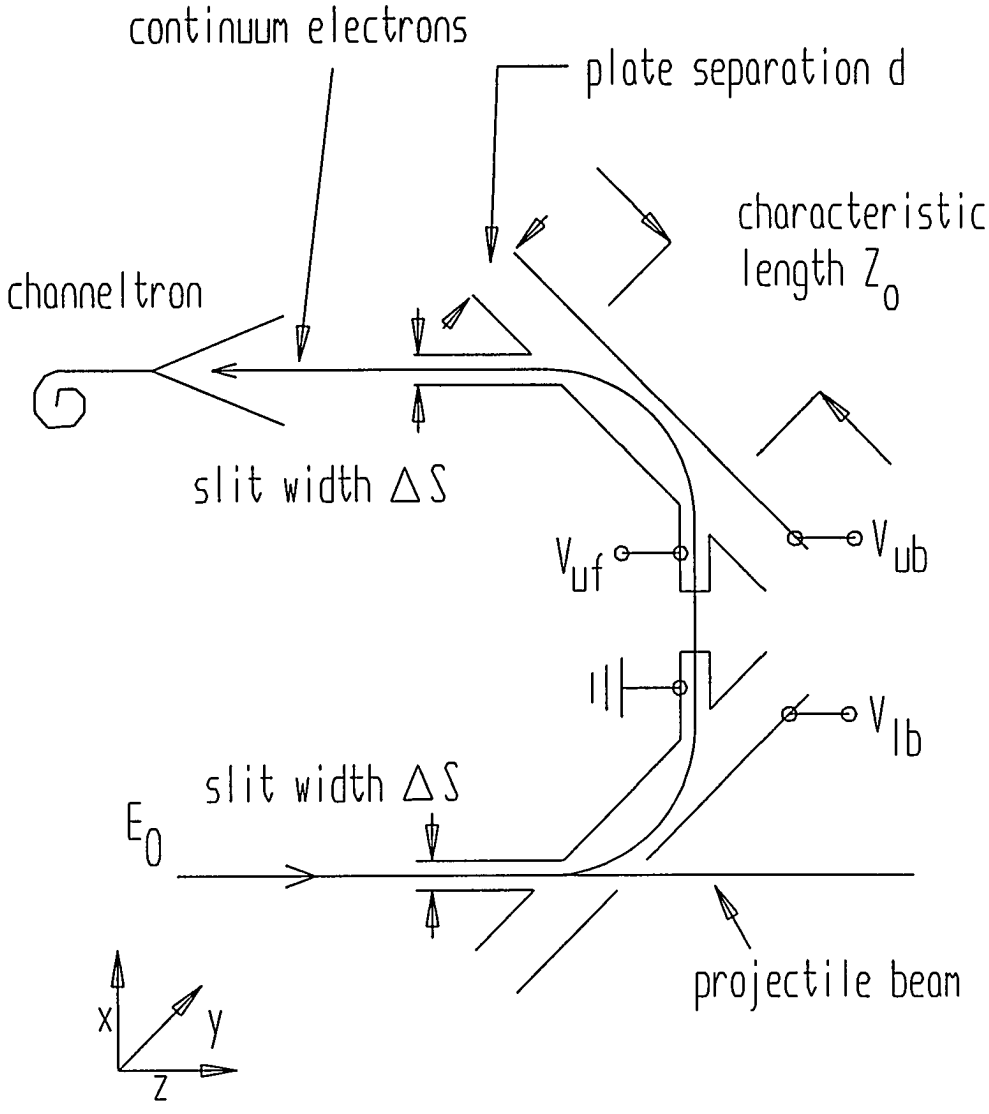

Note: E_0 is the electron energy to be analyzed. The four spectrometer plates, namely, lower front, lower back (lb), upper front (uf), and upper back (ub) are connected to different voltages: ground, V_{lb}, V_{uf}, and V_{ub}, respectively.

Figure 28. Schematic of the Electron Spectrometer.

coincidences between several simultaneous events, while the PC is easier to program and, hence, to use as a control for the spectrometer system.

A typical data acquisition sequence works as follows. The PC prompts the user for the spectrometer angle (defined in the y-z plane as shown in Figure 28), the electron energy range, the number of times to repeat that range, and the integration period (collected charge or time) at each energy point. The integration period is entered as a total number of counts that is proportional to the main beam charge collected in the Faraday cup (Figure 27), or time. This number is stored in a presettable scaler that changes the status of a GATE level when the maximum number of counts is reached. The GATE level is used to turn off the PC data acquisition as well as the MicroVAX data acquisition.

The selected energy range is scanned as the PC increments spectrometer voltages to select the passing energies for electrons ejected from the collision region. While scanning, the total number of electrons is recorded both by the MicroVAX and by the PC. This count number is graphed versus the passing energy of the spectrometer. If the goal of the experiment is to simply collect a continuum-electron spectrum, it is sufficient to use the PC alone. If, however, a spectrum of continuum electrons coincident with beam particles is to be taken, it is necessary to use the MicroVAX which, unlike the PC, is a multiparameter data acquisition system.

This energy scan can be repeated as many times as specified by the user. Should something unexpected (like a surge or a drop of the beam current) occur, the present collection cycle can be aborted and discarded. When all the cycles are completed

successfully, the sum of them is written to an output file which can be imported into various spreadsheet or graphing programs.

Control Program

Centralized control of the spectrometer control is achieved using CAMAC (Computer Automated Measurement And Control). CAMAC is a long-time standard that allows computer control of up to 24 modules in a crate through a dataway. These modules can be addressed by the main computer through combinations of the unique slot number (1-24), the subaddress (A, 1-16), and the function code (F, 1-32). The actions taken upon receipt of the subaddress A and the function code F depend on the type of module being addressed. For a detailed discussion of the CAMAC standard refer to Leo (1994). The hardware setup used in this experiment is shown schematically in Figure 29.

The software controlling the process of data acquisition, called CA7, is written in object-oriented Turbo-Pascal 7.0. The structure of the program follows closely the physical setup shown in Figure 29 with the function of each module programmed into separate subroutines. First, a set of Read and Write commands for the CAMAC crate controller is defined. Using these commands, commands for the next level are composed, i.e., directives for the power supplies , the scaler, the presettable scaler, the input register, the stepper motor controller, and the GPIB interface. The GPIB commands are used to define another set of commands controlling IEEE compatible devices, such as voltmeters and electrometers. This structured approach allows the addition or removal of a module

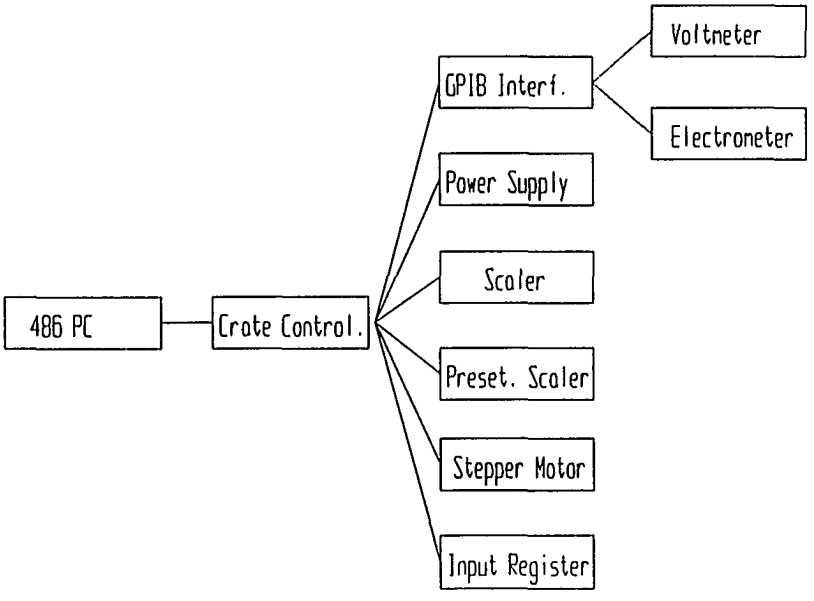

Figure 29. Schematic of the Setup Controlled by the 486 PC.

and its corresponding program code easily.

The object-oriented (OOP) programming approach has two special properties that are made use of in this program: (1) bundling of data and functions together into one object, and (2) inheritance of member functions and data types.

The first property (bundling of data and functions) means that all the characteristics of a physical module, e.g., slot number and device number, and all functions that operate on this module, e.g., commands to read the display or to set the range, are packaged together in one software object. This object can then be treated like any other predefined data type, such as, "real" or "integer". In order to model voltmeters, for example, as many variables as there are voltmeters can be declared to be of the type "TVoltmeter" so that each variable can control one voltmeter independently. Whenever

an operation is performed on one of the voltmeters, the corresponding command does not require a list of arguments such as slot number or device number because all these data are part of the object already. This simplifies the calling of procedures in the code.

The second property (inheritance) allows definition of a new object that inherits everything from an existing one and adds some of its own specific member functions and variables. As shown in Figure 30, the object corresponding to, for instance, the LeCroy power supply ("TLeCroy"), is a specialized type "TModule" (generic CAMAC module having a slot number and Write and Read commands) which means that it now has a slot number, Write and Read commands, and in addition to that, commands to read and set a voltage. Likewise, the object for the Keithley electrometer, "TElectrometer", is a specialized GPIB module ("TIEEE") which in turn is a specialized generic module ("TModule"). "TSpectrum" is a graphics object that contains the measured data and the procedures to display them.

The program allows the user to control all of the connected CAMAC modules directly, and it allows a data acquisition mode in which parameters are changed according to the spectrometer mode that is selected (refer to the spectrometer operation, discussed below). In Figure 31 a calling hierarchy diagram shows how the main subroutines (shown are the names of Pascal units) are interconnected with each other in order to allow control in manual mode (direct control of the modules) or in automatic mode (during data acquisition). The main program is coded in CA7 and this unit has therefore control over everything else. Two branches are connected to CA7:

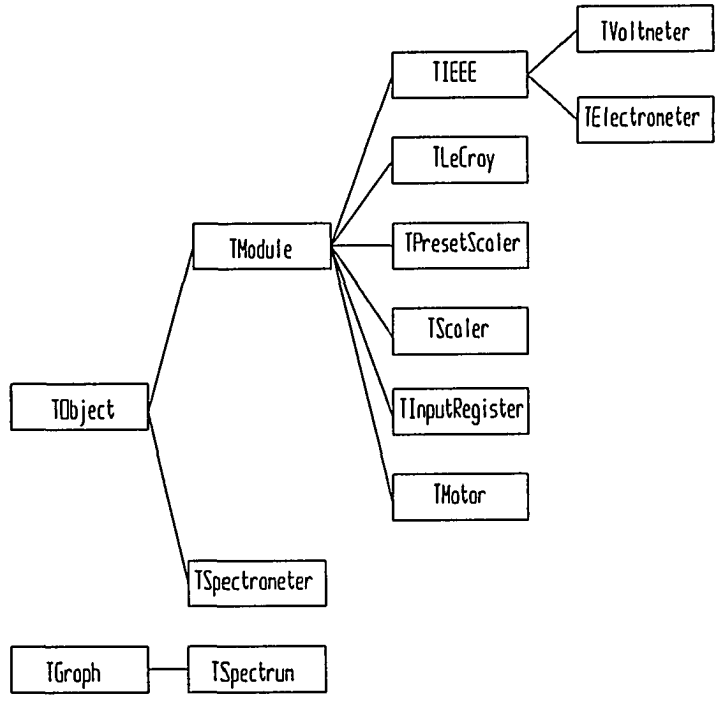

Figure 30. Inheritance Diagram for the CA7 Program.

1. CASTATUS. This unit displays the status of the entire CAMAC system, i.e., it displays a screen with the outputs of all connected modules.

2. CARUN. This unit is used when the computer is collecting data. It has access to the unit CAMODE which contains the code that controls the spectrometer according to the six different modes described below in the section on Spectrometer Operation.

These two branches control the device subroutines, namely, CAVOLT, CAELECTR, CALECROY, CASCALER, CAPRESCA, CAINREG, CAMOTOR. These are the units containing the code for the voltmeter, the electrometer, the LeCroy power supplies, the scalers, the presettable scalers, the input register (shaft encoder), and

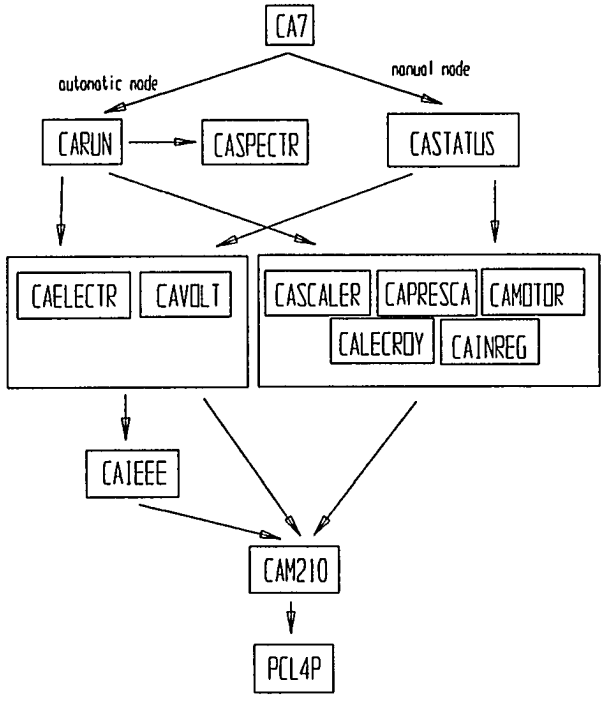

Figure 31. Calling Hierarchy of the Turbo Pascal Units.

the motor controller, respectively. Two of these units, CAVOLT and CAELECTR, call a unit called CAIEEE which contains standardized IEEE-488 compatible commands. This latter unit is used only by IEEE-compatible devices. Each of the two branches access the unit CAM210 which contains the command set used by higher-level procedures to drive the crate controller. The lowest-level procedure PCL4P is a routine used by CAM210 to communicate with the CAMAC crate through the serial port.

Spectrometer Operation

The spectrometer used in this experiment consists of two 45° plane mirror (or

parallel-plate) analyzers (PMA) as described by D. Roy and D. Tremblay (1990) (Figure 28). Each of these PMA's acts as a "bandpass filter" that accepts electrons only within a small energy range determined by the voltages applied to its plates. The projectile beam, due to its relatively large mass, is nearly unaffected by the PMA voltage, and hence is passed through a hole in the spectrometer. The first PMA extracts the electrons from the beam, while the second PMA directs them into a channeltron for detection (Figure 28).

The relationship between the electron charge e, the passing energy E and the required potential difference ΔV between the parallel plates is dependent on a geometric factor k called the spectrometer constant:

$$E_0 = \frac{e\,\Delta V}{k}\,. \tag{60}$$

It is noted that Roy and Tremblay (1990) refer to the inverse 1/k as the spectrometer constant. For 45° PMA's, the spectrometer constant can be calculated using the following formula:

$$k = \frac{Z_0}{2d}\,, \tag{61}$$

where Z_0 is the characteristic length (distance between the entrance and the exit slit) and d the plate separation as shown in Figure 28. For both PMA's used in this experiment the spectrometer constant is nominally

$$k = 0.60. \tag{62}$$

Another characteristic constant of the spectrometer is its energy resolution ΔE (energy spread of the transmitted electrons) which is given by

$$\frac{\Delta E}{E_0} = \frac{2\,\Delta S_1}{Z_0} \tag{63}$$

where ΔS is the width of the entrance and the exit slit (Harrower, 1955). Accordingly,

$$\Delta E = rE_0 \tag{64}$$

where r is a constant that depends on the design. Thus, the absolute resolution improves (decreases) with decreasing passing energy E_0.

The spectrometer can be operated in one of six modes, depending on four different factors: (1) high or low resolution, (2) constant or variable outgoing energy (with which the electrons leave the second plane mirror analyzer), (3) constant or variable transmission between the two plane mirror analyzers, and (4) high or low analyzing energy range (high energy refers to passing energies $\gtrsim$ 100 eV, while the low energy range is 1/5 or 1/10 of the high energy range, depending on the voltage divider factor as explained below).

The possible modes are: (1) low resolution, (2) high resolution, constant outgoing energy, and (3) high resolution, constant transmission.

Additionally, each of these three modes can be run with high or low analyzing energies, giving a total of six possible modes of operation.

Low-Resolution Mode

A circuit diagram for the basic (high energy) setup is shown in Figure 32 (a). Two equivalent PMA's are used and so the passing energy E_0 with which the electrons leave the first PMA is identical to the outgoing energy E_{out} with which the electrons leave the second PMA. In order to account for slightly different spectrometer constants of the two PMA's, these constants, k_l and k_u for the lower and the upper PMA, respectively, can be adjusted with the control program.

The absolute accuracy of the LeCroy power supplies is ±1 V, i.e., the voltage outputs can be as much as are up to 1 V above or below the selected voltage. This can be improved by using the low-energy mode (Figure 32 (b)). In this mode, the power supplies provide voltages which are increased by a factor of 5 or 10, while voltage dividers reduce these voltages by the same factor. By using this technique, the absolute accuracy of ±1 V results in a relative accuracy which is increased by a factor of 5 or 10.

The low-resolution mode is characterized by three factors:

1. Variable Absolute Energy Resolution ($\Delta E = r * E_0$). Because the analyzing energy E_0 is scanned over a range of energies, the FWHM of the peak (ΔE) in the transmitted electron spectrum increases as E_0 increases.

2. Constant Transmission Between the Two PMA's. The transmission through the entire system is determined by the deceleration factor

$$c = \frac{E_0}{E_{out}} \tag{65}$$

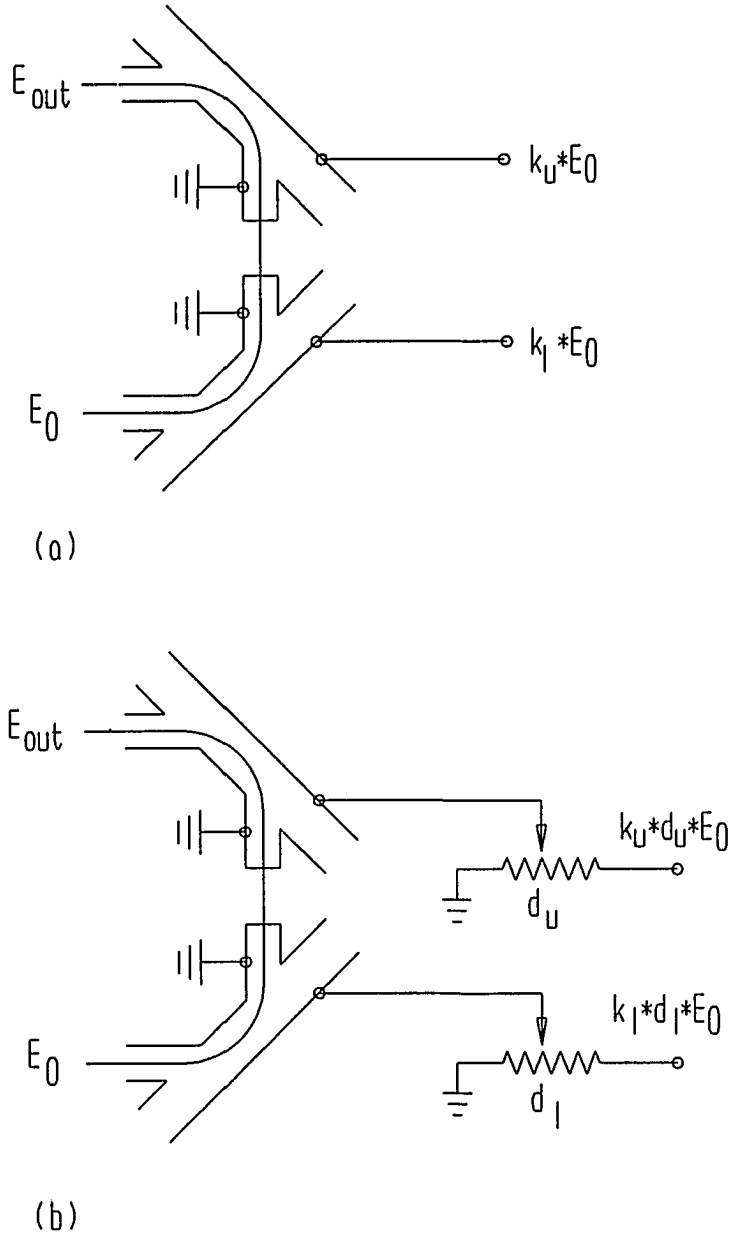

Note: E_0 is the energy to be analyzed, E_{out} is the outgoing energy and k_l, k_u, d_l, and d_u are the lower and the upper spectrometer constants and the divider constants, respectively. All voltages are negative and are numerically equal to the products of the listed factors where the energies are in eV.

Figure 32. Schematics of the Low-Resolution Mode for (a) High Energies and for (b) Low Energies.

which depends on the shape of the electric field between the PMA's. E_0 and E_{out} are the passing energies of the first and the second PMA, respectively. Since in this mode the passing energies for both PMA'S are identical, the transmission does not depend on the analyzing energy E_0.

3. Variable Counting Efficiency. The channeltron has an efficiency that depends on the energy of the passed electrons as shown in Figure 33. Since the outgoing energy varies, the counting efficiency of the channeltron varies also.

High-Resolution Mode, Constant Outgoing Energy

This mode is different from the low-resolution mode in that the outgoing electron energy E_{out} in the second PMA is lower than the analyzing energy E_0 in the first PMA. Therefore, the absolute resolution (which is proportional to the analyzing energy) is better for the second PMA than for the first one. Again, this mode can be run with high (Figure 34(a)) or with low analyzing energies (using a divider constant of 5 or 10, see Figure 34(b)).

The three characterizing factors are:

1. Constant Absolute Resolution ($\Delta E = r * E_{out}$). This is the case because the second PMA has a constant passing energy E_{out} (typically about E_{out} = 12 V) independent of the energy E_0 with which the electrons are extracted from the beam into the first PMA. This low E_{out} ensures a high resolution which is independent of the passing energy E_0.

2. Variable Transmission Between the Two PMA's. The transmission is determined by the deceleration between the two PMA's as given in 65. In Figure 34 it can

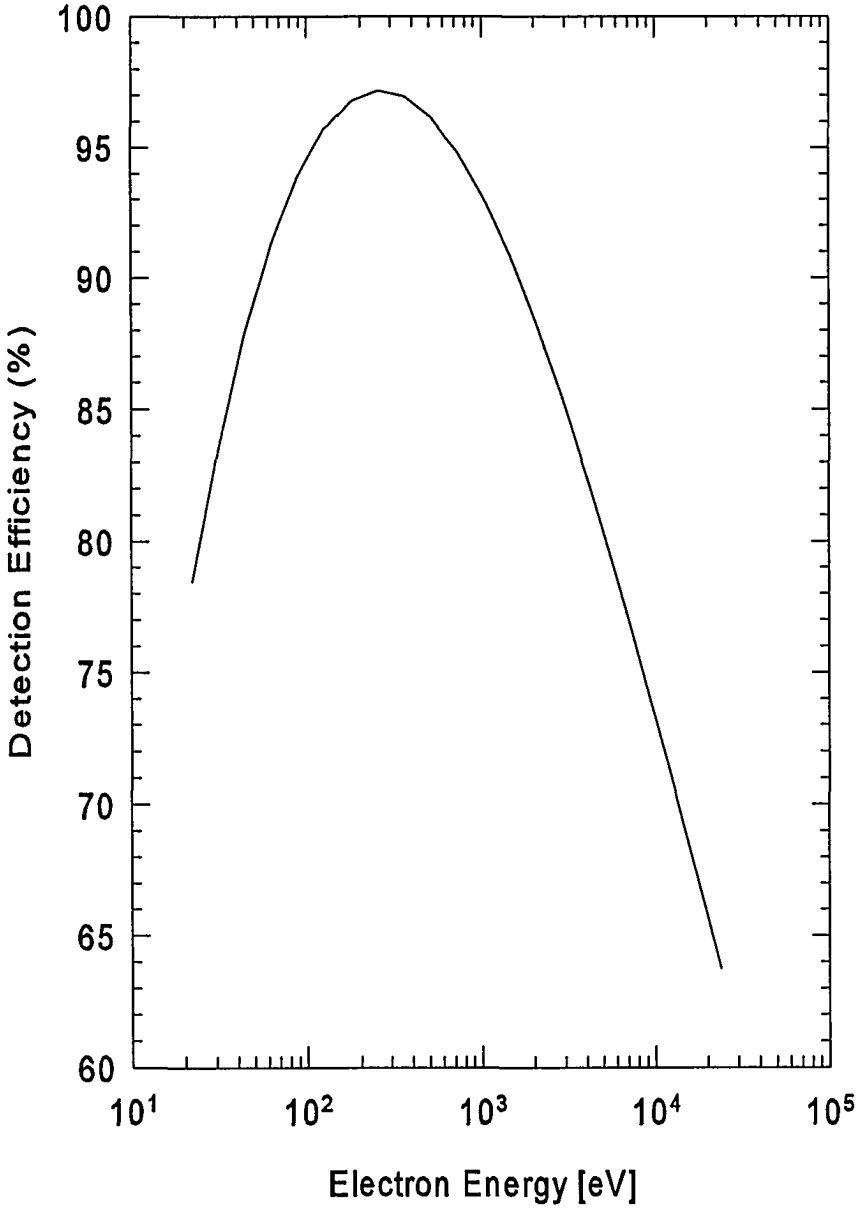

Figure 33. Typical Channeltron Efficiency as a Function of the Impact Energy. (Kurz, 1979).

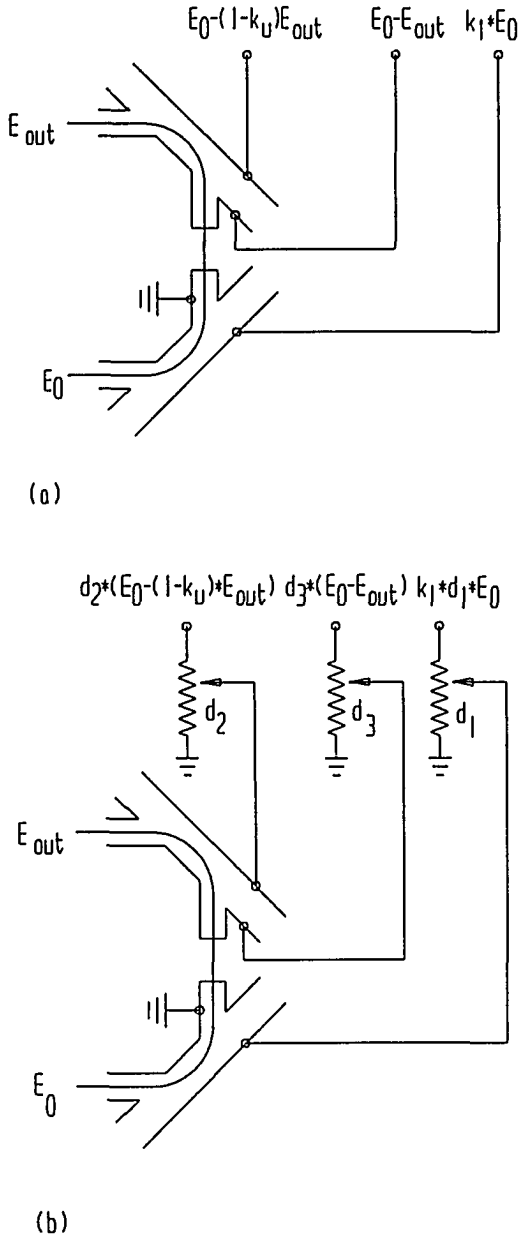

Note: E_0 is the energy to be analyzed, E_{out} is the outgoing energy and k_l, k_u, d_1, d_2, and d_3 are the lower and the upper spectrometer constants and the divider constants, respectively. Voltages are negative and are numerically equal to the products of the listed factors where the energies are in eV.

Figure 34 . Schematics of the High-Resolution Mode With Constant Outgoing Electron Energy for (a) High Energies and for (b) Low Energies.

be seen that the difference between the two passing energies is $E_0 - E_{out}$ which leads to a potential difference between the two PMA's and hence to a dispersion of the electron beam that is dependent on the analyzing energy E_0.

3. Constant Counting Efficiency. The channeltron has an efficiency that depends on the energy of the passing electrons as shown in Figure 33. Since the second PMA passes electrons whose passing energy E_{out} is independent of the analyzing energy E_0, the counting efficiency remains constant.

High-Resolution, Constant Transmission

In this mode, the ratio between the analyzing energy E_0 in the first PMA and the outgoing energy E_{out} in the second PMA remains constant while scanning the given energy range. Again, this mode can be run with high (Figure 35(a)) or with low analyzing energies (using a divider constant of 5 or 10, see Figure 34(b)). The three characterizing factors are:

1. Variable absolute resolution ($\Delta E = r * E_{out}$). This is the case because the analyzing energy E_0 is scanned over a range of energies and the passing energy E_{out} in the second PMA is a function of the passing energy E_0 in the first PMA. This leads to an increase in the FWHM of the peak in the transmitted energy spectrum and therefore to a decrease in resolution with increasing analyzing energy. This decrease in resolution, however, is not as large as in the low-resolution modes because the passing energy in the second PMA is $E_{out}=E_0/c$ where the deceleration constant c is >1, so that ΔE_{out} (high-resolution, constant transmission) < ΔE_{out} (low-resolution).

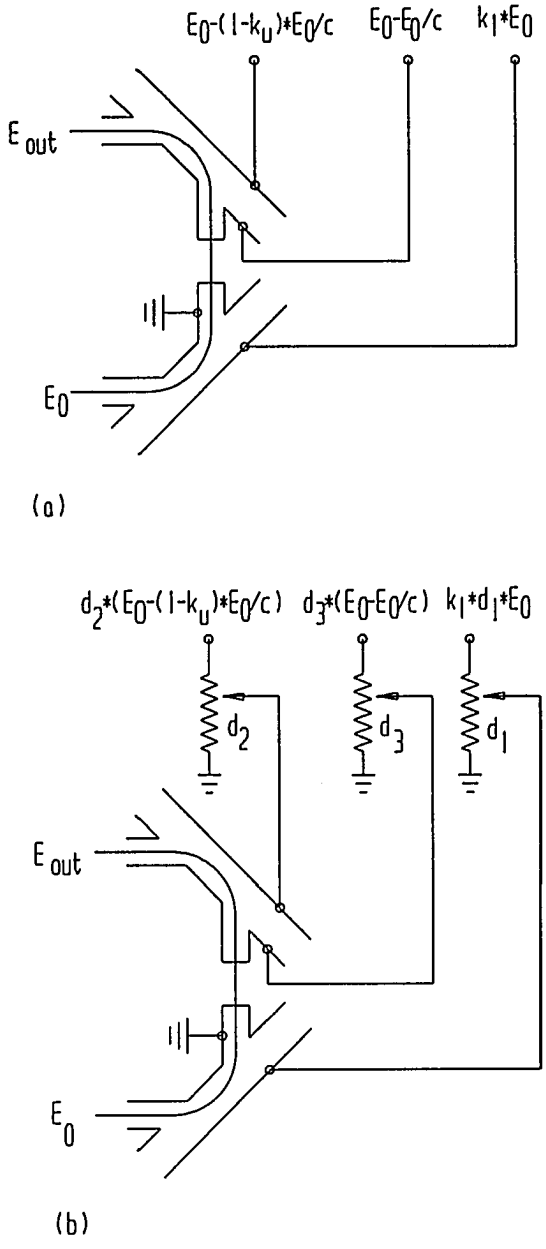

Note: E_0 is the energy to be analyzed, E_{out} is the outgoing energy and k_l, k_u, d_1, d_2, d_3, and c are the upper and the lower spectrometer constants, the three divider constants and the transmission constant, respectively. Voltages are negative and are numerically equal to the products of the listed factors where the energies are in eV.

Figure 35. Schematics of the High-Resolution Mode With Constant Transmission for (a) High Energies and for (b) Low Energies.

2. Constant Transmission Between the Two PMA's. The transmission is determined by the deceleration between the two PMA's as given in Eq. 65. When this mode is used, the experimenter can choose the deceleration factor that determines the ratio between the incoming electron energy E_0 and the outgoing electron energy E_{out}. A constant deceleration between the two PMA's means that the dispersion of the electrons between the PMA's is constant, and so the transmission does not change while scanning the spectrum.

3. Variable Counting Efficiency. The second PMA passes electrons to the channeltron whose passing energy E_{out} (as a function of E_0) changes as the given energy range is scanned; this leads to a variable counting efficiency of the channeltron as shown in Figure 33.

Stepping Motor Control

The stepping motor is connected to the spectrometer through a system of mechanical gears (Figure 36). The motor rotates 2° per step, so 180 steps are needed for a full rotation. The gear system translates one full motor rotation (180 steps) to a 2° spectrometer rotation, i.e., 90 motor steps correspond to a 1° spectrometer rotation. This gives a setting accuracy of (1/90)°. In order to be able to track the rotations and determine the absolute position of the motor, the spectrometer is connected to a shaft encoder. One full rotation of the shaft encoder sends 128 counts to a register module. Three full shaft encoder rotations correspond to eight motor rotations (or a 16° spectrometer rotation). Therefore 3*128 counts are sent for a 16° spectrometer rotation.

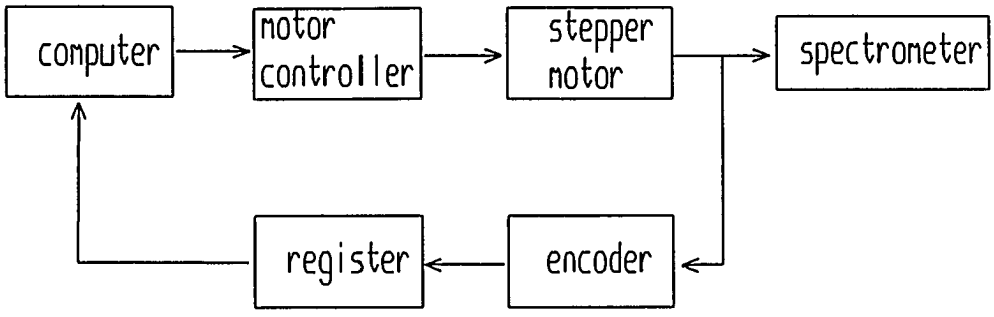

Note: One motor rotation corresponds to 3/8*128 counts at the register and a 2° spectrometer rotation.

Figure 36. Schematic of the Stepper Motor Setup.

This gives a shaft encoder reading accuracy of (1/24)°. The range of the shaft encoder is 13 bits (= 8192) which allows measurement of the angle uniquely over a range of 8192*(1/24)° ≈ 341° before an overflow occurs. In order to ensure a maximum rotational range of -170.5° to +170.5°, the spectrometer should be aligned with the beam direction (see Figure 28), then the shaft encoder disconnected and manually rotated until the register module shows approximately 13 bits / 2 (= 4096 counts). This count number in decimal form is then displayed on the status screen of the spectrometer control program. Then the spectrometer can be rotated by 170.5° in the CW and CCW directions before overflow occurs. The control program has a feature to finetune the alignment within the shaft encoder accuracy of (1/24)°.

Determination of the Spectrometer Constants

The spectrometer constant k has been defined in Eq. 60 as the proportionality constant between the passing energy E_0 and the potential difference ΔV between the two

plates in a PMA. In order to calibrate the spectrometer, this constant has to be determined experimentally.

It is well-known (e.g., Gulyás et al., 1992) that ejected electrons which travel along the beam direction with the velocity of the beam produce a peak in the electron spectrum, the so-called "cusp", which is therefore expected to appear at the electron energy corresponding to the velocity of the projectile beam (see Figure 37).

The electron spectrometer and its control program were tested using a Li^{2+} projectile beam impacting on Ar at 1 MeV/u; thus, the cusp is expected to appear at 1 MeV/1836≈ 545 eV, where 1836 is the proton-electron mass ratio. If, however, the lower spectrometer constant k_l used by the control program, which sets the plate voltage, is different from the actual geometrical value, the electron spectrum will be displaced from its expected position, while its shape is unaltered. (This can be understood from Eq. 60). Since the shape does not change, the measured energy spectrum can be normalized to the known beam energy.

Unlike inaccuracies in the setting of the lower spectrometer constant, inaccuracies in the setting of the upper spectrometer constant not only result in a displacement of the spectrum, but also in a decrease of transmission through the spectrometer and a change in shape of the electron spectrum. The reason for this is that the passing energy is already determined by the lower PMA, and so the upper PMA acts as an additional energy selector which has to be tuned to the first selector. It is therefore more crucial to determine precisely the spectrometer constant of the upper PMA than that of the lower PMA. In Figure 37 spectra are shown for 1 MeV/u Li^{2+} + Ar collisions for various

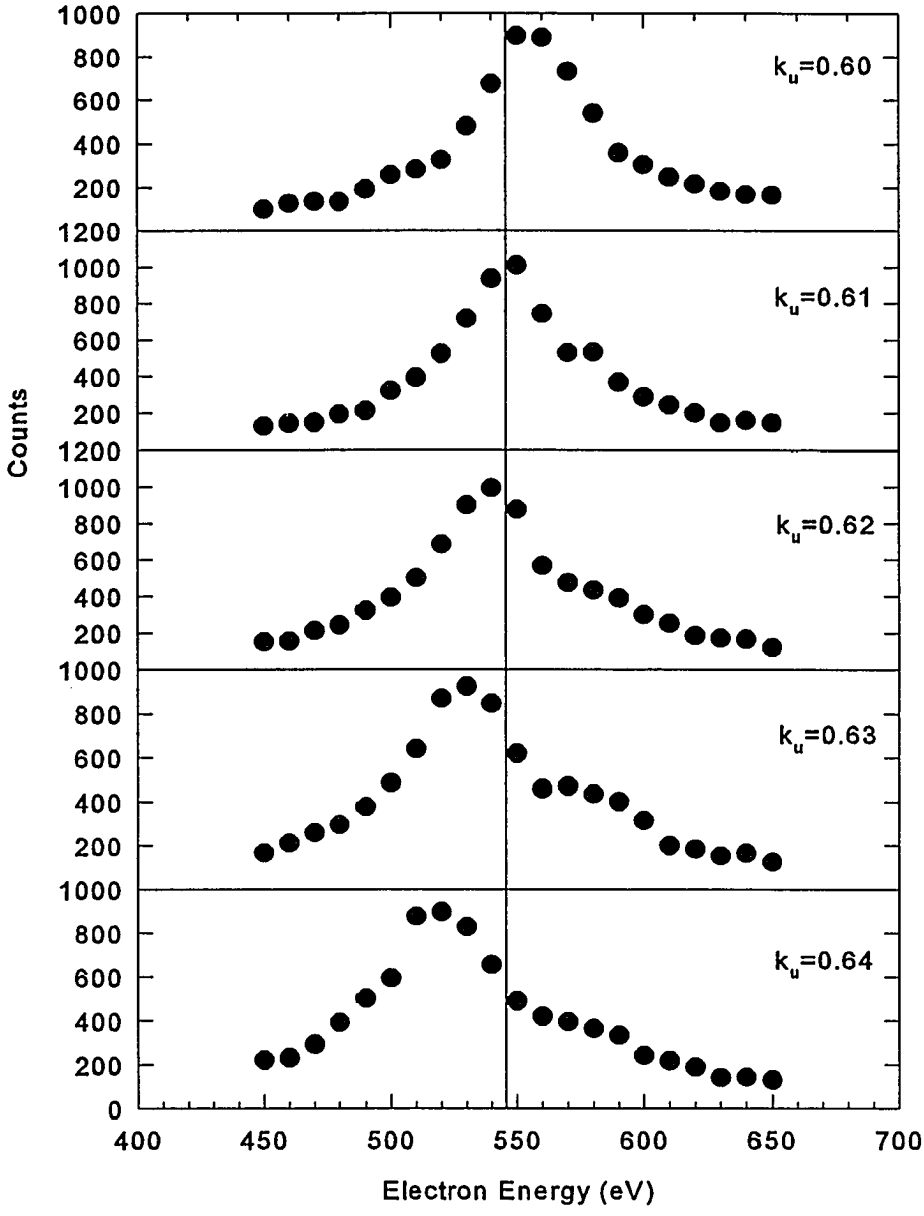

Note: The lower spectrometer k_l constant is 0.60, while the upper spectrometer constant k_u is shown in the upper right corner of each plot. The vertical line at 545 eV corresponds to the beam velocity.

Figure 37. Cusp-Electron Spectra for Li^{2+} + Ar Collisions at 1 MeV/u.

settings (near the nominal value of 0.60) of the upper spectrometer constant for a fixed lower spectrometer constant of 0.60. The vertical line at 545 eV shows the energy of the electrons that travel with the velocity of the projectile beam. It can be seen that the cusp shifts and the shape of the spectrum changes with changing upper spectrometer constant. From these spectra, it appears that the optimum value of the upper spectrometer constant is somewhere between 0.61 and 0.62.

CONCLUSION

Projectile charge changing and target ionization have been studied for Li^{q+} (q=1,2,3) projectiles colliding with He targets in the energy range between 0.5 and 8 qMeV. This work consists of three major parts: investigation of (1) total projectile electron capture and loss, (2) target ionization associated with specific outgoing projectile charge states, and (3) development of an electron spectrometer control system.

In the first part, total charge-changing by the lithium projectiles has been measured without knowledge of the final charge state of the helium target. It was found that: (a) cross sections for total single-electron capture from He to the $Li^{1,2,3+}$ projectiles agree within the experimental uncertainty with the empirical scaling of Schlachter et al. (1987), and (b) cross sections for single-electron loss from $Li^{1,2+}$ projectiles are in agreement with experimental results by Wirkner-Bott et al. (1981) and Hülskötter et al. (1991). The total single-loss cross sections for Li^{2+} also agree with the Bohr theory (Hvelplund et al., 1980 and Knudsen et al., 1982).

Secondly, ionization of He by lithium projectiles for specific reaction channels has been studied. Cross sections for single and double ionization of He by incident $Li^{1,2,3+}$ have been obtained for three projectile reaction channels, namely, direct ionization, single-electron capture, and single-electron loss. In general, good agreement is found in those cases where previous measurements were available for comparison. For all incoming projectile charge states, energies and reaction channels it has been found that the double

ionization cross sections are smaller than the corresponding single ionization cross sections. This implies that double ionization occurs for smaller average impact parameters than single ionization, as expected.

In addition, the effective charges of the $Li^{1,2+}$ projectiles for double and single ionization have been calculated by normalizing to the results for Li^{3+} projectiles and the following results have been obtained, respectively: 1.4 and 2.0 for Li^{+}, and 2.1 and 2.4 for Li^{2+}. For Li^{+} and Li^{2+}, the effective charges for single ionization are close to the distant-collision limit (McGuire et al., 1981), while the effective charges for double ionization are between the distant-collision limit and the close-encounter limit. This is consistent with the fact that double ionization requires smaller average impact parameters than single ionization.

The main emphasis of this work, however, is the ratio R of double-to-single ionization of helium for each the various projectile reaction channels. Three observations have been made:

1. For a given incident projectile charge state, the ratios depend strongly on the reaction channel, with the ratios for projectile electron capture being the largest, those for projectile electron loss the next largest, and the ratios for no projectile charge change the smallest.

2. For direct ionization (no charge change), the ratios are largely independent of the incoming projectile charge state, and apparently depend only on the nuclear charge. And,

3. For projectile single-electron capture and single-electron loss, the ratios depend

quite strongly on the incoming projectile charge state.

Oberservation (1) can be explained qualitatively by the fact that capture occurs for smaller average impact parameters than loss which, in turn, occurs for smaller average impact parameters than direct ionization. For direct ionization, (2), the data for R are in good agreeement with the scaling of Knudsen et al. (1984). Theoretically, however, it is not clear why the ratios are largely independent of the incoming projectile charge state. To solve this problem, more theoretical work is necessary. For the single capture and the single loss channels, (3), it has been shown that the interactions between the projectile and the target depend on the incoming projectile charge state. At the highest energies investigated, the contribution of the antiscreening effect (electron - electron interaction) increases compared to the contribution of the screening effect; this is in agreement with comprehensive studies by McGuire et al., 1981, Montenegro and Meyerhof, 1992, Montenegro et al., 1992, and Montenegro et al., 1994.

While the scaling of the double-to-single ionization ratio for bare projectiles with nuclear charge Z and velocity v is largely understood in the direct ionization channel, this scaling is not understood for dressed projectiles or for projectiles undergoing charge change (single-electron capture or single-electron loss). Future experiments for projectiles with $Z>3$ would be useful to enhance the understanding of the Z and v scaling of the ratio for dressed projectiles and for the single-electron capture and single-electron loss channels.

The present work has been conducted mostly in the perturbative TS and intermediate regimes, i.e., for $0.05 < Z/v < 1$. Future experiments for smaller Z/v, i.e., for

the SO regime, and for higher Z/v, i.e., for the non-perturbative TS regime, could complement the present work. In a recent experiment (Závodszky et al., 1995), the double-to-single ionization ratio has been obtained for the direct ionization and single-electron loss reaction channels for $C^{5,6+}$ + He collisions at 100 MeV/u (Z/v=0.096 for C^{6+}). Additional work could be done to extend the results of this and the present work for direct ionization and single-electron loss. For the (low-energy) non-perturbative TS regime (Z/v>1), few data exist. In this regime, the perturbative $(Z/v)^2$ scaling for independent particle interactions does not apply. Thus, future work could help to improve the understanding of the dependence of the double-to-single ionization ratio on the projecitile charge and velocity for Z/v>1 for the direct ionization, single-electron capture, and single-electron loss channels.

In the third part of this work, an electron spectrometer control system, including software and hardware control and data acquisition, has been presented. The control system has been tested for Li^{2+} + Ar collisions at 1 MeV/u. This electron spectrometer system provides significant new capabilities in which coincidences can be detected between the outgoing projectile charge state, the electron energy, the electron direction, and, in the future, the target charge state, thereby giving further insight into the collision dynamics for various reaction channels.

As an example, studies can be made for electron loss to the continuum (ELC) and electron capture to the continuum (ECC). It has been suggested (Andersen et al., 1984) that the transfer ionization (TI) process can proceed through a direct interaction (ECC accompanied by bound-state capture) or through an ELC reaction accompanied by

double-electron capture to the projectile. Thus, the electron - electron interaction, which was important in the interpretation of some of the results presented in this dissertation, may play a role in continuum-electron emission as well. Studies which are complementary to the work presented here can be done using the electron spectrometer setup to investigate such electron - electron effects.

BIBLIOGRAPHY

Andersen, L.H., Frost, M., Hvelplund, P., & Knudsen, H. (1984). Correlated two-electron effects in highly charged ion-atom collisions: Transfer ionization and transfer excitation in 20-MeV Au^{15+} + He collisions. Physical Review Letters, 52(7), 518-521

Andersen, L.H., Hvelplund, P., Knudsen, H., Møller, S.P., Elsner, K., Rensfelt, K.-G., & Uggerhøj, E. (1986). Single and double ionization of helium by fast antiproton and proton impact. Physical Review Letters, 57 (17), 2147-2150.

Andersen, L.H., Hvelplund, P., Knudsen, H., Møller, S.P., Sørensen, A.H., Elsener, K., Rensfelt, K.-G., and Uggerhøj, E. (1987). Multiple ionization of He, Ne, and Ar by fast protons and antiprotons. Physical Review, A36 (8), 3612-3629.

Bates, D.R., & Dalgarno, A. (1952). Proceedings of the Physical Society A65, 919

Bates, D.R. & Mapleton, R.A. (1966). Proceedings of the Physical Society (London) 87, 657

Briggs, J.S., & Taulbjerg, J, (1979). Charge transfer by a double-scattering mechanism involving target electrons. Journal of Physics B: Atomic and Molecular Physics, 12 (15), 2565-2573

Brinkman, H.C., & Kramers, H.A. (1930). Proceedings of the Academy of Sciene 33, 973

Drake, G.W.F. (1971). Theory of relativistic magnetic dipole transitions: lifetime of the metastable $2\ ^3S$ state of the heliumlike ion. Physical Review, A3(3), 908-915.

Drake, G.W.F., Victor, G.A., & Dalgarno, A. (1969). Two-photon decay of the singlet and triplet metastable states of helium-like ions. Physical Review, 180(1), 25-32.

Drisko, R.M. (1955). Ph.D. Thesis, Carnegie Institute of Technology, unpublished.

Ferguson, S.M. (1995). private communication.

Forest, J.L. (1991). Double ionization of helium by intermediate to high energy velocity He^+ projectiles. M.A. thesis, Western Michigan University, Kalamzaoo, MI.

Forest, J.L., Tanis, J.A., Ferguson, S.M., Haar, R.R., & Lifrieri, K. (1995). Single and double ionization of helium by intermediate-to-high-velocity He^+ projectiles. Physical Review, A52 (1), 350-356.

Glasstone, Lovberg (1960). Controlled thermonuclear reactions. Princeton, N. J.: D. Van Nostrand Company.

Gulyás, L., Sarkadi, L., Pálinkás, J., Kövér, Á., Vajnai, T., Szabó, Gy., Végh, J., Berényi, D., and Elston, S.B. (1992). Cusp-shape studies with He^+ ions at 1.41- and 2.41-a.u. impact velocities. Physical Review, A45 (7), 4535-4541

Haken, H. & Wolf, H.C. (1987). Atom- und Quantenthysik. Einführung in die experimentellen und theoretischen Grundlagen. Chapter 23.4. Berlin, Germany: Springer-Verlag.

Harrower, G.A. (1955). Measurement of electron energies by deflection in a uniform electric field. The Review of Scientific Instruments, 26, 850 - 854.

Hülskötter, H.-P., Feinberg, B., Meyerhof, W.E., Belkacem, A., Alonso, J.R., Blumenfeld, L., Dillard, E.A., Gould, H., Guardala, N., Krebs, G.F., McMahan, M.A., Rhoades-Brown, M.E., Rude, B.S., Schweppe, J., Spooner, S.W., Street, K., Thieberger, P., & Wegner, H.E. (1991). Electron-electron interaction in projectile electron loss. Physical Review, A44(3), 1712-1724.

Hvelplund, P. (1976). Electron capture and loss by ground-state and metastable Li^+ in helium and argon targets. Journal of Physics B: Atomic and Molecular Physics, 9(9), 1555-1565.

Hvelplund, P., Haugen, H.K., & Knudsen, H. (1980). Single- and double-electron loss from helium by collisions with $v \geq v_0$ multiply charged ions. Physical Review, A22(5), 1930-1940

Jackson, J.D., & Schiff, H. (1953). Physical Review 89, 359.

Knudsen, H., Andersen, L.H., Haugen, H.K., & Hvelplund, P. (1982). Electron loss from fast one-electron ions colliding with He, N_2, and Ar. Physica Scripta, 26, 132-140

Knudsen, H., Andersen, L.H., Hvelplund, P., Astner, G., Cederquist, H., Danared, H., Liljeby, L., & Rensfelt, K.-G. (1984). An experimental investigation of double ionisation of helium atoms in collisions with fast, fully stripped ions. Journal of Physics B: Atomic and Molecular Physics, 17, 3545-3564

Knudsen, H., Andersen, L.H., Hvelplund, P., Sørensen, & Ćiric, D. (1987). Simultaneous

capture and ionisation for fast ion impact on helium. Journal of Physics B: Atomic and Molecular Physics, 20, L253-L257.

Knudsen, H., Haugen, & H.K., Hvelplund, P. (1981). Single-electron-capture cross section for medium- and high-velocity, highly charged ions colliding with atoms. Physical Review, A23 (2), 597-610.

Kurz, E.A. (1979). Channel electron multipliers. American Laboratory, March 1979.

Leo, W.R. (1994). Techniques for Nuclear and Particle Physics Experiments, 2nd Edition. Berlin, Germany: Springer Verlag.

Mapleton, R.A. (1961). Physical Review 122, 528.

McDowell, M.R.C., & Coleman, J.P. (1970). Introduction to the theory of ion-atom collisions. Amsterdam: North-Holland.

McGuire, J.H. (1982). Double ionization of helium by protons and electrons at high velocities. Physical Review Letters, 49(3), 1153-1157

McGuire, J.H. (1984). High-velocity limits for the ratio of double to single ionisation by charged particles and by photons. Journal of Physics B: Atomic and Molecular Physics, 17, L779-L784.

McGuire, J.H. (1987). Correlation in atomic scattering. Physical Review, A36(3), 1114-1122.

McGuire, J.H. (1991). Multiple-electron excitation, ionization, and transfer in high-velocity atomic and molecular collions. Advances in atomic, molecular, and optical physics, 29, 217-323

McGuire, J.H., Berrah, N., Bartlett, R.J., Samson, J.A.R., Tanis, J.A., Cocke, C.L., & Schlachter, A.S. (1995). The ratio of cross sections for double to single ionization of helium by high energy photons and charged particles. Journal of Physics B: Atomic, Molecular, and Optical Physics, 28, 913-940

McGuire, J.H., Salzborn, & E, Müller, A. (1987). Simulataneous capture and ionization in helium. Physical Review, A35(8), 3265-3268

McGuire, J.H., Stolterfoht, N., & Simony, P.R. (1981). Screening and antiscreening by projectile electrons in high-velocity atomic collisions. Physical Review, A24 (1), 97-102.

Merzbacher, E. (1970). Quantum Mechanis. New York: John Wiley & Sons.

Montenegro, E.C., Melo, W.S., Meyerhof, W.E., & Pinho, A.G. (1992). Separation of the screening and anitscreening effects in the electron loss of He^+ on H_2 and He. Physical Review Letters, 69 (21), 3033-3036.

Montenegro, E.C. and Meyerhof, W.E. (1991). Target screening effect on the projectile electron-loss probability. Physical Review, A44 (11), 7229-7233.

Montenegro, E.C. and Meyerhof, W.E. (1992). Inelastic electron-electron interaction in the projectile-electron-loss probability. Physical Review, A46 (9), 5506-5513.

Montenegro, E.C., Meyerhof, W.E., & McGuire, J.H. (1994). Role of two-center electron-electron interaction in projectile electron excitation and loss. Advances in Atomic, Molecular, and Optical Physics, 34, 249-300.

Nikolaev, V.S., Dmitriev, I.S., Fateeva, L.N., & Teplova, Ya., A. (1961). Experimental investigation of electron capture by multiply charged ions. Soviet Physics JETP, 13(4), 695-869.

Olson, R.E. (1978). Electron-capture and impact-ionization cross sdctions for multiply charged ions colliding with helium. Physical Review, A18 (6), 2464-2469.

Oppenheimer, J.R. (1928). Physical Review 31, 349.

Pivovar, L.I., Levchenko, Yu.Z., & Krivonosov, G.A. (1971). Ionizing collisions and charge exchange for Li^+, Li^{2+}, and Li^{3+} ions in gases (0.2 - 2 MeV). Soviet Physics JETP, 32 (1), 11-15.

Ramsey, N.F. (1956). Molecular beams. Oxford: Clarendon.

Roy, D., Tremblay, D. (1990). Design of electron spectrometers. Reports on Progress in Physics, 53, 1621-1674.

Sanders, J. (1995). private communication.

Schlachter, A.S., Stearns, J.W., Berkner, K.H., Stockli, M.P., Graham, W.G., Bernstein, E.M., Clark, M.W., & Tanis, J.A. Electron capture for fast highly charged ions in He: An empirial scaling rule revisited. Abstracts of Contributed Papers, Fifteenth International Conference on the Physics of Electronic and Atomic Collisions, Brighton, United Kingdom, 1987, page 505.

Shah, M.B. & Gilbody, H.B. (1985). Single and double ionisation of helium by H^+, He^{2+}

and Li^{3+} ions. Journal of Physics B: Atomic and Molecular Physics, 18, 899-913.

Shakeshaft, R. (1974). Connection between the classical and quantum mechanical treatments of the forward capture of a light particle in the high velocity limit. Journal of Physics B: Atomic and Molecular Physics, 7 (9), 1059-1065.

Tanis, J.A. (1989). Interactions involving two electrons in ion-atom collisions. Nuclear Instruments and Methods in Physics Research, B40/41, 70-76.

Tanis, J.A. (1992). Testing double ionization mechanisms with highly charged ions. AIP Conference Proceedings: VIth International Conference on the Physics of Highly-Charged Ions, Manhattan, Kans., 28 Sept. - 2 Oct. 1992

Taulbjerg, K. (1983). Electron capture in ion-atom collisions. Fundamental processes in energetic atomic collisions, edited by Lutz, H.O., Brigss, J.S., & Kleinpoppen, H., Plenum Press, New York, N.Y. and London, England.

Thomas, L.H. (1927). Proceedings of the Royal Society, 114, 561

Végh, L. and Burgdörfer, J. (1990). Shakeoff induced by fast charged projectiles. Physical Review, A42 (1), 655-658.

Welsh, L.M., Berkner, K.H., Kaplan, S.N., & Pyle, R.V. (1967). Cross sections for electron capture by fast protons in H_2, He, N_2, and Ar. Physical Review 158 (1), 85-92.

Wirkner-Bott, I., Seim, W., Müller, A., Kester, P., & Salzborn, E. Electron capture by Li^{3+} and Li^{2+} ions in H_2 and He. Journal of Physics B: Atomic and Molecular Phys., 14, 3987-3991.

Woitke, O., Ferguson, S.M., Haar, R.R., Jasper, E., Plano, V.L., Tanis, J.A. (1994). Projectile charge changing in 0.2 - 1.2 MeV/u $Li^+ + H_2$ collisions. Meeting of the Division of Atomic and Molecular Physics of the American Physical Society, Crystal City, VA, 18 - 22 April, 1994.

Woitke, O., Závodszky, P.A., Ferguson, S.M., and Tanis, J.A. (1995). Single and double ionization of He by 0.5 - 8 MeV/q Li^{q+} (q=1,2,3) ions. Scientific Program and Abstracts of Contributed Papers, Nineteenth International Conference on the Physics of Electronic and Atomic Collisions, Whistler, British Columbia, 1995, page 56.

Závodszky, P.A., Tanis, J.A., Kamber, E.Y., Houck, J.H., & Woitke, O. (1995). Unpublished.

Zhu, M., Haar, R.R., Ferguson, S.M., Woitke, O., J.A. Tanis, Sarkadi, L., Pálinkás, J., Závodszky, P.A., and Berényi, D. (1995). Cusp-electron production in intermediate-energy O^{7+} + Ar collisions. Nuclear Instruments and Methods in Physics Research, B98, 351-353.